Geo-Information Science and Remote Sensing
Thesis Report GIRS-2020-16

Mapping Sargassum on beaches and coastal waters of Bonaire using Sentinel-2 imagery

William Tjiong

2020

Mapping Sargassum on beaches and coastal waters of Bonaire using Sentinel-2 imagery

---

William Tjiong

Registration number 940211-836-070

Supervisors:

dr.ir. JGPW (Jan) Clevers

dr.ir. CA (Sander) Mücher

A thesis submitted in partial fulfilment of the degree of Master of Science

at Wageningen University and Research Centre,

The Netherlands.

Cover page image adapted from Global Environment Facility (2018)

March 2020
Wageningen, The Netherlands

Thesis code number: GRS-80436
Thesis report: GIRS-2020-16
Wageningen University and Research Centre

Laboratory of Geo-Information Science and Remote Sensing

Abstract

Sargassum is a type of brown algae that can be found in coastal waters or free floating in the ocean. Sargassum is not directly harmful on sea, in fact a lot of marine species such as fishes and sea turtles depend on it for shelter and food source. Climate change and increasing amount of nutrient in the Caribbean Sea has presumably led to recurring large scale Sargassum influxes in this region since 2011. The worst influx occurred in 2018 which impacted many islands in the Dutch Caribbean including Bonaire. Sargassum brown tide flooded the island and deprived the coastal ecosystems from oxygen, which led to degradation of mangroves and seagrass beds in Bonaire. Besides, the smell of rotting seaweed on beaches repels tourists having an adverse effect on the tourism sector. Measures must be taken to prevent irreparable damage on the ecosystems and economy of Bonaire due to Sargassum influx. There is a great need for an early warning system that alerts the authorities for possible Sargassum influx and a monitoring system that can assess the extent and impact of Sargassum on coastal ecosystems. With up to 10m spatial resolution and five days revisit time, the freely available Sentinel-2 satellite platform might be a good opportunity for such a warning and monitoring system.

This research investigated the effectiveness and limitations of Sentinel-2 images for mapping Sargassum on the open sea, the coastal waters and the east coast of Bonaire. This research also evaluated the potential of Sentinel-2 images for mapping the seagrass distribution in the shallow waters of Lac Bay in relation to the possible impact of Sargassum. Sargassum and seagrass distribution maps are important for coastal managers to locate the most impacted sites and to design suitable measures.

Supervised Decision Tree and Maximum Likelihood Classifiers (DTC and MLC) were explored to map Sargassum and seagrass on the coast. A chi-square threshold technique was applied to the MLC, referred to as $\mathrm{MLC}_{\mathrm{probability\%},}$ to avoid misclassifications. Training sites were visually defined from Sentinel-2 images taken in 2019 to collect reference Sargassum and seagrass pixels for training the supervised classifiers. A distinction between Sargassum on land and water was made apart from six other classes in the training samples. In the lagoon Lac Bay only seagrass and non-seagrass classes were addressed for mapping their distribution. Feature selection based on the Jeffries-Matusita distance was performed to select the best band selection and spectral index combinations. Sargassum ground truth data or training sites can be difficult to assess on open sea because its presence is temporary and unpredictable. Therefore, unsupervised classifications based on density slicing and Principal Component Analysis were explored to detect floating Sargassum on open sea. Density slicing was used to segment a Green Normalized Difference Vegetation Index ($\mathrm{GNDVI}_{\mathrm{Slice}}$) image, whilst a Triangle thresholding was used to automatically segment a Principle Component image ($\mathrm{PCA}_{\mathrm{Triangle}}$). The classification results were compared across different time periods apart from each research objective. The best classification method was widely evaluated based on classification accuracy, image interpretation and robustness of the classification methods.

Results showed that the Normalized Difference Vegetation Index (NDVI), Red-Edge Position Index (REP) and Sentinel-2 bands B05 (VNIR at 705nm) and B11 (SWIR at 1610nm) were effective in separating Sargassum from other coastal features. The $\mathrm{MLC}_{20\%}$ model achieved an excellent validation accuracy of 87% and was found suitable for classifying floating Sargassum on coastal waters while minimizing false positives due to cloud edges and dark mangrove fringes. Persisting misclassifications of Sargassum on land occurred due to various degree in organic decomposition and water content of the Sargassum leading to a larger variation in spectral reflectances and so ambiguity in the training samples and possibly due to mixed pixels in addition. Consequently, floating Sargassum and coastline pixels were often overestimated as Sargassum on land. Hence, Sargassum on land cannot be classified with a high accuracy in this study. The $\mathrm{PCA}_{\mathrm{Triangle}}$ and $\mathrm{MLC}_{\mathrm{Base}}$ methods were effective in detecting floating Sargassum on open sea. The $\mathrm{MLC}_{\mathrm{Base}}$ model does not use a chi-square threshold, hence every pixel is classified on the image. The $\mathrm{PCA}_{\mathrm{Triangle}}$ method is excellent for classifying sparsely distributed Sargassum slicks on rough waters, whilst the $\mathrm{MLC}_{\mathrm{Base}}$ method is suitable for open calm sea. The study also showed that clouds, image striping and inter-band parallax effects were the main sources of misclassification of Sargassum in open sea. In this study, the seagrass distribution cannot be assessed accurately since fringing coral reefs and deep-water pixels were grossly overestimated as seagrass. This means that the impact of Sargassum on the seagrass can be neither assessed.

Nevertheless, this research confirmed the capability of Sentinel-2 platform for mapping Sargassum. The results of this study can be used as a reference to develop a proper Sargassum warning and monitoring framework and support other studies on the potential of remote sensing for coastal ecosystems.

Keywords: Sargassum, Seagrass distribution, Remote Sensing, Sentinel-2, Coastal ecosystems, Supervised and Unsupervised Classification.

Table of contents

List of figures

List of tables

Chapter 1 Introduction

1.1 Context

Sargassum is a genus of brown macroalgae or seaweed that can be found in shallow waters or free floating in the ocean. Sargassum patches on the open sea drift along sea currents and can aggregate into larger Sargassum rafts or long slicks. One of the early studies on Sargassum observations focused on defining the extent of Sargassum coverage in the Sargasso Sea (Krümmel, 1891). The Sargasso Sea is a large region in the North Atlantic Ocean, known for its great abundance of floating Sargassum. More than 89% of the species found in the Sargasso Sea can be classified into two species: *Sargassum natans* and *Sargassum fluitans* (Deacon, 1942). Both species are 'holopelagic' meaning that they spend their entire lifespan floating on the sea surface and reproduce exclusively by vegetative fragmentation (Winge, 1923).
Sargassum seaweeds that accumulate in the Sargasso Sea originate from The Gulf of Mexico where it blooms in the spring (Laffoley et al., 2011). This Sargassum bloom is induced by nutrient loadings from land that are discharged via the Mississippi River into the sea (Lapointe, 1995). Consequently, large populations of Sargassum seaweeds accumulate over the summer and form extensive Sargassum rafts in this region. Some Sargassum may get carried to inshore waters, but most of them dies off in the winter, to be restocked again next season (Laffoley, 2011).

Sargassum is not directly harmful on sea, in fact diverse biotic communities and animal species such as fishes, sea turtles and invertebrate depend on the seaweed for shelter and as a food source (Vos et al., 2016). However, Sargassum can potentially damage coastal ecosystems such as mangroves and seagrass beds if it accumulates on these coastal ecosystems. Therefore, monitoring of pelagic Sargassum is of great importance for managing coastal ecosystems. Attempts to map the abundance pelagic Sargassum in the Atlantic Ocean in the past has proven to be a complex problem that involves the dynamic sea environment such as seasonal biomass distribution, ocean climate and human-induced factors (Butler & Stoner, 1984; Krümmel, 1891; Parr, 1939). Therefore, a more sophisticated method of mapping pelagic Sargassum in the ocean is needed.

Advances in earth observation and remote-sensing technologies provide a large amount of data and applications for land and marine resource management. Spaceborne remote sensing can be used for monitoring the impact of hazards affecting the marine ecosystems such as oil spills, plastic pollution, flooding, iceberg deterioration, marine debris and harmful algal blooms at global scale (Platt et al., 2008). Applications in spaceborne remote sensing combined with ancillary data, such as sea surface temperature and sea current models, are useful in the management and conservation of fish and marine mammal species (National Research Council, 2011; Platt & Sathyendranath, 2008).

1.2 Problem definition

An unprecedented amount of pelagic Sargassum invaded the Caribbean islands in the summer of 2011 (Higgins, 2011). Masses of Sargassum seaweed piled up on beaches trapping sea turtles and releasing high concentrations of toxic hydrogen sulfide gas when it decomposes (Atkin, 2018). Beside sea turtles, local tourism was also affected by the Sargassum beaching which led to temporarily closure of hotel resorts and high-cleaning costs of beaches (Caribbean Regional Fisheries Mechanism, 2014; Higgins, 2011). Sargassum was before a rare occurrence in the Caribbean Sea, yet recent Sargassum influx suggest otherwise. Climate change in combination with nutrient pollution of the Caribbean Sea might have caused this phenomenon. Satellite observations from 2011 indicated new locations of Sargassum north of the coast of Brazil

(Gower et al., 2013), later dubbed as the great Atlantic Sargassum belt (GASB) (Wang et al., 2019). Monthly satellite data were able to clearly show a massive Sargassum bloom extending from the Caribbean to West Africa in the summer of 2011. This bloom seems to recur every year resulting in multiple large-scale Sargassum events such as in 2014 on the shores of San Andreas Island (El Isleño, 2014) and in 2015 on the coasts of Haiti and Bonaire (Dutch Caribbean Nature Alliance, 2019; Haiti Libre, 2015) among other regions.

Climate change and increasing nutrification of seas indicate that the amount of Sargassum in the Caribbean Sea might increase substantially within the near future. The global average temperature is estimated to increase every decade by 0.2 °C (Masson-Delmotte et al., 2018). Consequently, higher rates of precipitation, rising sea level, higher water temperatures and changes in ocean currents are expected due to global warming (Pink, 2018). Wang et al. (2019) suggest that changing ocean dynamic and high nutrient supplies from the Amazon River and West Africa may have fueled this massive Sargassum bloom in the central Atlantic.

The highest record of Sargassum bloom, with approximately 20 million ton of wet biomass, occurred in the year of 2018 (Wang et al., 2019) in the Atlantic. Consequently, major Sargassum brown tides invaded the Dutch Caribbean Islands including Bonaire. Bonaire is one of the six Dutch Caribbean islands with the most extensive blue carbon ecosystem. Blue carbon ecosystems, like mangroves and seagrasses, can capture and store large amount of carbon in plants and subsurface, thus contributing to mitigating climate change and global warming effect (Tamis & Foekema, 2016). Besides, blue carbon systems have high biodiversity values by providing food and shelter for various coastal and in coastal water communities (Croft-Cusworth, 2018). The 2018 Sargassum invasion covered the entire shorelines and beaches of Bonaire with rotting seaweed, which repel tourists. More importantly, accumulation of dead Sargassum in mangrove stands and in coastal waters deprived the area from oxygen resulting to die-offs of fishes and seagrass patches and damage to the mangrove ecosystem (Moons, 2018). Impacted seagrass areas may take several years to recover or may be lost completely if large-scale Sargassum continue to wash up (Van Tussenbroek et al., 2017).

The discovery of the great Atlantic Sargassum belt as a new source region followed by recurring large-scale beaching of Sargassum bring up concerns for the future of Bonaire and its coastal ecosystems. Measures must be taken to prevent irreparable damage on the coastal ecosystems due to Sargassum influx. STINAPA, the national park authority on Bonaire, has drafted a work plan together with the local government that explains the actions to be taken during future Sargassum influx events (Dutch Caribbean Nature Alliance, 2019). Clear protocols when a Sargassum influx is a disaster are still missing. Therefore, an early detection and monitoring system for Sargassum beaching is crucial for defining the extent and impact of Sargassum strandings on the coast (Hinds et al., 2016).

Early studies on satellite detection of pelagic Sargassum in the ocean utilized the Medium Resolution Imaging Spectrometer (MERIS) and Moderate Resolution Imaging Spectroradiometer (MODIS) Terra and Aqua sensors (Gower et al., 2007; Gower & King, 2008; Gower et al., 2013). The MERIS sensor on-board of the Envisat satellite was operational from 2002 to April 2012. MERIS operated at a spatial resolution of 1200 or 300 m, while MODIS operates at 250, 500 and 1000 m depending on selected bands. Sargassum patterns can be detected using, for instance, the infrared spectrum typical of vegetation (Gower et al., 2007). However, mixed signals between Sargassum and surrounding coastal features, such as mangrove forest, may occur when Sargassum patches are too small, partially submerged or sparsely distributed. This increases the need for higher spatial- and spectral resolution data to discriminate surface features from Sargassum. Midwood and Chow-Fraser (2010) used IKONOS satellite data (3.28 m) to detect floating vegetation in Canada. A similar study was done by Siddiqui and Zaidi (2015) using Worldview-2 satellite data (1.84 m) to detect seaweed along Karachi Coast. However, very high spatial resolution satellite data like IKONOS and Worldview-2 are only commercially available, making such data sources less attractive for frequent monitoring of Sargassum. The new Sentinel-2 mission provides free and global satellite data with a spatial resolution up to 10m in the visible spectrum and a revisit time of five days. Therefore, the use of the Sentinel-2 satellite platform might be excellent for monitoring Sargassum and assessing the impact of it on the ecosystems in coastal regions. This thesis will therefore assess the use of Sentinel-2 for monitoring Sargassum and seagrass on Bonaire.

1.3 Objectives

The main objective of this research is to use high-resolution multispectral Sentinel-2 data to detect and map Sargassum patches on open sea and the east coast of Bonaire. Accurate Sargassum maps will be useful information for the coastal authorities to assess the location and coverage of Sargassum mats that have washed up along the shores and beaches. Consequently, the extent to which these Sargassum seaweeds affect nearshore benthic habitats and coastal ecosystems in east Bonaire can be evaluated too. Detection of free-floating vegetation in the ocean has been done by many researchers around the world, using different methods and earth observation satellite sensors. In this study, the research questions will focus on finding the most suitable method to classify and assess the impact of pelagic Sargassum on coastal ecosystems using open source Sentinel-2 multispectral imagery.

The purpose of this study is to demonstrate the effectiveness and limitations of spaceborne Sentinel-2 optical satellite imagery for the detection of Sargassum on open sea and on the coast based on their spectral image characteristics. This research will also evaluate the possibility of the multispectral sensor data for mapping coastal ecosystems, such as seagrass distribution on the east coast of Bonaire. A seagrass distribution map is important for evaluating the impact of Sargassum events on the quality of such an ecosystem.

1.4 Research questions

Based on the objectives, the following research questions are formulated:

RQ 1. To what extent can Sargassum patches be classified on the coast and coastal waters of Bonaire using Sentinel-2 imagery?
RQ 2. To what extent can floating Sargassum patches be classified on open sea using Sentinel-2 imagery?
RQ 3. Can the impact of Sargassum on seagrass distribution in Lac Bay be mapped with Sentinel-2?

1.5 Thesis structure

This thesis is structured in five chapters. Chapter two describes the study area and general research approach with respect to each objective. This chapter also elaborates on several image classification techniques used in this study. Classification maps and analysis results are presented in chapter three, whereas chapter four discusses the used methodology and research findings. Finally, the conclusions from this study are given in chapter five which includes a few recommendations.

Chapter 2 Data and methods

2.1 Study area

2.1.1 Overview

Bonaire (12° 12' 6.8040'' N, 68° 15' 44.5788'' W) is one of the six Dutch Caribbean islands located about 70 kilometers from the north coast of Venezuela. The island has a semi-arid climate which receives about 463 mm of precipitation annually. Bonaire's tropical region has dry and wet seasons which span from February to June and September to January, respectively (Homan, 2017). Two important mangrove sites: Lac Bay and Lagun can be found on the wind faces east coast of Bonaire.

With an area of about 700 hectares, Lac Bay is a shallow non-estuarine bay that supports valuable habitats for mangrove forests, seagrass pastures, corals, sea turtles, fishes and invertebrates. Lac Bay is a protected Ramsar site and Important Bird Area (IBA) (Bettencourt & Imminga-Berends, 2015). Ramsar sites are wetlands that are designated by 170 countries under the Ramsar convention to be protected and managed sustainably (Van Dam, 2019). The lagoon has a maximum water depth of 4.5 m and a tidal range of about 0.3 m (Van Moorsel & Meijer, 1994). The lagoon is protected from the open sea by a shallow coral barrier on the east side of Lac Bay. Sorobon beach, situated southwest of Lac Bay, is a popular leisure site that provides access to the shallower water area inside the coral dam. The shallower water site (1.5 m) is designated for snorkeling and windsurfing (STINAPA Bonaire, n.d.). A smaller bay area named Lagun located north of Lac Bay also functions as an IBA site. The smaller mangrove stands in this site also suffer from recurring Sargassum brown tides.

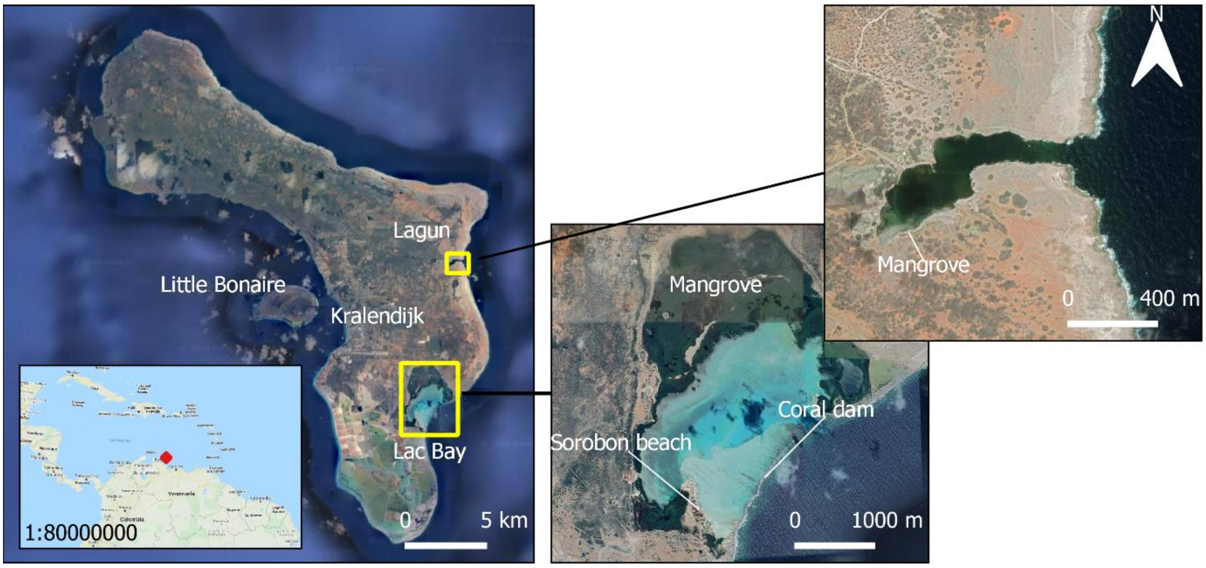

Figure 1. Location of the study area. The mini map and satellite image on the left shows the extent of Bonaire and its location in the Caribbean Sea (red). The satellite images on the right show subsets of Lac Bay and Lagun. Mini map and satellite image by Google Maps ®.

2.1.2 Impact of Sargassum brown tides

The east coast of Bonaire has been severely impacted by recent Sargassum brown tides since this part of the island is exposed to the prevailing easterly trade winds (National Oceanic and Atmospheric Administration, 2017). STINAPA and the local government have put effort to contain the brown tide at Lagun by using a floating boom (see figure 2). However, such measures are temporarily and difficult to deploy on larger bay area such as Lac. Accumulation of dead Sargassum deprives the area of oxygen, which leads to visible die-offs of mangrove trees and seagrass as shown in figure 3. Moreover, decomposing organic matter results into murky waters which limit light reaching deeper waters and further impeding the growth of seagrass meadows.

Figure 2. Thick brown Sargassum mats floating near the beach. Left picture shows a floating boom used by STINAPA and local government to contain Sargassum brown tied at Lagun during the invasion in March 2019. Right picture shows Sargassum flooding the mangrove stands at Sorobon during the invasion in March 2018. Pictures retrieved from (Bonaire Nu, 2018, 2019).

Figure 3. Examples of healthy (top row) and dead (bottom row) seagrasses and mangroves at Lac Bay during the invasion in 2018. Photos by Luuk Leemans, retrieved from (Radboud Universiteit, 2019).

A summary of recent Sargassum reports, including possible clean-up date, in Bonaire is shown in table 1. These reports were considered during selection of Sentinel-2 imageries.

Table 1. Sargassum beaching reports between 2017 and 2019. Information adapted from https://bonaire.nu/?s=sargassum%20.

Date	Site	Description	Possible clean-up date
25 December 2017	Mostly Lagun	Large-scale strandings of Sargassum at Lagun. High mortality of juvenile sea turtles, lobsters and fishes during this event. STINAPA, Junior Rangers and volunteers were involved in clearing the area. Possible first landing 1-2 days earlier.	27 January 2018
6 March 2018	Lac Bay, Lagun	Massive Sargassum invasion in the first week of March at Lac Bay and Lagun. High priority to clear seaweed at Lac Bay Sorobon and Lagun. Subsequently, other coastal sites (e.g. Boka Washikemba and Kaminda). STINAPA, local government, volunteers and coast guards were involved in clearing the area. Possible first landing 1-2 days earlier.	7, 8 and 9 March 2018 at Sorobon and Lagun. Following few weeks at areas surrounding Sorobon and other coastal sites.
19 July 2018	Mostly Lagun	Sargassum influx at Lagun and other coastal areas. STINAPA employees were involved in clearing up the site.	20 July 2018
6 March 2019	Lac Bay, Lagun	Large-scale Sargassum influx at coastal areas of Bonaire. STINAPA and the port warden set up seaweed booms at a few mangrove areas in Lac Bay. Possible first landing 1-2 days earlier.	6 March 2019
10 May 2019	Lac Bay, Lagun	Large-scale Sargassum influx at coastal areas of Bonaire. STINAPA and volunteers were involved in clearing the Sargassum on Sorobon beach.	11 May 2019

The next paragraphs elaborate on the data and approaches to map Sargassum and seagrass. Section 2.2 explains the technical specifications and pre-processing of Sentinel-2 images, whilst section 2.3 addresses the supervised and unsupervised image classification techniques used in this study. Section 2.4 explains how to assess the classification accuracy. Finally, section 2.5 summarizes the general research approach and objectives with respect to the research questions.

2.2 Sentinel-2 data

2.2.1. Sentinel-2 instrumentation

Sentinel-2 is one of a series of Earth observation satellite missions developed by the European Space Agency (ESA) under the Copernicus program to monitor land- and sea surface conditions and the atmosphere. The Sentinel-2 mission includes two polar-orbiting satellites released in 2015 (Sentinel-2A) and 2017 (Sentinel-2B). Consequently, a revisit time of five days (at the equator) can be achieved using both satellites and ten days with one satellite. Both missions have an operational life expectancy of seven years. Each satellite supports a Multispectral Instrument (MSI) which is a push-broom type of sensor that records rows of multispectral image data along the flight track. A single Sentinel-2 scene covers a swath width of 290 kilometers. Furthermore, the instrument can measure thirteen spectral bands at 10, 20- and 60 meters ground resolution (European Space Agency, 2015). The full Sentinel-2 MSI band specifications are summarized in table 2.

Table 2. Sentinel-2 Multispectral Instrument band specifications. Note that the native 10m resolution bands are provided in 20m and 60m resolutions as well, whereas the native 20m bands are also available in 60m. Band B10 (highlighted in yellow) is used for atmospheric correction in the Level-1C product and is not included in the Level-2A product.

Band	Band Description	Wavelength range (nm)	Central wavelength (nm)	Ground resolution (m)
B01	Coastal aerosol	433 – 453	443	60
B02	Blue	458 – 523	490	10
B03	Green	543 – 578	560	10
B04	Red	650 – 680	665	10
B05	Vegetation Red-Edge	698 – 713	705	20
B06	Vegetation Red-Edge	733 – 748	740	20
B07	Vegetation Red-Edge	773 – 793	783	20
B08	Near-infrared	785 – 900	842	10
B8A	Vegetation Red-Edge	855 – 875	865	20
B09	Water vapor	935 – 955	945	60
B10	Shortwave infrared/ Cirrus	1360 – 1390	1375	60
B11	Shortwave infrared	1565 – 1655	1610	20
B12	Shortwave infrared	2100 – 2280	2190	20

2.2.2 Sentinel-2 data products and pre-processing

Atmospheric correction
Copernicus Open Access Hub is an online platform that provides access to free and complete Sentinel mission products. Two Sentinel-2 product types were downloaded via the platform: Level-1C and Level-2A. Level-1C data are geometrically and radiometrically corrected top of atmosphere reflectances (TOA). To assess surface properties of Sargassum accurately, an atmospheric correction is required to estimate the bottom of atmosphere reflectance (BOA) or also known as surface reflectance. Level-2A data contain atmospherically corrected surface reflectances. Note that the cirrus band B10 is not included in the Level-2A product (see table 10). Sentinel-2 Level-2A products are globally available from December 2018 onwards, whereas older Sentinel-2 data in the archive only support Level-1C products. In this study, the Sen2Cor Processor was used to pre-process level-1C data to level-2A products (Main-Knorn et al., 2017).

Cloud mask data
Additional Sen2Cor data outputs include Aerosol Optical Thickness (AOT), Water Vapor (WV) and Scene Classification (SCL) (Main-Knorn et al., 2017). The Scene Classification data contains a cloud flag that can be used to mask clouds from the imagery. However, during the study it was found that low altitude clouds were not well detected and bright coastal features like the beach and white rooftops were misclassified as clouds. This is partially due to the lack of a thermal band (Frantz et al., 2018) . Therefore, cloud condition was carefully considered during scene selection and the rest of this study.

Digital Number to Surface Reflectance
The radiometric resolution of Sentinel-2 images is 12-bit, which means it can measure 4096 (2^{12}) different intensities of reflected radiance. For analysis purposes, the image data was converted to its physical unit (surface reflectance) by applying a conversion formula:

$$SR = \frac{DN}{10000} \tag{1}$$

Wherein DN (Digital Number) is the original image pixel values and 10000 the Quantification Value (European Space Agency, 2017).

Resampling
Some Sentinel-2 multiband images are only available in 20- and 60 meters resolutions. For analysis purposes, a bilinear interpolation was performed using the Rasterio Python module (Gillies & others, 2013) to resample coarse band images into 10m resolution images. This resampling method basically splits the coarse pixel into smaller pixels based on the weighted distance of four neighboring pixels. The resulting image appears smoother but preserves sharpness and surface information (Teoh et al., 2008).

2.3 Remote sensing image classification techniques

2.3.1 Supervised- and unsupervised classifications

Supervised classification
In this study, several supervised and unsupervised image classification techniques were explored for mapping Sargassum and seagrass distributions. A supervised classification requires training samples with known class types collected from the study area or image. The classifier then compares the spectral signatures of the training samples with a pixel from an image and assigns it to a class based on certain decision rules (Li et al., 2014). Recent studies have used supervised Maximum Likelihood Classification for mapping seagrass and Sargassum distributions in coastal regions (Blanco & Tamondong, 2019; Thang et al., 2020). Another study used Decision Trees to map seagrass and macroalgal in estuaries (Pe'eri et al., 2016). Both supervised techniques were explored in this study. Sections 2.3.2 and 2.3.3 explain how these classification techniques were implemented in the study.

Unsupervised classification
In an unsupervised classification, the image data is naturally clustered or segmented into unknown classes based on their spectral characteristics. Image interpretation is often required to identify or group these classes (Gumma et al., 2019). Unsupervised classification is a suitable method for detecting floating Sargassum on open sea where ground truth data are difficult to collect. Histogram thresholding or density slicing of a spectral index image was used before to identify floating Sargassum in coastal waters and open sea (Dierssen et al., 2015; Hu et al., 2015). Principle Component Analysis (PCA) is a data dimensionality reduction technique which is, to the best of the author's knowledge, never been used before for mapping floating Sargassum. A PCA combined with histogram thresholding can be an effective method to segment objects of interest in images (Akurathi, 2016; Terletzky & Ramsey, 2016). In this study, a Principal Component Analysis combined with an automatic histogram thresholding method, namely Triangle algorithm, was explored apart from density slicing of a spectral index. Section 2.3.4 explains how PCA and Triangle thresholding was implemented in the study.

2.3.2 Maximum Likelihood Classification

Maximum Likelihood Estimation
A supervised Maximum Likelihood Classifier (MLC) was implemented in Python based on Richards (2013). Maximum Likelihood Classification is a parametric method that assumes a Gaussian distribution for each class. It aims to assign every pixel in an image to a class that has the largest probability (i.e. maximum likelihood) (Miranda et al., 2018). To estimate the largest probability of a pixel to a certain class the classifier applies a Maximum Likelihood Estimation (MLE) function based on Bayes' theorem (Ballantyne, 2018; Richards, 2013):

$$\arg\max p(\omega_i|x) = \arg max\left[-ln|C_i|| - (x - m_i)^T {C_i}^{-1}(x - m_i)\right] \tag{2}$$

Wherein $p(\omega_i|x)$ the posterior probabilities that pixel x belongs to class ω_i (after analysis) and $p(x|\omega_i)$ the conditional probabilities that a given class ω_i is observed in pixel x. The prior probabilities $p(\omega_i)$ refer to the actual chance of finding a pixel from class ω_i in the image. For N-number of classes, the conditional probabilities $p(x|\omega_i)$ were estimated from training samples based on a multivariate Gaussian probability density function:

$$p(\omega_i|x) = 2\pi^{-\frac{N}{2}}|C_i|^{-\frac{1}{2}}exp\left\{-\frac{1}{2}(x-m_i)^T C_i^{-1}(x-m_i)\right\} \tag{3}$$

Substituting equation 3 into equation 2 gives:

$$arg\ max\ p(\omega_i|x) = \arg\max\left[-\frac{N}{2}ln\ 2\pi - \frac{1}{2}ln|C_i| - \frac{1}{2}(x-m_i)^T C_i^{-1}(x-m_i) + \ln p(\omega_i)\right] \tag{4}$$

For operational purposes the first term $-\frac{N}{2}ln\ 2\pi$ can be ignored, as it is not related to the analysis. Besides, if there is no a priori knowledge about the features in the study area then the last term $\ln p(\omega_i)$ can be omitted too. Consequently, all classes are assumed to have equal probabilities. Equation 4 can then be simplified to:

$$arg\ max\ p(\omega_i|x) = arg\ max[-\ln|C_i| - (x-m_i)^T C_i^{-1}(x-m_i)] \tag{5}$$

Where C_i and m_i are the estimated covariance matrix and mean vectors for each class ω_i in the training samples, $|C_i|$ the determinant of the covariance matrix, C_i^{-1} the inverse of the covariance matrix and $(x-m_i)^T$ the transposed vector of $(x-m_i)$. Finally, the $arg\ max$ operator dictates the class membership ω_i based on the largest posterior probability with respect to its estimated probability density function.

Chi-square threshold

Misclassification of pixels may occur if the class distributions overlap. A threshold can be set to bound the maximum distance to which pixels are assigned to a class. Consequently, pixels outside this bound are assigned to a rejection class. The threshold rule (for equal prior probabilities) is defined as:

$$arg\ max\left[-\ln|C_i| - (x-m_i)^T C_i^{-1}(x-m_i)\right] > arg\ max\ [-\chi^2 - ln|C_i|] \tag{6}$$

Wherein χ^2 is the critical chi-square value for N degrees of freedoms (= input bands) (Swain & Davis, 1978). In this study, MLC models with chi-square probabilities (see table 3) of 10%, 20% and 50% (hereinafter referred to as $\text{MLC}_{\text{probability\%}}$) were investigated apart from the base (= 0% probability) model (hereinafter referred to as MLC_{Base}). For example, the $\text{MLC}_{20\%}$ model implies that a pixel is classified if it falls within 80% of the class distribution or else the pixel is rejected The MLC_{Base} model classify every pixel one the image, hence each pixel must belong to a class.

Table 3. Reference table with critical chi-square values for eight different degrees of freedom

Probability	**1**	**2**	**3**	**4**	**5**	**6**	**7**	**8**
0.50	0.455	1.386	2.366	3.357	4.351	5.348	6.346	7.344
0.20	1.642	3.219	4.642	5.989	7.289	8.558	9.803	11.03
0.10	2.706	4.605	6.251	7.779	9.236	10.645	12.017	13.362

2.3.3 Decision Tree Classification

Decision Trees

Decision Trees are a non-parametric method that recursively split the feature space (e.g. spectral bands) based on given training samples. It tries to stratify the training data with mixed classes into homogeneous classes while minimizing the variance in each class (Kingsford & Salzberg, 2008). The algorithm aims to find the best features in the dataset that can separate the classes. An example of a decision tree diagram is shown in figure 4. A Decision Tree consists of a root node, decision nodes and leaves. The root represents the entire population or a set of training samples, whereas decision nodes are sub-nodes that can split into more nodes or end at a leaf (= final class).

Decision Tree Classifier

In this study, a supervised Decision Tree Classifier from the Scikit-Learn Python module was used (Pedregosa et al., 2012). The classifier has many parameters that can be tuned. A list of Scikit-learn parameters that were considered is listed in table 4. In this study, the Entropy was widely used as splitting criterion:

$$Entropy\ (bits) = -\sum_{i=1}^{N} P_i\, log_2 P_i \tag{7}$$

Where P_i is the probability of class i appearing in a dataset with N number of classes (Zhou, 2019). The Entropy can also be used in a spatial context for mapping the uncertainty of the MLC results based on the class-posterior probabilities $p(\omega_i|x)$ (Maselli et al., 1994).

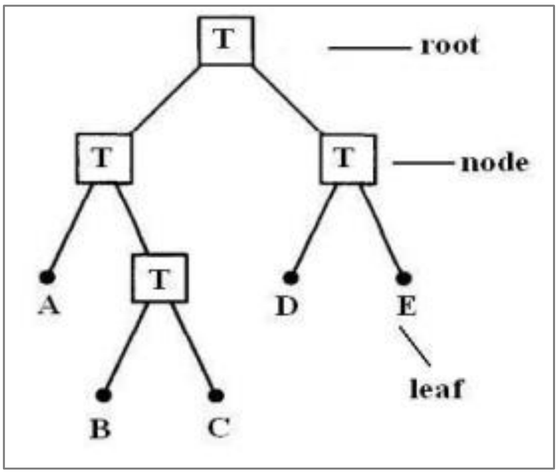

Figure 4. Example of a decision tree diagram. Figure adapted from (Pooja et al., 2011).

Table 4. Scikit-learn Decision Trees parameters considered in this study.

Parameter name	Description
max_depth	Maximum depth of tree. A larger number increases the complexity of the tree.
min_samples_split	Minimum number of samples required to split a node.
max_leaf_nodes	Maximum number of leaf nodes (final classes) allowed.
min_samples_leaf	Minimum number of samples required at each leaf node.
min_impurity_decrease	A purity threshold that is used when splitting a node.
criterion	The splitting criterion (Gini or Entropy).

Tuning a Decision Tree Classifier

A stratified K-fold cross validation was performed to tune the Decision Tree Classifier (DTC). A K-fold cross-validation partitions the input data into K (=10) number of training and validation subsets. For each K iteration, a subset was used as validation, whereas the rest (K-1) were used for training the classifier (Piragnolo et al., 2017). Subsequently, the training and validation accuracies were computed for plotting a validation curve (see example figure 5). This validation curve was used to assess the influence of the training samples with increasing model complexity (i.e. parameter value). Attention was given to parameter values that best balance bias and variance. A high bias versus low variance indicates underfitting, whereas low bias versus high variance indicates overfitting (Scheunders et al., 2018). Note that that the parameters listed in table 3 were evaluated individually using the default Scikit-Learn settings.

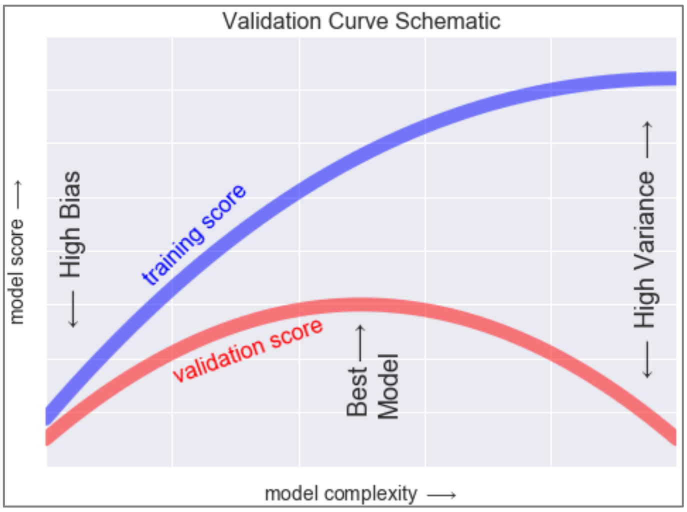

Figure 5. Example of a validation curve depicting training and validation accuracies (scores). Figure adapted from (VanderPlas, 2016)

2.3.4 Image Segmentation of Principal Component Image

Principal Component Transformation

A Principal Component Analysis (PCA) is an unsupervised method that aims to reduce redundant information in the data. This is done by transforming a set of intercorrelated variables (e.g. Sentinel-2 bands) into fewer uncorrelated random variables, namely Principal Components (Torbick & Becker, 2009) (see example figure 6). Each component contains a specific piece of information from the original image. This information can be associated with meaningful surface features such as land and vegetation or noise like sun-glints and clouds. Hence, a Principal Component image can help visually enhance floating Sargassum on the image. The Principal Components for N number of components (= input Sentinel-2 bands) can be expressed in its simplest form as (Estornell et al., 2013):

$$Y_N = Wx = \begin{pmatrix} w_{1,1} & \cdots & w_{1,N} \\ \vdots & \ddots & \vdots \\ w_{N,1} & \cdots & w_{N,N} \end{pmatrix} \begin{pmatrix} x_1 \\ \vdots \\ x_N \end{pmatrix} \tag{8}$$

Wherein W is the transformation matrix and x the band vector from the original data. The coefficients of the transformation matrix refer to the Eigenvector loadings or also known as Principle Component scores. The scores pertain to the direction of the components. It is also an estimate of the influence of the bands in each Principal Component (Gupta et al., 2013; Weijerman et al., 2005). The Eigenvectors are ordered by the Eigenvalues which is the proportion of the original information (i.e. explained variance ratio) retained in each Principal

Component. Hence, most of the information can be found in the first few components which account for the largest explained variances in the data. In this study, a Principle Component Analysis from the Scikit-Learn Python module was used (Pedregosa, 2012). It should be noted that Scikit-Learn normalizes the data by centering the components around mean of zero.

Triangle based image thresholding

A linear combination of normal random variables is normally distributed (Hearn & Metcalfe, 1995). This is also true for Principal Components; hence PC image data are unimodal. The peak of such distribution represents the dominant feature in the image such as land or sea surface pixels (i.e. the background). Contrarily, meaningful objects like floating Sargassum are found in the lower tail of the distribution. In this study, an image based Triangle method from Scikit-Image Python module (van der Walt et al., 2014; Zack et al., 1977) was used. The Triangle algorithm is specially designed for threshold detection of a unimodal distribution. The algorithm estimates the cut-off point by finding the largest distance that lies perpendicular between the maximum and minimum line of the histogram (see example figure 7). The histogram value at which the largest distance is found best separates objects from its background, resulting into binary image segments for example: Sargassum or non-Sargassum.

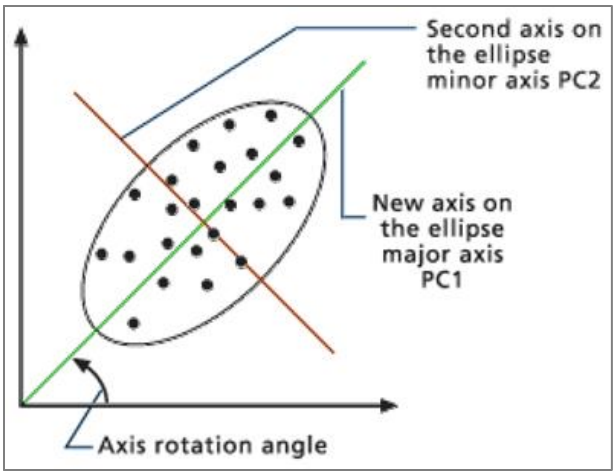

Figure 6. Example scatterplot between two variables. The green and red lines refer to the first and second Principal Components. Figure adapted from (ESRI, n.d.).

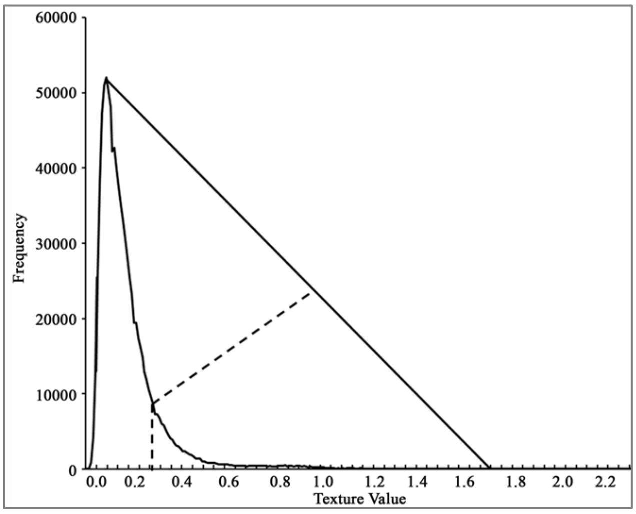

Figure 7. Example illustration of the Triangle method for determining threshold value in a unimodal distribution. Figure adapted from (Terletzky, 2016).

2.4 Accuracy assessment

An accuracy assessment was done to evaluate the model and predictive performances of the Maximum Likelihood and Decision Tree classifiers with respect to the training samples. In this study, a confusion matrix (see example table 5) was used to derive several classification accuracies.

Table 5. Example of a confusion matrix

		Observed	
		Sargassum	**Non-Sargassum**
Classified	**Sargassum**	True Positive (TP)	False Positive (FP)
	Non-Sargassum	False Negative (FN)	True Negative (TN)

$$Overall\ accuracy\ (OA, MA, VA) = \frac{TP + TN}{TP + FP + FN + TN} \tag{9}$$

$$Producer's\ accuracy\ (PA) = \frac{TP}{TP + FN} \tag{10}$$

$$User's\ accuracy\ (PA) = \frac{TP}{TP + FP} \tag{11}$$

$$F1\ score = \frac{2 * PA * UA}{PA + UA} \tag{12}$$

Wherein True Positive (TP) and True Negative (TN) refer to the cost of correct classifications, whereas False Negative (FN) and False Positive (FP) are the cost of misclassifications (Lai & Tsai, 2019).

The overall accuracy (OA) pertains to the proportion between number of correctly classified samples and total number of samples. Also, this study makes a distinction between model accuracy (MA) and validation accuracy (VA). The model accuracy was computed based on the training samples to which the classifier is trained upon. The validation accuracy was acquired from independent external samples. Both are calculated the same way as the overall accuracy.

The producer's- and user's accuracies describe how well the pixels are classified on an image and the probability that the classified pixels are indeed found in the field (Ismail et al., 2009). The F1 score is the harmonic mean between producer's- and user's accuracies. For coastal managers, the user's accuracy is particularly important because they need to be certain of the information on the ground, for example before dispatching park rangers to the Sargassum affected locations.

2.5 Research approach and objectives

The general research approach with respect to each objective is explained in this paragraph. Section 2.5.1. pertains to research question 1, whereas sections 2.5.2 and 2.5.3 refer to research questions 2 and 3, respectively. An overview of the approach is illustrated in figure 15 on page 23.

2.5.1 Classifying Sargassum on the coast and coastal waters

Sampling strategy for classifying Sargassum

A supervised classification was performed to classify Sargassum on the coast and coastal waters. A labelled dataset is required to train the DTC and MLC. In this study, training samples were collected from four Sentinel-2 imageries taken during the invasion in March 2019 (4, 9, 14 and 19 March). Training sites covering eight classes were drawn to extract reference pixels from each scene. The eight classes are described in table 6.

Table 6. Description of classes used in this study

Class name	Abbreviation	Description
Floating Sargassum	Sf	Floating Sargassum mats found on water surface
Sargassum on land	Sl	Sargassum mats found stranded on the coastline
Beach	Lb	Bright sand pixels on Sorobon and along the coast
Soil	Ls	Brown soil pixels mostly found north of Lac Bay and around Lagun
Mangrove	Vm	Mangrove trees found on Lac Bay and Lagun
Other vegetation	Vo	Vegetation other than mangrove
Deep water	Wd	Dark pixels found on deep waters
Shallow water	Ws	Shallow water pixels found on Lac Bay and along the coast

Sargassum rafts have been reported to mainly have struck the southwest part of Lac Bay and the inland bay area of Lagun where they accumulate on beaches. Sargassum rafts have also been washing off along the shoreline on the east coast of Bonaire. A 200-meter buffer surrounding the east shoreline of Bonaire was created to limit the extent of the study area to this region of interest. Greater parts of Lac Bay and Lagun were also included in this region. Figure 8 shows the extent of the region of interest along with some examples of the training sites.

Spectral indices

Several spectral indices to classify Sargassum were considered in this study (see table 7). Spectral indices can aid in class discrimination based on the sensitivity of the classes toward specific band wavelengths. These indices also help in reducing soil and background reflectances which can cause misclassifications (Fang & Liang, 2014). The indices were widely used for detecting seaweed (SEI, FAI), algal blooms (VB-FAH, SABI) and studying vegetations (NDVI, REP, GNDVI). The GNDVI is identical to the NDWI by McFeeters (1996) which is widely used for mapping water bodies. The Floating Algae Index (FAI) is developed by Hu (2009) for detecting floating Sargassum on open sea. The original FAI uses a band centered at 1240nm, but a band centered at 1640nm can be used as well according to Hu (2009). Additionally, Sentinel-2 band B8A (865nm) was investigated as an alternative for B8 (842nm) in the NDVI because the band is narrower (see table 2) and might be more sensitive towards certain classes.

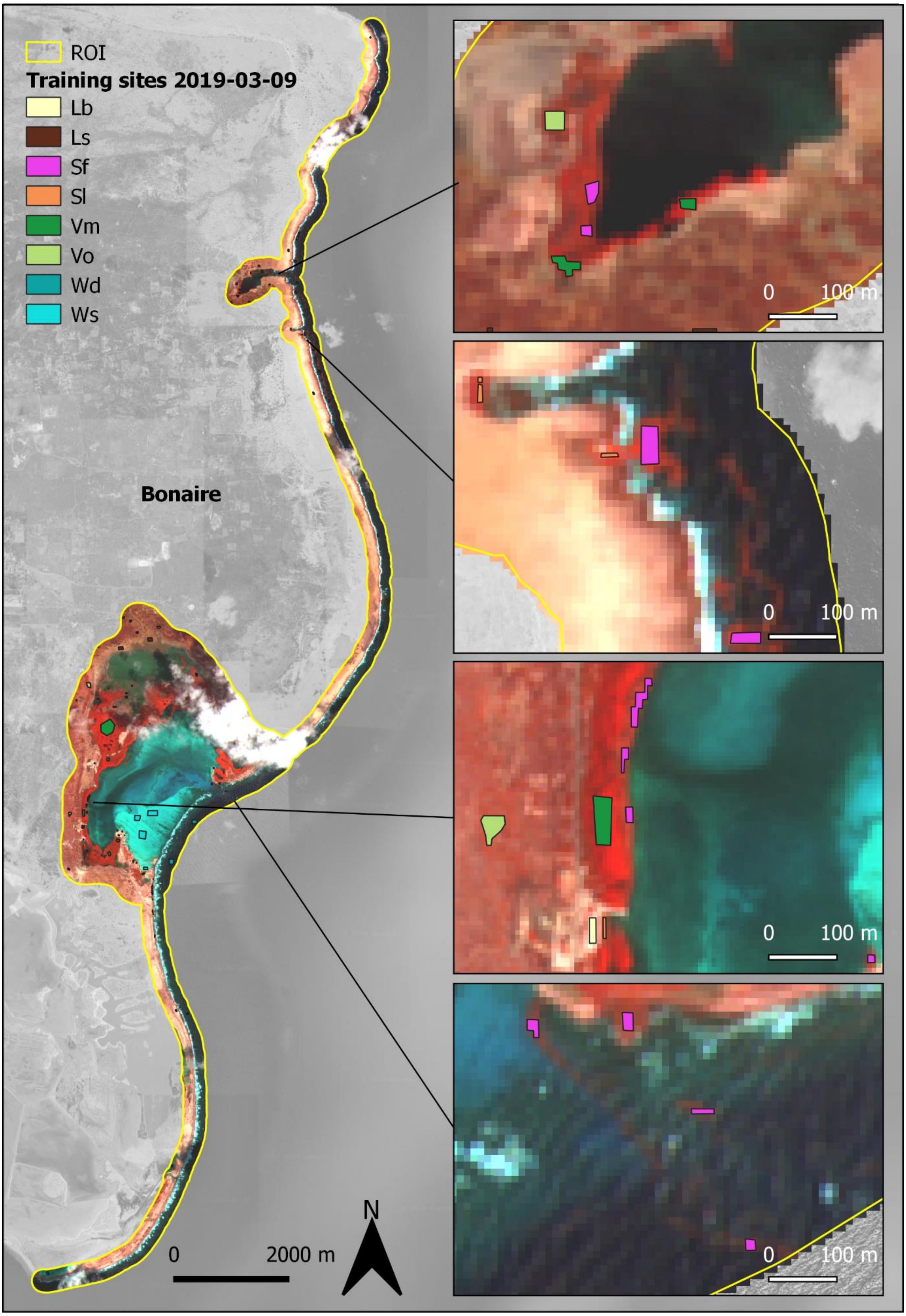

Figure 8. Region of interest (ROI) depicting east shoreline of Bonaire. An example false colour composite (bands 8, 3 and 2) is shown for a scene taken on 9 March 2019. Vibrant red pixels are associated with vegetation or Sargassum. The training sites for Sargassum (Sf and Sl) and other classes are also displayed for multiple subsets in the ROI. Grayscale base map by Google Maps ®.

Table 7. Spectral indices considered in this study. The formulation is noted according to the Sentinel-2 band central wavelength (nm).

Index	Name	Formulation	Reference
NDVI	Normalized Difference Vegetation Index	$\frac{(R_{842} - R_{665})}{(R_{842} + R_{665})}$	(Rouse et al., 1973)
NDVI B8A	“”	$\frac{(R_{865} - R_{665})}{(R_{865} + R_{665})}$	“”
REP	Red-Edge Position	$705 + 35\frac{(\frac{R_{665} + R_{783}}{2}) - R_{705}}{(R_{740} + R_{705})}$	(Guyot & Frederic, 1988)
GNDVI	Green Normalized Difference Vegetation Index	$\frac{(R_{842} - R_{560})}{(R_{842} + R_{560})}$	(Gitelson et al., 1996)
FAI	Floating Algae Index	$R_{842} - R_{665} + (R_{1610} - R_{665})0.187$	(Hu, 2009)
VB-FAH	Virtual-Baseline Floating macroAlgae Height	$(R_{842} - R_{560}) + (R_{560} - R_{665})0.614$	(Xing & Hu, 2016)
SEI	Seaweed Enhancing Index	$\frac{(R_{865} - R_{1610})}{(R_{865} + R_{1610})}$	(Siddiqui et al., 2019)
SABI	Surface Algal Bloom Index	$\frac{(R_{865} - R_{665})}{(R_{490} + R_{560})}$	(Alawadi, 2010)

Feature selection process
All twelve Sentinel-2 bands including eight spectral indices shown in table 5 were considered as input features for the DTC and MLC models. The Jeffries-Matusita distance was used to calculate the separability between the classes with respect to each input feature. The Jeffries-Matusita distance uses the Bhattacharyya distance as separability measure under the assumption that each class is normally distributed. The Bhattacharyya distance (B) between two classes is expressed as (Nussbaum & Menz, 2008):

$$B = \frac{1}{8}(m_1 - m_2)^2 \frac{2}{\sigma_1^2 + \sigma_2^2} + \frac{1}{2} ln \left[\frac{\sigma_1^2 + \sigma_2^2}{2\sigma_1\sigma_2}\right] \qquad (13)$$

Where m_i and σ_i^2 (i = 1,2) are the estimated mean and variance for two arbitrary classes in the training samples.
Subsequently, the Jeffries-Matusita distance (J) can be derived:

$$J = 2(1 - exp\{-B\}) \qquad (14)$$

This produces a separability score between 0 (not separable) and 2 (completely separable). Input features with high separability scores were used in the DTC and MLC models. Special attention was given to the separability of both Sargassum classes (Sf and Sl).

Accuracy assessment of Sargassum classification
The model- and predictive performances of the DTC and MLC models were evaluated based on the accuracy metrics explained in section 2.4. The classifiers were trained upon 80% of the training samples. These samples were randomly selected with respect to the proportion of the classes. The remaining 20% test subset was used to calculate model accuracies (MA).

An (independent) external validation set was also used to assess the predictive performance of the classifiers. The validation points were collected visually from a scene taken on 18 May 2019 (see example figure 9). A minimum of two classes is required to assess the classification accuracy. It should be noted that only floating Sargassum (Sf) and non-floating Sargassum classes (Non-Sf) were considered in this step. 80 sample points were collected for each class. Sargassum on land (Sl) was not sampled and validated because it was more difficult to assess on the images. Contrarily, floating Sargassum (Sf) was easier to sample when inspecting images before and during the invasion. Non-floating Sargassum points were mostly associated with other coastal features or classes as defined in table 6. Additionally, clouds and cloud shadows were also considered as non-floating Sargassum class.

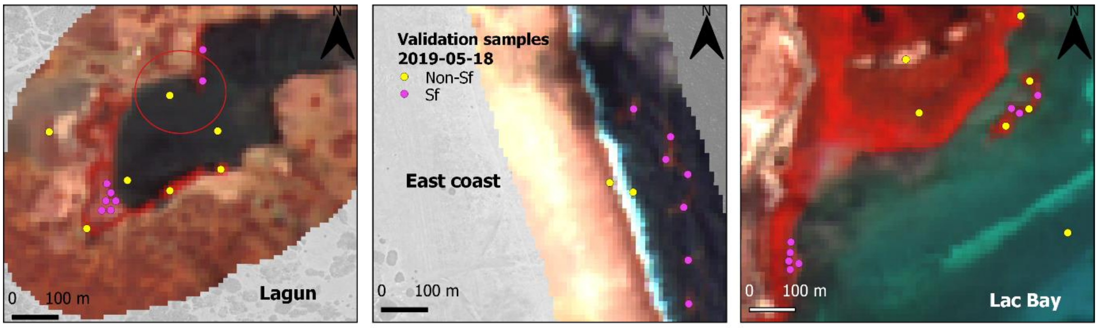

Figure 9. Floating Sargassum (Sf) and Non-floating Sargassum (Non-Sf) validation samples for a scene taken on 18 May 2019. The samples are overlaid on top of a false colour composite of the same scene

Comparative analysis of Sargassum classifications

Cross-comparison between Sargassum classified Sentinel-2 images was performed to investigate the robustness of the classifiers in detecting Sargassum across different scenes. Scenes taken from two Sargassum influx periods were investigated: 4 to 19 March and 8 to 23 May 2019. Additionally, scenes taken outside the invasion periods were also considered: 28 January, 12 February, 21 August and 29 November 2019. The total area of the classification result in hectares (ha) was used as comparative metric. For a 10m by 10m pixel the area is expressed as:

$$Total\ area\ (ha) = \frac{Number\ of\ classified\ pixels}{100} \tag{15}$$

Sargassum coverage map

Cumulative Sargassum coverage maps were calculated for scenes taken during the invasions in March 2018 and 2019 (scenes taken on 4, 9, 14 and 19 March) and May 2019 (scenes taken on 8 , 13, 18 and 23 May). A cumulative coverage map helps to allocate which part of east Bonaire is most impacted by the Sargassum influx. The Sargassum coverage maps were computed on a 20m by 20m grid based on the best model in terms of classification accuracy and robustness. The following expression was used to calculate the cumulative coverage:

$$Cumulative\ coverage\ (\%) = \frac{Average\ total\ area\ across\ scenes}{Area\ grid} \tag{16}$$

2.5.2 Classifying Sargassum in open sea

Regions of interests on open sea

Sargassum rafts apt to float towards the east coast of Bonaire due to the prevailing early trade winds. An early warning and monitoring system should be able to accurately detect floating Sargassum (Sf) before it reaches the shore. Floating Sargassum on open sea can take the form of lines or narrow slicks (Gower, 2007). Sargassum lines aligned with the wind direction are called “windrows”. These windrows are commonly found in Brazil and near the Caribbean Islands according to Ody et al. (2019). This phenomenon might pose a challenge for satellite-based monitoring systems if the slicks are sparsely distributed and most of the reflectance is attenuated by water. In this study, floating Sargassum for different sea states and cloud conditions were investigated. Seven subsets from scenes taken on 4 March 2018, 4 and 9 March, 28 April 2019 were selected. Large abundance of floating Sargassum rafts were especially observed on 4 March 2018. An overview of the sea region of interest and the selected subsets are shown in figure 10. It should be noted that the subsets were cropped from two different tile IDs namely: T19PEP (tile covers entire Bonaire) and T19PFP (tile covers eastern seas).

Unsupervised classification methods

Two different unsupervised methods to classify floating Sargassum were explored namely: density slicing of a spectral index image and PCA in combination with Triangle thresholding. In this part of the study, the Green Normalized Difference Index (GNDVI) was preferred over eight other indices listed in table 5 (see paragraph 2.5.1). The GNDVI utilizes the water penetrating green band (B03 at 560nm), hence it was presumed to be able to detect partially submerged Sargassum in water more effectively. The GNDVI uses native 10m resolution bands (B08 and B03), thus having the advantage in detecting smaller patches. The NDVI and VB-FAH were not considered since it uses the red band (B04 at 665nm) which is sensitive to turbid water (Bustamante et al., 2009; Dogliotti et al., 2015) and may cause misclassification. Also, the NDVI is prone to variable environmental and observing conditions such as clouds and viewing angle (Hu, 2009).

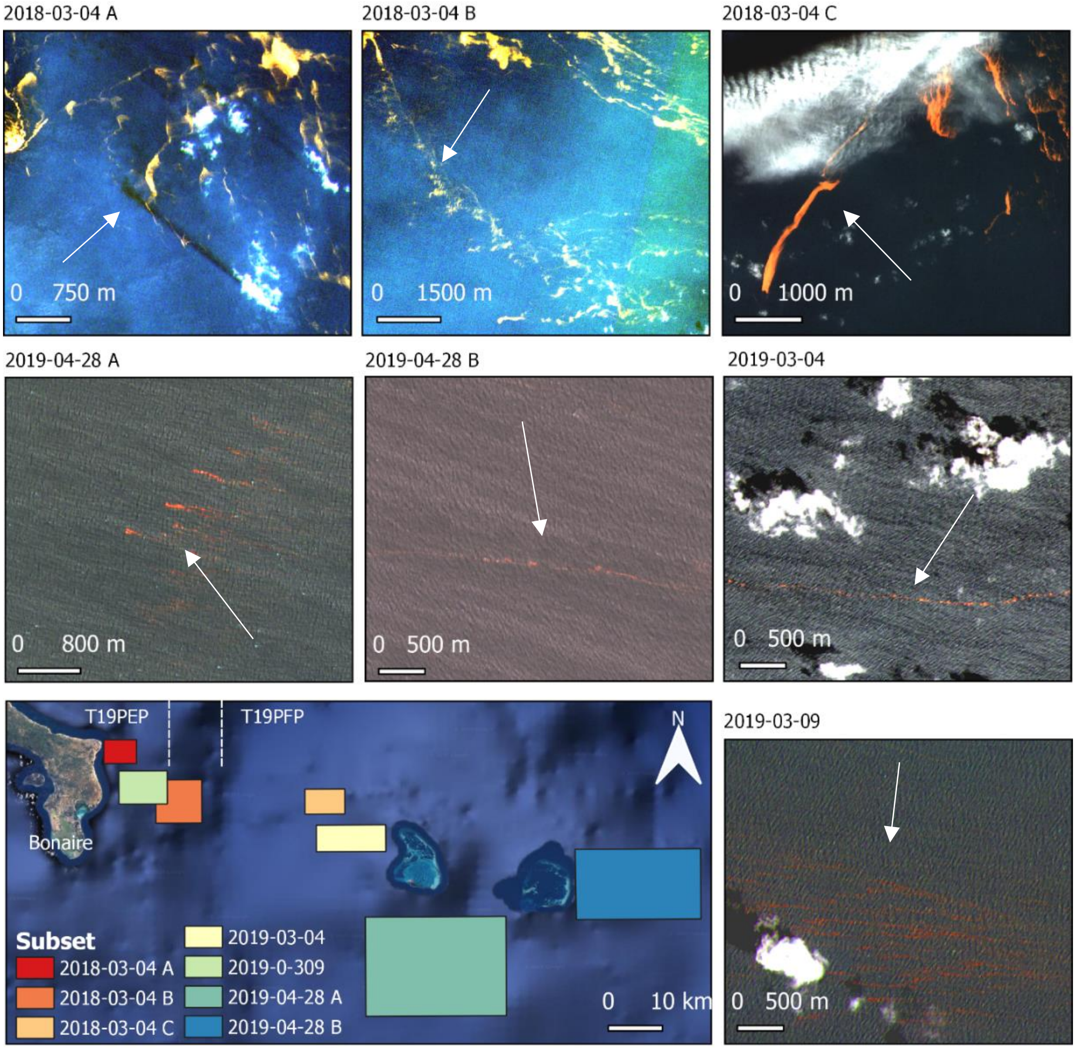

Figure 10. Subsets of image enhanced false colour composites depicting floating Sargassum (arrows) on greater east sea of Bonaire. The subsets are zoomed in to reveal Sargassum rafts more clearly. The dashed lines on the mini map show to which extent the two tiles T19PEP (tile covers entire Bonaire) and T19PFP (tile covers eastern seas) overlap each other. Mini map by Google Maps ®.

GNDVI images were derived for each subset and the most suitable threshold value to segment the image was defined based on image interpretation. The threshold value indicates the minimum GNDVI value to separate Sargassum patches from the background (i.e. water surface, clouds and other noise). Attention was given to the sea state and cloud condition in each scene, which affect the visibility of Sargassum slicks on the water surface. The results of this method are referred to as $\text{GNDVI}_{\text{Slice}}$ hereinafter.

A PCA with five components was performed for each subset. All Sentinel-2 bands, except B01 (443nm), B09 (945nm) and B10 (1375nm) were used as input images in the analysis. These bands were not used due to their coarse spatial resolution (60m) and sensitivity towards water vapor which limit the detection of Sargassum on open sea. Subsequently, the principal component images were visually inspected for each subset. Special attention was given to the PC images that support high contrast between floating Sargassum and the background (i.e. water surface, cloud and other noises). These images were then segmented using Triangle thresholding. The results of this method are referred to as $\text{PCA}_{\text{Triangle}}$ hereinafter.

Comparative analysis of floating Sargassum on open sea

Cross-comparison between Sargassum classified Sentinel-2 images was performed to investigate the robustness of the unsupervised GNDVISlice and $\text{PCA}_{\text{Triangle}}$ methods in detecting Sargassum across different scenes. Additionally, the supervised DTC and MLC models were also used to classify Sargassum on open sea. The total area (equation 15) of each classification result was used as comparative metric.

Scalability of classification methods

The performances of the $\text{GNDVI}_{\text{Slice}}$, $\text{PCA}_{\text{Triangle}}$, DTC and MLC classification methods were tested for larger subsets. The same scenes taken on 4 March 2018, which include Sentinel-2 tile IDs T19PEP and T19PFP, were classified. Note that subsets A and B from 4 March 2018 were part of the scene with tile ID T19PEP, whereas subset C was part of tile ID T19PFP. A false colour composite of the subsets combined is shown in figure 11. The two tiles overlap each other; hence each tile was classified individually and then merged using first layer priority. Subsequently, the total areas of the classification results were compared. It should be noted that the land and coastline, up to 200-meter into the sea, was masked from the final classification result.

Additionally, the best classification method in terms of robustness was compared with the Adapted Floating Algae Index (AFAI) product from the Sargassum Watch System (SaWS) (University of South Florida Optical Oceanography Lab, n.d.). The Sargassum Watch Systems provide a general outlook of floating Sargassum condition in the Caribbean and central West Atlantic using a Moderately Resolution Imaging Spectroradiometer (MODIS) sensor among others. The original FAI, investigated for coastal waters (see paragraph 2.5.1), is sensitive to clouds. Hence, the AFAI was developed by Wang and Hu (2016) for MODIS data only. The AFAI is calculated by using MODIS 1000m spatial resolution spectral bands centered at 667nm, 748nm, 869nm.

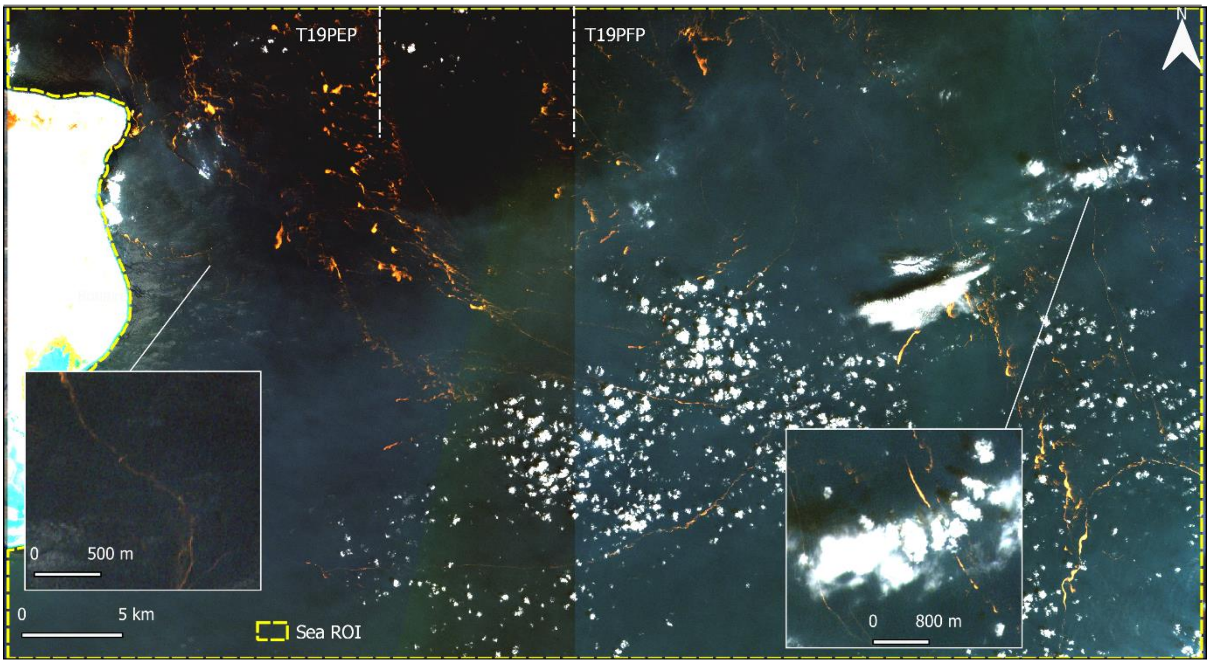

Figure 11. Combined false colour composites of two scenes taken on 4 March 2019 with tile IDs T19PEP and T19PFP. Large Sargassum rafts float at about 30km from the east coast of Bonaire. Image enhancement was applied on each scene to emphasize floating Sargassum. The white dashed lines indicate up to where the two tiles overlap. The sea region of interest is 59 km by 32 km large.

2.5.3 Classifying seagrass in Lac Bay

Sampling strategy for classifying seagrass

Lac bay supports an extensive habitat for seagrasses. Four seagrass native species can be found in the lagoon: *Thalassia testudinum* (turtle grass), *Syringodium filiforme* (manatee grass) *Halodule beaudettei* (shoal grass) *and Ruppia maritima* (wigeon grass). The most dominant species in Lac Bay are turtle and manatee seagrasses. Since 2010, an invasive and fast growing seagrass species *Halophila stipulacea* (halophila) was also observed (Engel, 2013). Figure 12 shows an example of turtle grass and halophila. In this part of the study, supervised classifications (DTC and MLC) were explored for mapping seagrass distribution regardless of species.

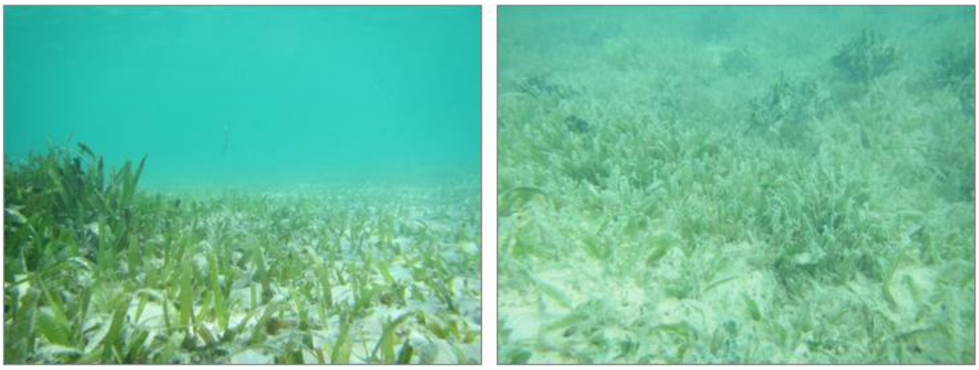

Figure 12. Example photos of turtle grass (left picture) and halophila (right picture). Photos by Marjolijn Christianen, retrieved from (Christianen, 2015).

Training samples were collected from three Sentinel-2 scenes taken on 8 and 28 January and 12 February 2019 (see example figure 13). Training sites covering two classes: seagrass and non-seagrass were drawn to extract reference pixels from each scene. Special attention was given to dark patches, which are most likely associated with seagrass. Dark patches found on the east part of Lac Bay are known coral reefs, hence these were defined as non-seagrass.

Additionally, annual seagrass monitoring data from 2019 by STINAPA Bonaire was used as reference. This data contains seagrass coverage of four species in Lac Bay: shoal grass, halophila, manatee grass and turtle grass. The seagrass coverage was sampled at 49 different locations at equi-distance interval. The measurements were done based on six 1m^2 quadrants (Verweij, 2018), thus each quadrant may contain mixed species. The samples were collected at multiple dates between 10 January and 18 February 2019.

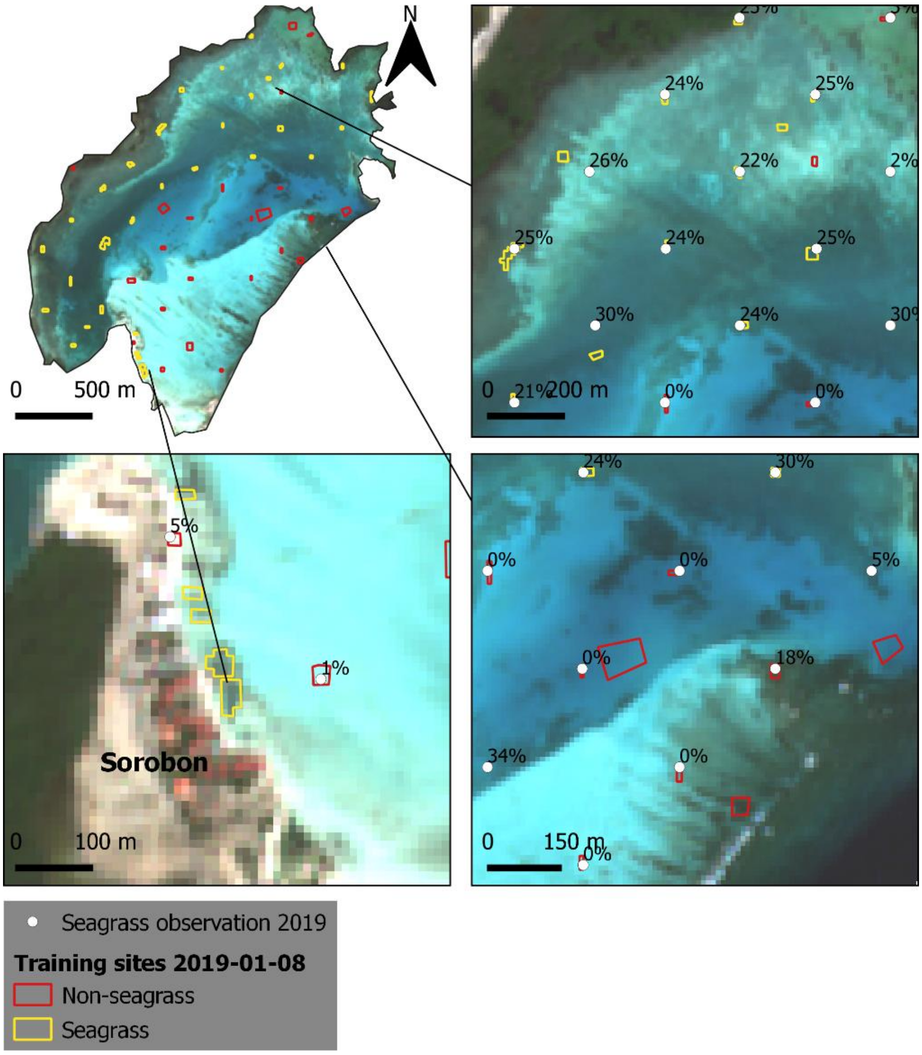

Figure 13. Location of training sites for a scene taken on 8 January 2019. Sea grass observations and training sites are overlaid on top of a true colour composite (bands 4, 3 and 2). Seagrass observations are only shown for several subsets for clarity. The observations are annotated with the mean seagrass cover (%) at each point.

Selected bands for mapping seagrass

Remote sensing of water bodies is more challenging than on land since water bodies absorb and transmit radiation. Clear water can only reflect about 10% of the incoming radiation (see figure 14). Reflected radiance is more attenuated in turbid waters. Besides, infrared radiance is fully attenuated by water, resulting into dark pixels on the image. Consequently, only spectral bands in the visible spectrum are suitable for shallow water remote sensing. In this part of the study, the red (B04 at 665nm), green (B03 at 560nm) and blue (B02 at 490nm) bands from Sentinel-2 data were used as input features for the DTC and MLC models.

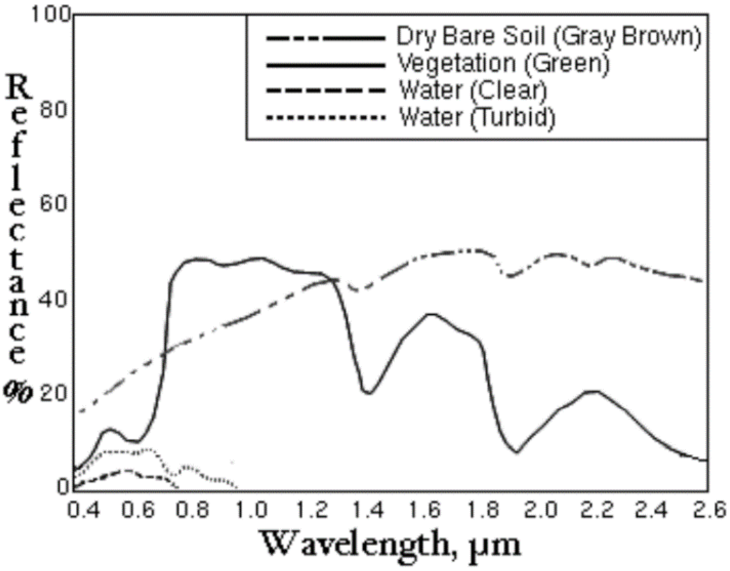

Figure 14. Typical spectral signatures of water and land features. Figure adapted from (Dalezios, 2013).

Accuracy assessment of seagrass classification
The model and predictive performances of the DTC and MLC models were evaluated based on the accuracy metrics explained in section 2.4. The classifiers were trained upon 80% of the training samples. These samples were randomly selected with respect to the proportion of the classes. The remaining 20% test subset was used to calculate model accuracies (MA).

In this part of the study, the 2019 seagrass monitoring data was used as external validation set to assess the predictive performance of the classifiers. It should be noted that the seagrass observations are labelled according to the mean coverage at each point. Points with a mean coverage greater than 0% were labelled as seagrass, else it was labelled as non-seagrass. A scene taken on 4 March 2019 was classified and validated accordingly.

Comparative analysis of seagrass distribution
Cross-comparison between Sargassum classified Sentinel-2 images was performed to investigate the robustness of the classifiers in mapping seagrass across different scenes.
Four different Sentinel-2 scenes taken on 8 January, 4 March, 21 August and 11 November 2019 were classified for seagrass and non-seagrass bottom types. Note that the scene taken on 4 March marks the start of the Sargassum influx in that month. The total classified area was used as comparative metric (see equation 15).

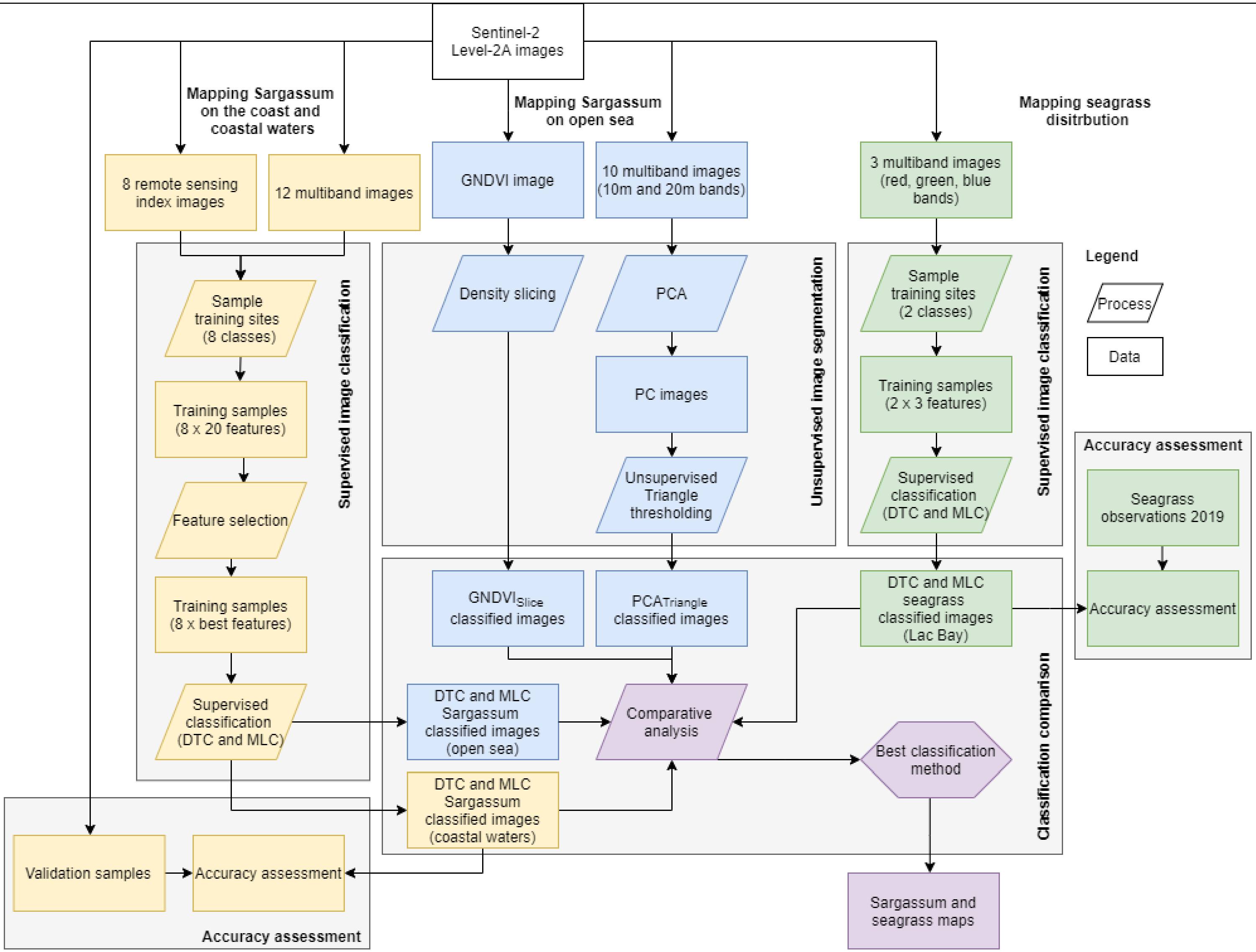

Figure 15. Flowchart diagram illustrating the general approach and objectives of this study.

Chapter 3 Results

3.1 Classification of Sargassum on the coast and coastal waters

3.1.1 Sampled dataset for Sargassum classification

Resampled dataset
Reference pixel values from multiple training sites covering eight predefined classes were obtained. The pixel values were sampled from four Sentinel-2 scenes taken during the Sargassum influxes on 4, 9, 14 and 19 March 2019. Class-imbalance was found in the collected samples, hence randomized undersampling was performed to create a more balanced dataset. This was done with respect to the sample size of the floating Sargassum (Sf) class, which was well represented on the image. Classes with sample sizes smaller than the floating Sargassum class were left intact. The resampled dataset was used for training the classifiers and further analyses in this study. Appendix 1 shows an overview of the training dataset before and after resampling. The band covariance matrices of the two Sargassum classes (Sf and Sl) are also given in this Appendix. The total number of samples in the resampled dataset is 4125 in which floating Sargassum (Sf) and Sargassum on land (Sl) accounts for 16.35% and 3.25% of the dataset, respectively.

Spectral signature
A spectral signature plot of each class is given in figure 17. Overall, the beach (Lb) has the highest reflectance compared to other classes. Deep waters (Wd) absorb most of the incoming light, hence they have a lower reflectance compared to shallow waters (Ws). Most of the visible light, especially blue and red (B02 and B03), is reflected from the bottom surface in the shallow waters of Lac Bay. Floating Sargassum (Sf) has a lower mean reflectance compared to Sargassum on land (Sl). Sargassum on land has a similar spectral curve as terrestrial vegetation (Vo and Vm), especially in the near-infrared spectrum between 740nm - 954nm (B06 -B09). However, it should be noted that B01 and B09 are in 60m resolution. Samples taken at Sorobon beach were adjacent to the water which may affect the spectral signature of these coarse resolution bands. Furthermore, most of the classes seem to separate well with B11.

3.1.2 Best input features for Sargassum classification

Heatmaps showing all the Jeffries-Matusita scores of all twelve bands and eight indices are given in Appendix 2. Based on these scores, the NDVI, REP, B05 and B11 were selected as the best input features for the DTC and MLC classifiers. The NDVI can separate Sargassum from land (Ls and Lb) and water (Ws and Wd) classes very well, whereas REP and B05 are suitable for discriminating Sargassum on land from mangroves (Vm) and other vegetations (Vo). Additionally, B11 provides a high separability score between floating Sargassum, Sargassum on land and other vegetations.

The distribution of each feature and class is shown in figure 17. It was observed that a few classes have unimodal distributions but do not entirely resemble Gaussian bell curves. Floating Sargassum has a distinct mean value at around 703nm and 0.05 for REP and B11 features, respectively. Persisting overlap exists between mangrove and both Sargassum classes. This is mostly caused by a large variance in the mangrove sample. This characteristic is less pronounced in the REP feature as also suggested by the separability score (Vm-Sf = 1.2 and Vm-Sl = 1.5) in appendix 2. Overlap also exists between Sargassum on land and soil (Ls) on most features except NDVI.

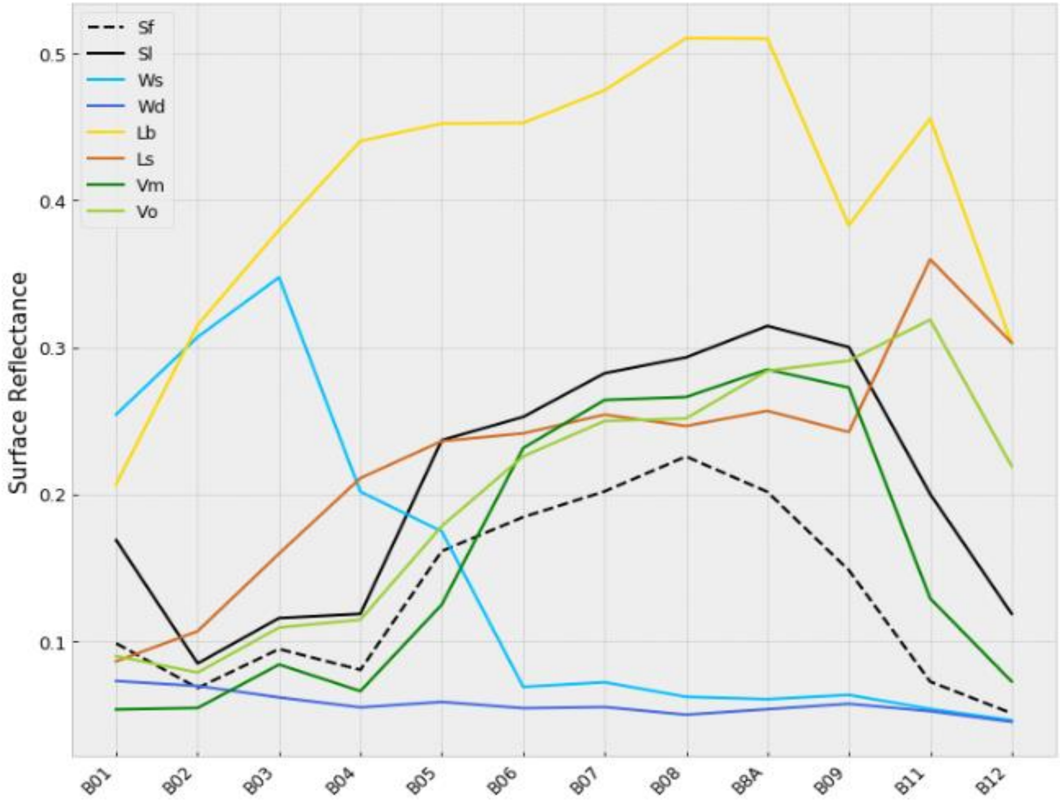

Figure 16. Spectral signature plot of each class sampled from the coast of Bonaire. The mean reflectance value is plotted in this figure.

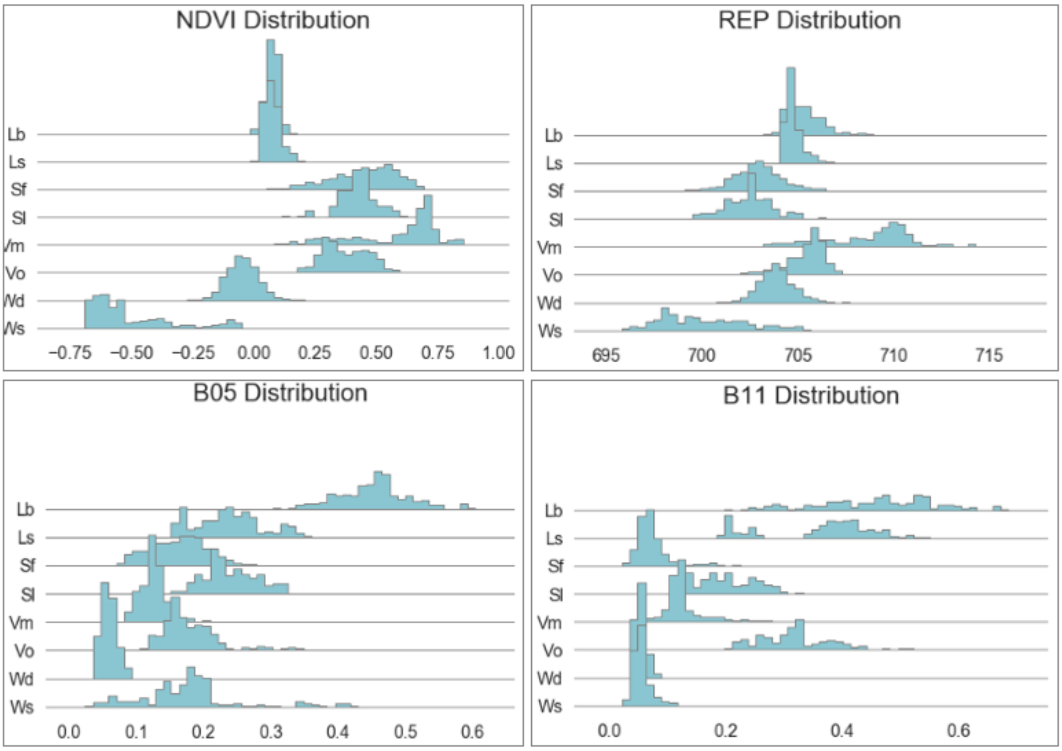

Figure 17. Distribution of each class and input feature. The classes (Sf, Sl, etc.) are displayed on the y-axis, whereas the x-axis illustrates the distribution of the input features NDVI, REP, B05 and B11.

3.1.3 Sargassum classification accuracy

Tuning Decision Tree Classifier for classifying Sargassum
The DTC was tuned using the resampled dataset prior to image classification. The training samples were stratified randomly split into 80% training (=3300 samples) and 20% test (=825 samples) sets. Subsequently, six Decision Tree parameters were investigated and cross validated individually using the default settings in Scikit-learn. The cross-validation results and DTC model are shown in Appendix 3. Attention was given to parameter values that best balance bias and variance. Entropy was selected for split criterion instead of the Gini index due to its lower variance. Subsequently, the rest of the parameters were cross validated with Entropy. The most important splitting features in the Decision Tree model were NDVI and B11.

Model and predictive performances in classifying Sargassum
The model and predictive performances of the DTC and MLC in classifying Sargassum were evaluated. MLC models with probabilities of 10%, 20% and 50% were tested next to the base model (section 2.3.2). A degree of freedom equal to 4 (=number of input features) was used to select the critical value from the Chi-square distribution table for each probability (see section 2.3.2). The model performances were evaluated based on the training and test sets (80:20). Additional floating Sargassum (Sf) samples were collected from a scene taken during another Sargassum invasion on 18 May 2019. This dataset was used as external validation to test the classifiers predictive performances. Appendix 4 summarizes the model and validation accuracy results for classifying Sargassum and other coastal features. Figure 18 shows a comparison between their overall accuracies along with the F1-scores of Sargassum.

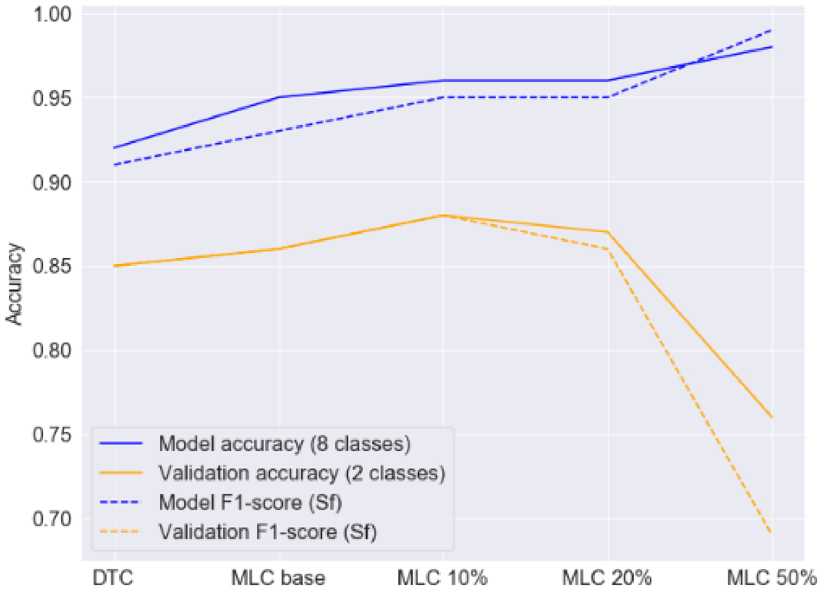

Figure 18. Comparison between model and validation accuracies of the DTC and MLC models in classifying Sargassum and other coastal features. The F1-scores of Sargassum are also plotted in this figure. Note that the model accuracy is based on all 8 classes in the sampling scheme, whereas the validation accuracy from 18 May 2019 is based on Sargassum and Non-Sargassum classes only.

Based on the training and test sets, the DTC achieved an overall model accuracy of 92%. The MLC models yielded higher accuracies between 95% and 98% with increasing probabilities. It should be noted that internally the restricted MLC models introduce a rejection class which was not included in the accuracy assessment. Both the model accuracy and F1-Score of floating Sargassum (Sf) produce comparable results. The DTC yielded an overall validation accuracy of 85%. The $MLC_{10\%}$ produced the highest accuracy of 88% compared to other MLC models. Greater probabilities than 10% did not improve the overall accuracy nor F1-score of floating Sargassum (Sf).

An example classification result is shown in figure 19. The estimated probabilities of both floating Sargassum (Sf) and Sargassum on land (Sl) are also given in this figure. Based on the classification, it was observed that the DTC and MLC$_{20\%}$ shows comparable results in detecting floating Sargassum. Many pixels along the coastline were classified as Sargassum on land, which is less pronounced in the restricted MLC models. Moreover, misclassification of Sargassum on land was noticeable at the fringes of a floating Sargassum raft. The probability map of Sargassum on land (referred to as p (Sl | X)) also suggested slightly higher values at this location. This effect is not visible in the MLC$_{50\%}$ model in this example but was expected to occur to some degree in other situations since both Sargassum classes are ambiguous (see figure 17).

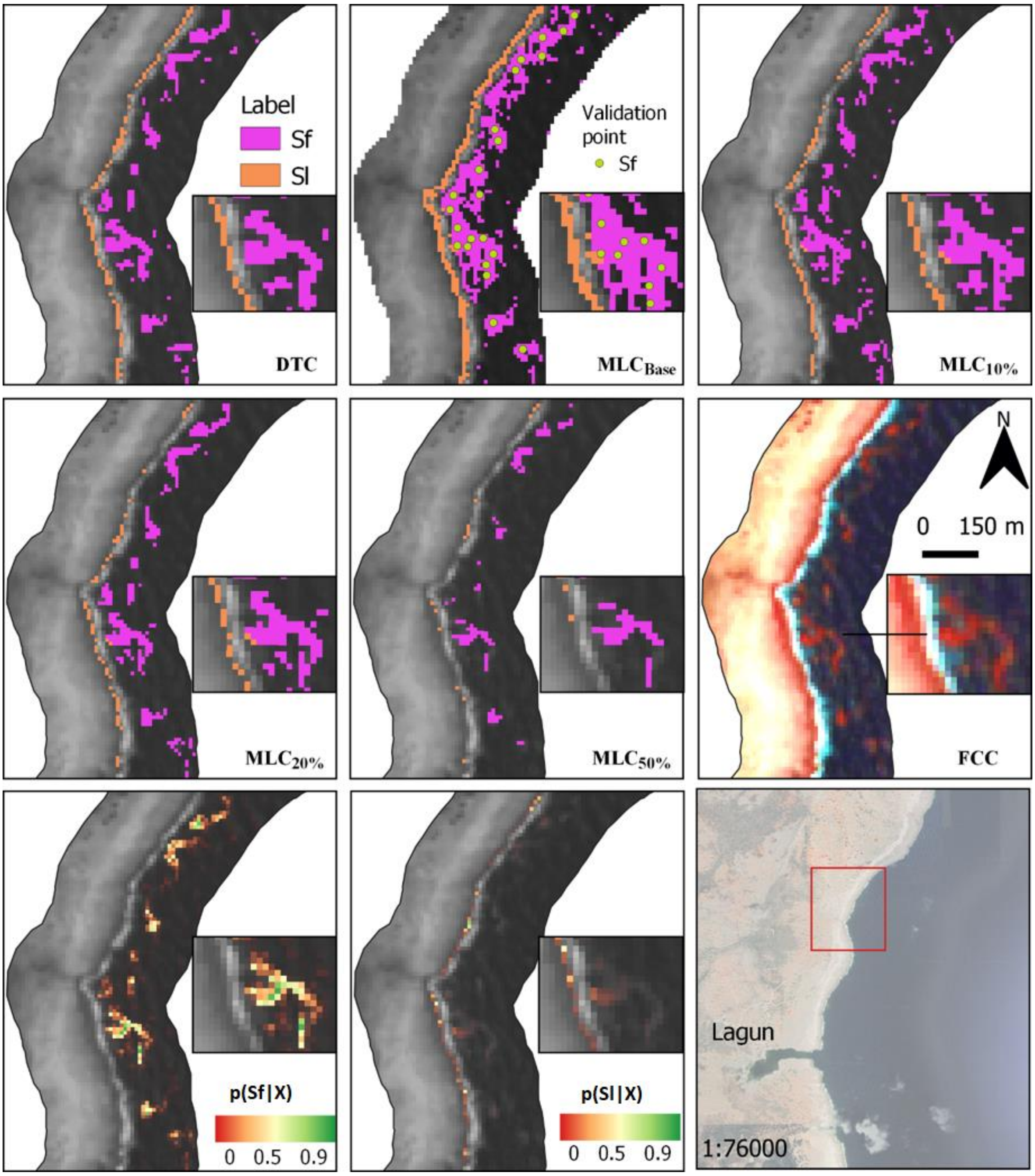

Figure 19. Sargassum classification examples for the validation scene taken on 18 May 2019. An example subset located north of Lagun is shown in this figure. The MLC posterior probabilities p (Label | X) are given on the third row. A closeup of the subset shows noticeable overlap between the two Sargassum classes. Grayscale image and false colour composite (FCC) are based on the same scene.

3.1.4 Robustness of classifiers in classifying Sargassum

Cross-comparison of Sargassum classified areas

A cross-comparison between Sargassum classified Sentinel-2 images was performed to investigate the robustness of the classifiers in detecting Sargassum across different scenes. Scenes taken from two Sargassum influx periods were investigated: 4 to 19 March and 8 to 23 May 2019. Additionally, scenes taken outside the invasion periods were also considered: 28 January, 12 February, 21 August and 29 November 2019. During the study it was observed that persisting misclassification occurs between Sargassum and surface features such as deep waters, dead mangrove stands, (dark) mangrove fringes and clouds. Therefore, a mask was applied on the Sargassum classification results to exclude false positive pixels from a few mangrove areas (see appendix 5). A mask was also applied on the Sargassum on land classification to retain classified pixels around 25m from the coastline. No masks were created for water surfaces and clouds since these phenomena vary per scene.

The DTC and MLC models were used to predict and calculate the total area of Sargassum for each scene. The results are presented in figure 20 for floating Sargassum (Sf) and Sargassum on land (Sl). Two example classifications (without false positive masks) from 8 and 13 May 2019 are shown in figures 21 and 22 for subsets of Lagun and Lac Bay, respectively.

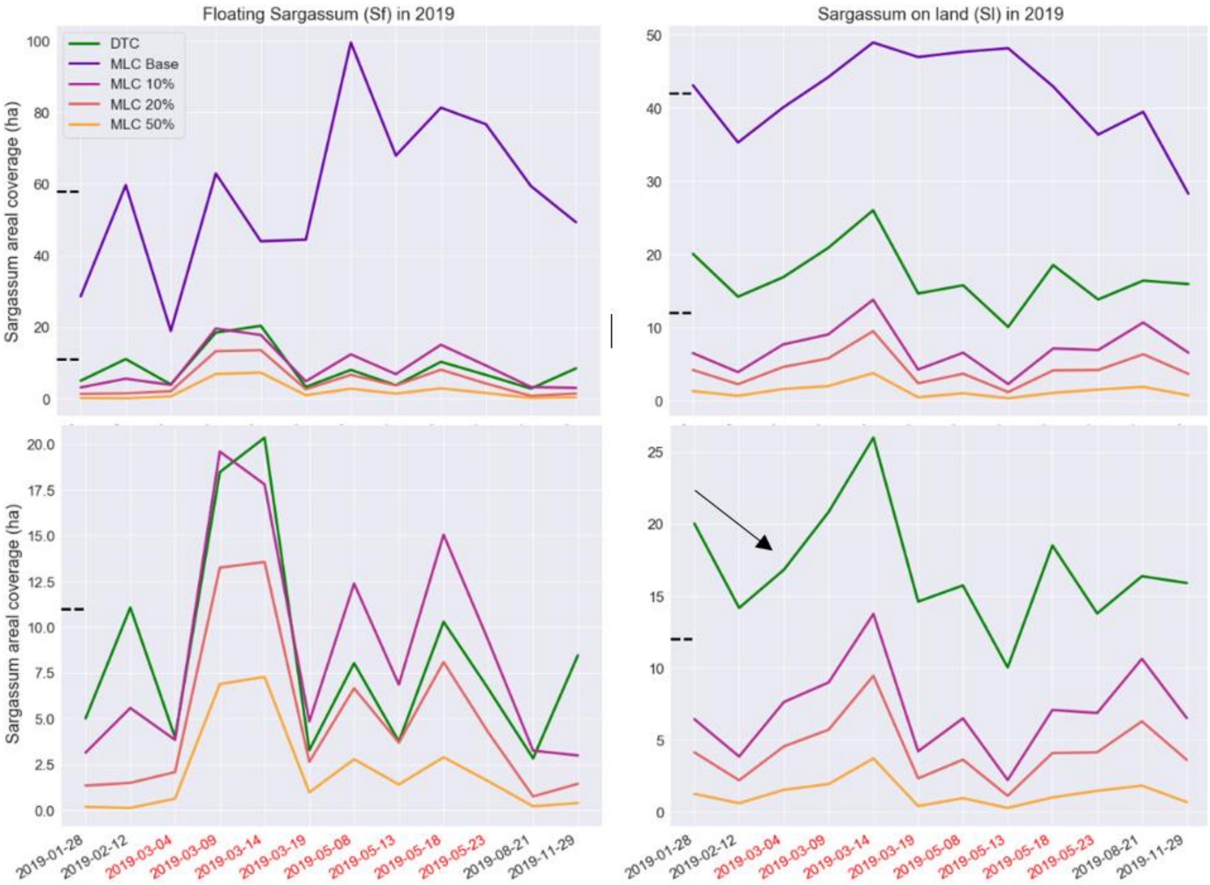

Figure 20. Sargassum (Sf and Sl) total classified area (ha) for various scenes taken during and outside the invasion periods. X-axis labels highlighted in red pertain scenes taken during the invasion. The black horizontal dashed lines on the y-axis indicate the means between the MlC_{Base} *and other models. The bottom row shows the total classified area by all models except* MLC_{Base}*. The black arrow indicates an observed trend in Sargassum on land (Sl) during the March invasion.*

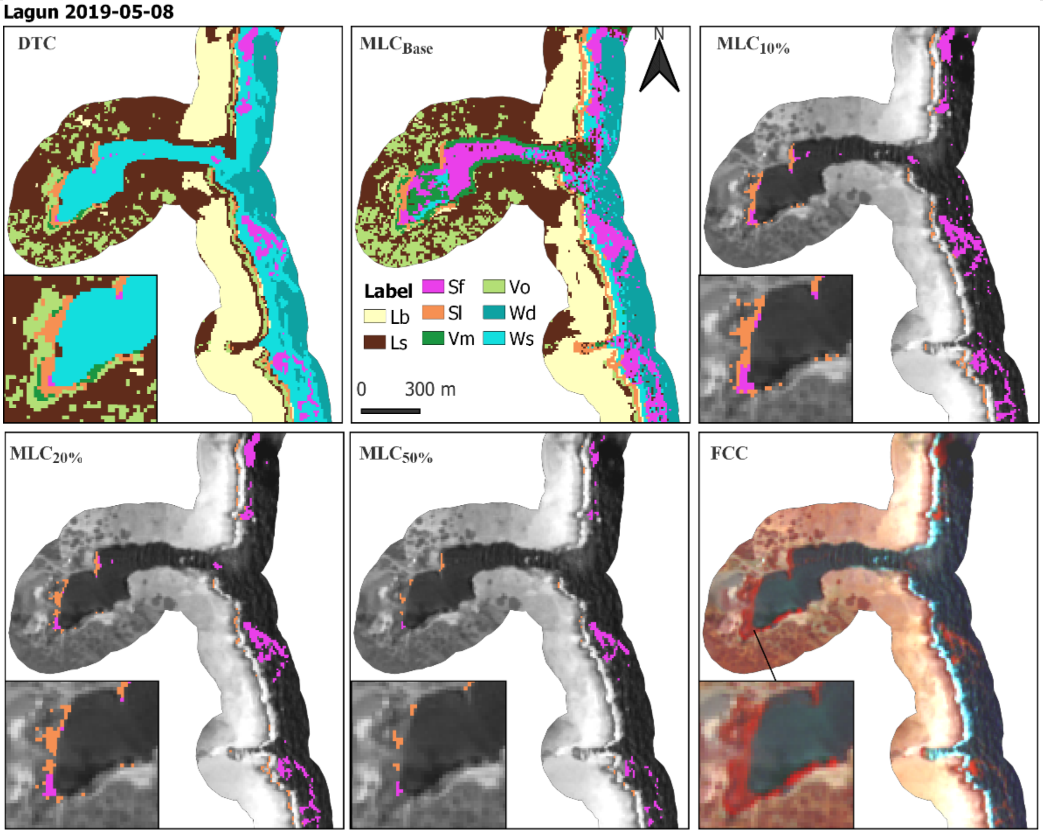

Figure 21. Comparison between DTC and MLC Sargassum classified scenes taken on 8 May 2019 for a subset of Lagun. Grayscale image and false colour composite (FCC) are based on the same scene.

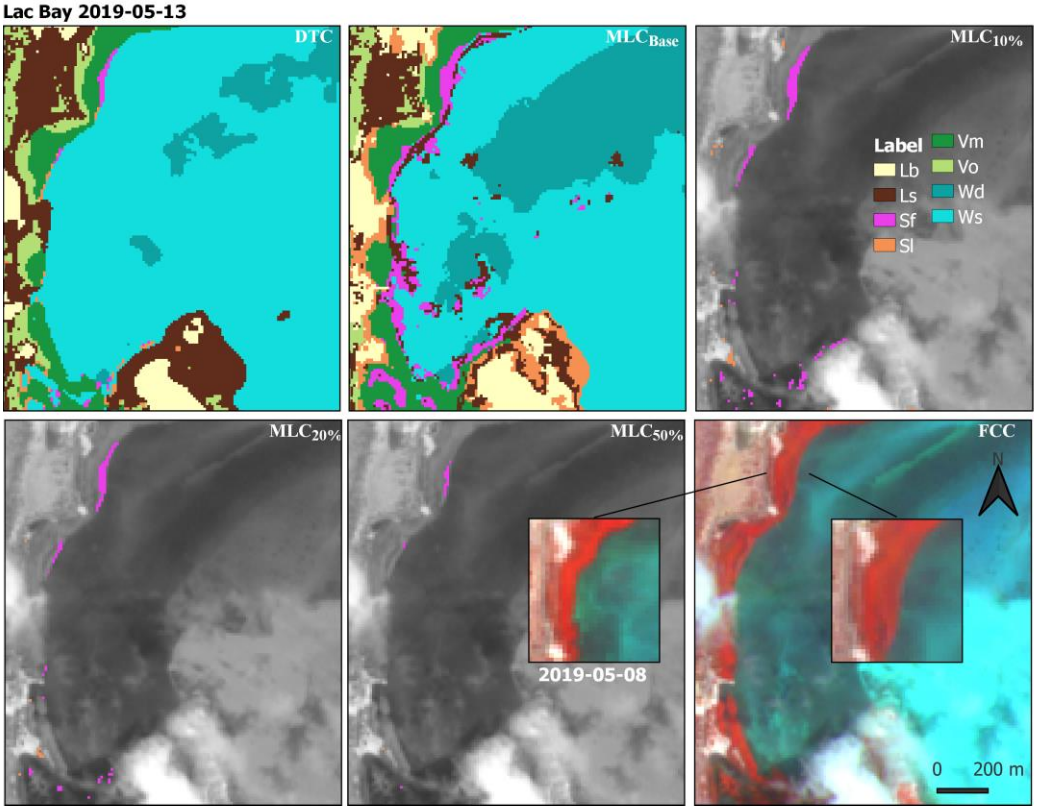

Figure 22. Comparison between DTC and MLC Sargassum classified scenes taken on 13 May 2019 for a subset of Lac Bay. A false colour composite from 8 May 2019 is also shown for a specific Sargassum affected mangrove site. Grayscale image and false colour composite (FCC) are based on the same scene.

Performance in classifying floating Sargassum

Based on the graphs and maps in figures 20, 21 and 22, it was evident that the MLC_{Base} model overestimated the classification of both Sargassum classes. This is mostly caused by aforesaid deep water and cloud (edges) pixels. The DTC and restricted MLC models were able to avoid these false positives more effectively. The average areal difference between the MLC_{Base} and other models was about 47 hectares across all scenes. It is also noticeable that floating Sargassum (Sf), washed up ashore and into mangrove stands (see figure 21), is grossly misclassified as Sargassum on land (Sl). This effect is more pronounced in the DTC model than in other MLC models.

Furthermore, multiple peaks were observed on 9 and 14 March, 8 and 18 May based on the restricted MLC models. Next to these dates, notable peaks were also observed outside the invasion periods on 12 February and 29 November by the DTC model. Upon closer inspection, it was found that these peaks were mostly caused by misclassification of cloud edges as shown in the example in figure 23. The $MLC_{20\%}$ model was found to be more robust in detecting floating Sargassum (Sf) while minimizing false positive errors across different scenes.

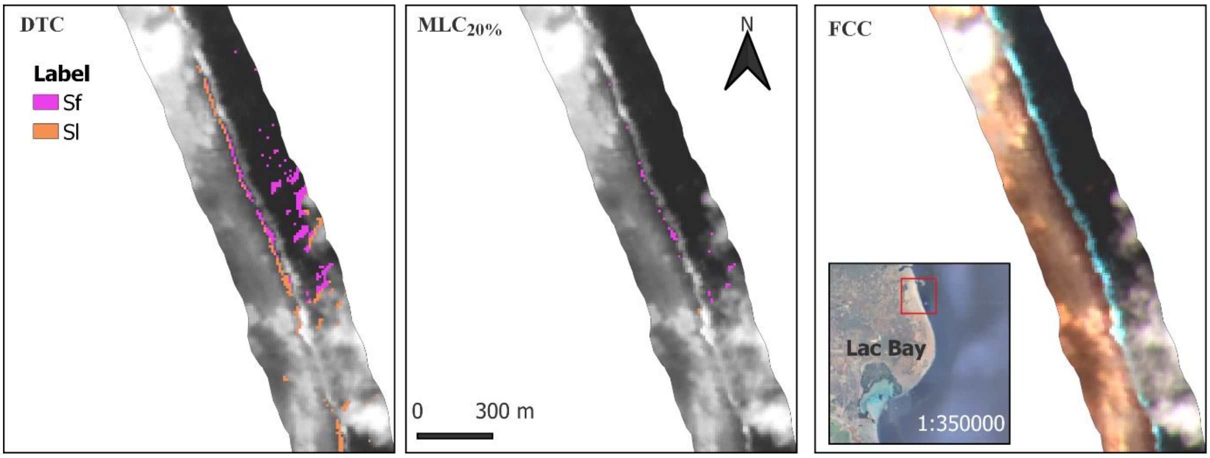

Figure 23. Comparison between DTC and $MLC_{20\%}$ classification results for a scene taken on 12 February 2019. A subset showing misclassification of clouds and deep-water pixels is illustrated in this figure. Grayscale image and false colour composite (FCC) are based on the same scene. Mini map by Google Maps ®.

Performance in predicting Sargassum on land

Sargassum on land (Sl) was found to be more difficult to classify since the classifiers apt to confuse with land (Ls and Lb) and floating Sargassum (Sf) as suggested in figures 21 and 22. Based on figure 20, the DTC model shows noticeable peaks on 14 March and 18 May which were less prominent in the restricted MLC models. As floating Sargassum (Sf) continues to wash up ashore during the first few weeks of the invasion periods, it is very likely that many Sargassum rafts accumulated on land which the classifiers detected as said peaks. This trend is mostly noticeable for the Sargassum invasion in March. However, it should be noted that most models still overestimated Sargassum on land (Sl) outside the invasion periods. The $MLC_{50\%}$ model was found applicable in minimizing these false positive errors. Sargassum on land (Sl) was mostly misclassified along the coastlines (see figures 19 and 21). Most of the northern coastlines of Bonaire are cliffed, hence Sargassum is less likely to accumulate at this site.

Possibility of Sargassum detected outside invasion period

Based on previous Sargassum events in earlier 2019 and 2018, it was observed that massive Sargassum beaching seems to recur around March in Bonaire. According to the Satellite-based Sargassum Watch System (SaWS) outlook bulletin (University of South Florida, n.d.), a large amount of Sargassum was detected with MODIS, among other sensors, in the Caribbean Sea in January and August 2019. The amount of Sargassum was found to be substantially reduced in November. Therefore, the possibility of small patches of Sargassum reaching Bonaire's coastal region outside the invasion period cannot be disregarded. In fact, the classifiers were presumed to have detected small Sargassum rafts (see example in figure 24) along the shorelines on 12 February and 21 August 2019. These rafts were visible floating a few tens of meters away from the northeastern coast near Lagun.

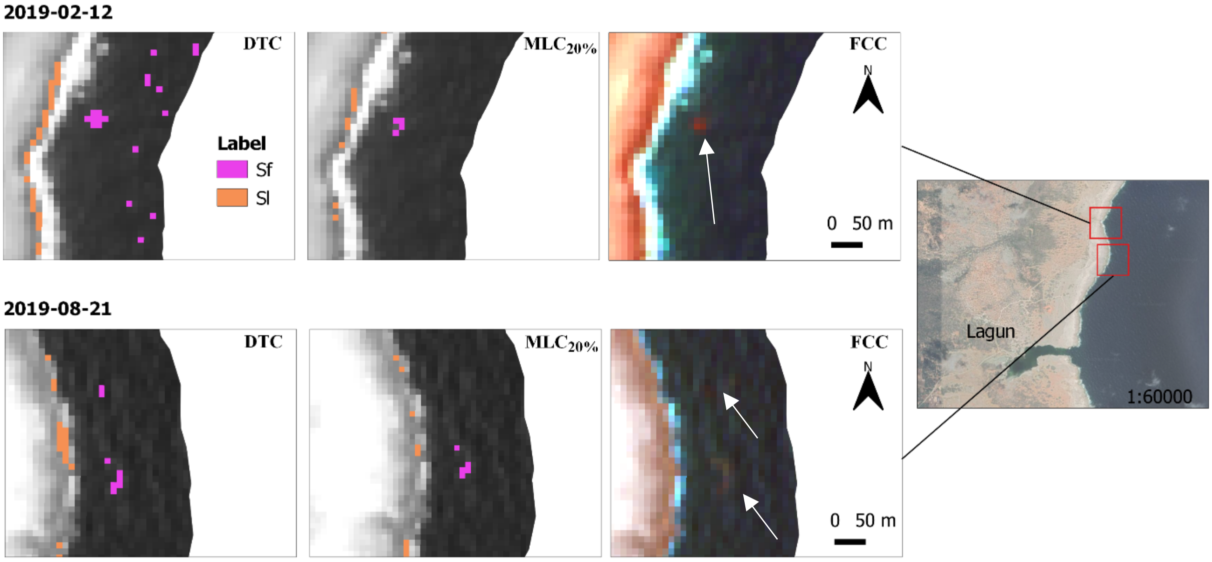

Figure 24. Possible Sargassum strandings in February and November 2019 detected by the DTC and MLC$_{20\%}$ models. The white arrows indicate small Sargassum patches. Grayscale image and false colour composite (FCC) are based on the same scene. Mini map by Google Maps ®.

3.1.5 Sargassum coverage maps

Cumulative Sargassum coverage maps were calculated for scenes taken during the invasions in March 2018 and 2019 (4, 9, 14 and 19 March) and May (8 ,13, 18 and 23 May) 2019. A cumulative coverage map helps to allocate which part of east Bonaire is most impacted by the Sargassum influx. The floating Sargassum coverage maps were computed on a 20m by 20m grid based on the classification results of the MLC$_{20\%}$ model. Despite the uncertainty of the MLC classifier in detecting Sargassum on land (Sl), a coverage map was also calculated for this class using the MLC$_{50\%}$ model. The same false positive masks shown in Appendix 5 were applied on the final coverage maps. The Sargassum coverage maps are shown in figures 25 and 26 for subsets of Lac Bay and Lagun, respectively. False colour composite series of the same subsets are shown in appendix 6.

The Sargassum coverage maps suggest that most Sargassum rafts float towards the southwest mangrove area in Lac Bay. These rafts were also observed to drift towards a few isolated mangrove trees (see appendix 6 and figure 25) located slightly north of this affected mangrove area. The northern mangrove area was found to be classified as floating Sargassum (Sf) as well. Furthermore, it is noteworthy that clusters of Sargassum on land pixels were mostly found next to floating Sargassum.

The total Sargassum coverage area during each scene was calculated and presented in table 8. Note that the results from 2019 were presented before in figure 20 in section 3.1.4. About 18.79 hectares of floating Sargassum (14.37 ha) and Sargassum on land (4.42 ha) were detected in the study area during the first three weeks of March 2018. This amount had doubled to 39.09 hectares in March 2019, whereas about 26.35 hectares Sargassum were detected in May in the same year.

Table 8. Total area (ha) classified as Sargassum (Sf and Sl) for scenes taken during the invasions in 2018 and 2019.

Date	Sf	Sl	Date	Sf	Sl	Date	Sf	Sl
2018-03-04	4.10	2.31	2019-03-04	2.07	1.57	2019-05-08	6.65	0.98
2018-03-09	5.73	1.3	2019-03-09	13.11	1.96	2019-05-13	3.65	0.29
2018-03-14	1.56	0.06	2019-03-14	13.55	3.76	2019-05-18	8.05	1.09
2018-03-19	2.98	0.75	2019-03-19	2.63	0.44	2019-05-23	4.15	1.49
Total	**14.37**	**4.42**	**Total**	**31.36**	**7.73**	**Total**	**22.5**	**3.85**

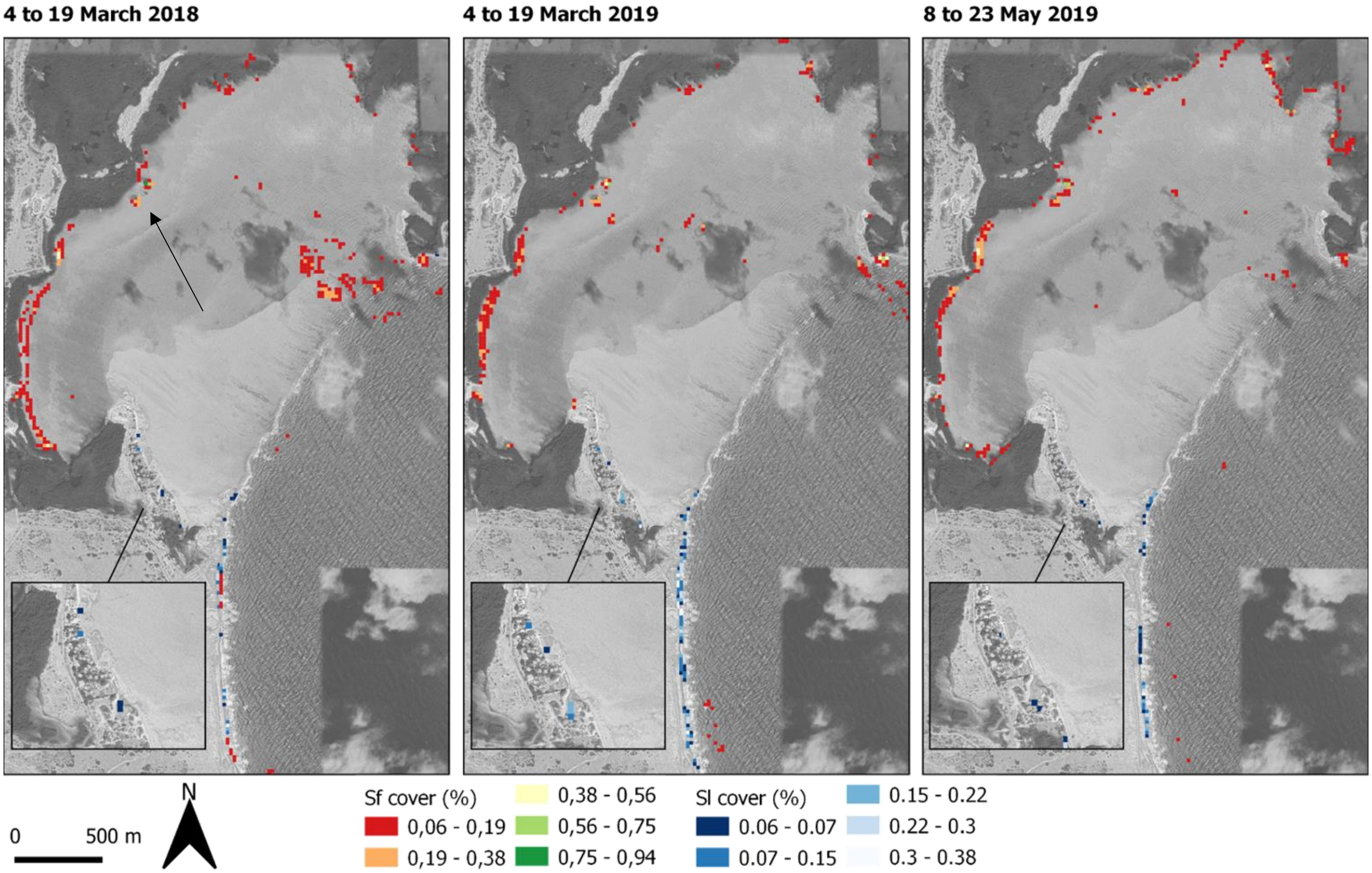

Figure 25. Sargassum coverage maps of Lac Bay during the invasion in March 2018 and March and May 2019. The Sargassum cover was calculated for a 20m x 20m grid. The cover map is displayed on top of a grayscale base map by Google Maps ®. The black arrow indicates the location of individual mangrove tree stands.

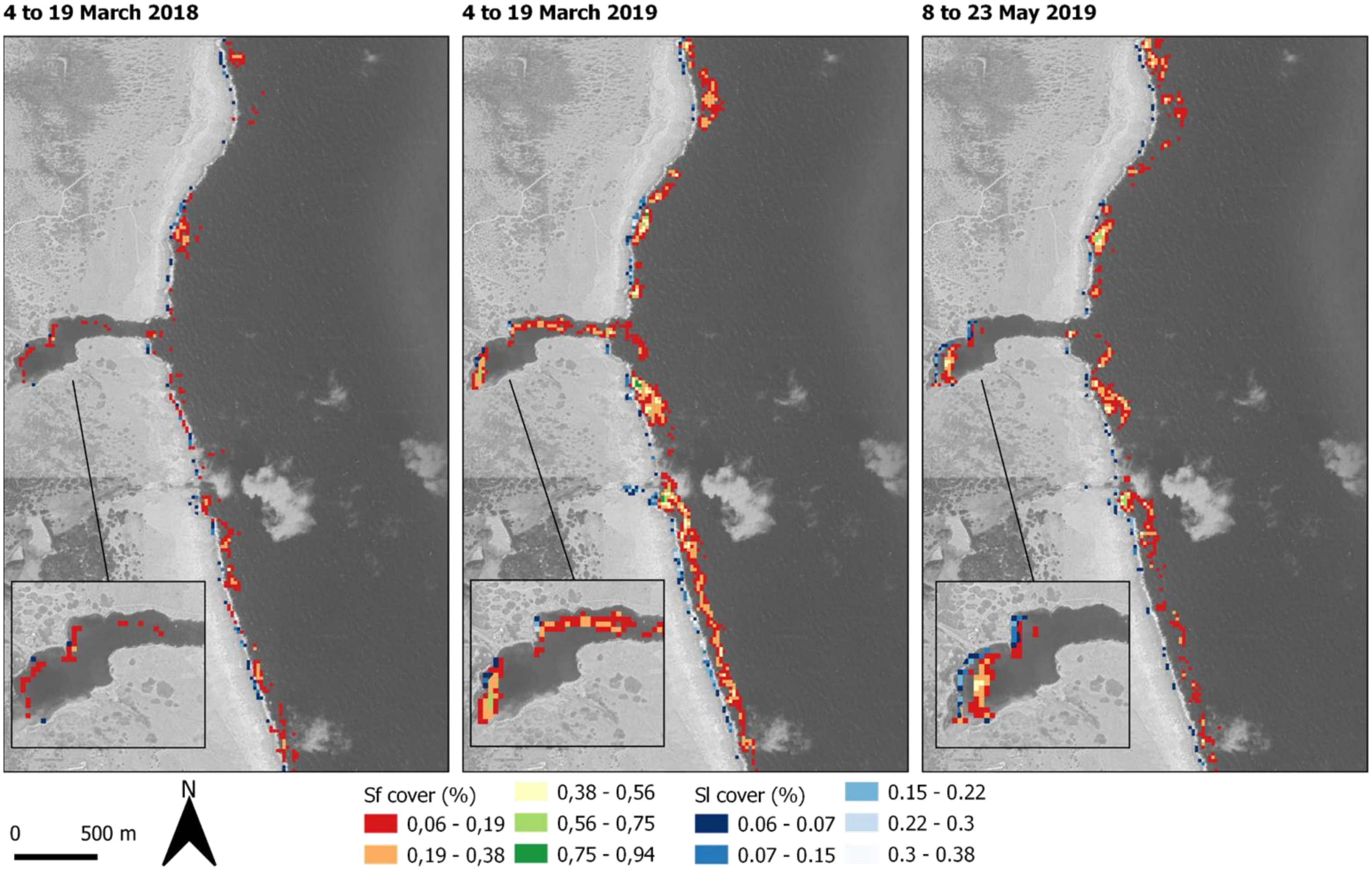

Figure 26. Sargassum coverage maps of Lagun during the invasion in March 2018 and March and May 2019. The Sargassum cover is calculated for a 20m x 20m grid. The cover map is displayed on top of a grayscale base map by Google Maps ®.

3.2 Classification of Sargassum in open sea

3.2.1 Segmentation of spectral index images by density slicing

Floating Sargassum (Sf) on open sea was classified through density slicing of Green Normalized Difference Index (GNDVI) image data. Seven subsets from scenes taken on 4 March 2018, 4 and 9 March, 28 April 2019 were investigated (figure 10). GNDVI images were derived from each subset and the most suitable threshold value to segment the image was defined based on image interpretation. The threshold value indicates the minimum GNDVI value to separate Sargassum patches from the background (i.e. water surface, clouds and other noise). Attention was given to the sea state and cloud condition in each scene, which affect the visibility of Sargassum slicks on the water surface.

The GNDVI distribution of each subset is presented in figure 27 along with the position of the selected threshold. Two groups of GNDVI values were identified based on the sea state. A GNDVI value between -0.25 and -0.30 was found suitable for detecting Sargassum patches in calm dark waters. The presence of sun-glint, whitecaps and clouds shift the recognition of these patches towards positive values. A GNDVI threshold value around 0.05 was found to be more applicable in such noisy scenes. Floating Sargassum pixels have a low frequency in the image compared to water pixels, hence they are often found in the tail of the histogram.

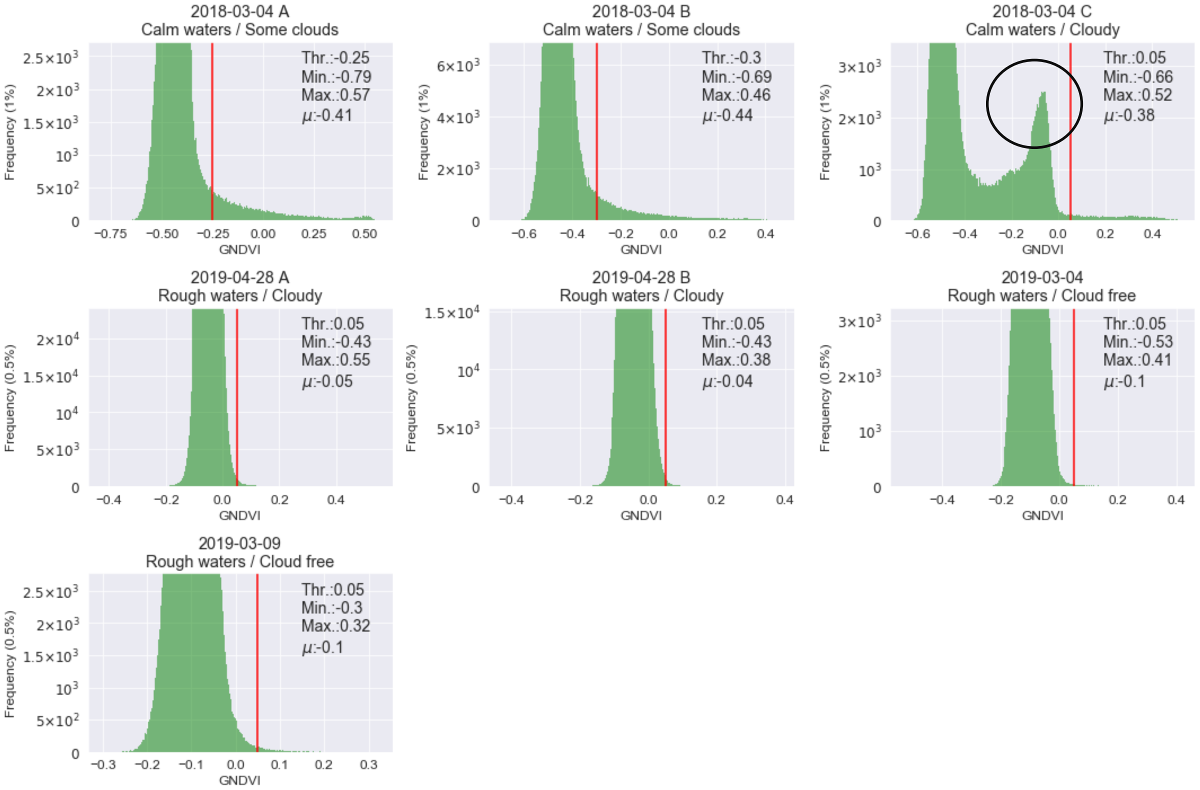

Figure 27. GNDVI distribution of each subset including the defined position of the threshold in red. The black circle indicates the presence of cloud in a GNDVI image. The y-axes are limited to 1% and 0.5% of the data for scenes with calm- and rippled waters, respectively.

3.2.2 Segmentation of principal component images by Triangle algorithm

Selected principal component images

Principal Component Analysis was performed for seven different subsets located on open sea. Each PC image was visually inspected, and the best PC image that provides high contrast between floating Sargassum and the background was selected. The selected PC images are shown in figure 28. During image inspection, it was observed that PCs 1 and 2 reveal the most Sargassum patches in dark calm waters with some clouds in the scene. The presence of clouds sun-glint, and whitecaps shift the recognition of Sargassum towards PCs 4 and 5.

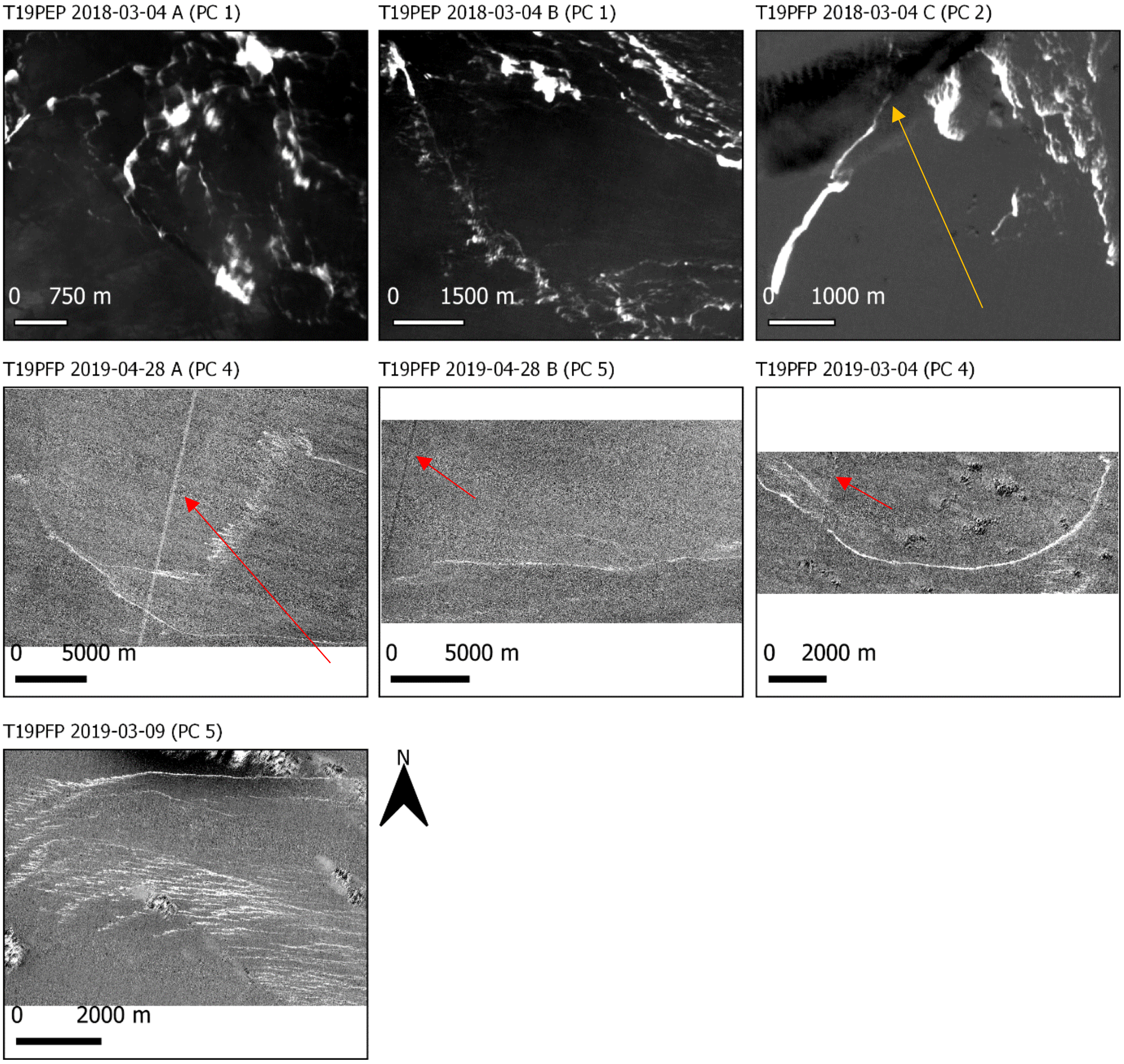

Figure 28. Selected Principal Component images to be used as input for the Triangle algorithm. Contrast stretching was applied on each image to emphasizes floating Sargassum in white. The yellow arrow indicates where Sargassum patches are revealed behind a thin layer of cloud. The red arrow indicates where image striping occurs.

Principal component scores

Table 9 shows the principal component score of each input band across different subsets. An image band with a component score close to -1 or 1 has a significant influence on that component, whereas a score close to 0 shows a weak influence. It is noteworthy that most Red-Edge bands B05 to B8A (705nm to 865nm) have large positive scores (0,18 to 0.47) for PCs 1

and 2 for scenes with dark calm waters. This is most likely associated with strong reflection of floating Sargassum which is indicated as bright pixels in the PC images in figure 28.
In general, the visible bands (4, 3 and 2) and shortwave infrared bands (11 and 12) were found less significant for enhancing floating Sargassum on the water surface.

Sargassum patches obscured by thin layer of clouds (figure 10, section 2.5.2) were observed in subset C for a scene taken on 4 March 2018. These patches were greatly enhanced (bright pixels) in PC image 2. The cloud pixels in this PC image appear dark, which corresponds to large negative component scores in the visible and shortwave infrared bands (PC 2 in table 9).

Furthermore, it was observed that clouds, sun-glint and whitecaps are associated with bright pixels, apart from floating Sargassum, in PC images 4 and 5 for subsets with rough waters. Large positive scores (0.60 to 0.78) were found for near-infrared band B08 (at 842nm) across these subsets, which indicate strong reflection by floating Sargassum. Other Red-Edge bands were found less significant for enhancing floating Sargassum on rough waters, but this varies per subset. It should be noted that the Red-Edge bands, except band B08 (=10m), have a 20m spatial resolution. Consequently, a large portion of the pixels might be dominated by water which attenuates most of the surface reflectance in the Red-Edge spectrum.

Table 9. Principal component score (Eigenvector loading) of each input band across different subsets. Positive scores are highlighted in green, whereas negative scores are in red. Scores close to zero are highlighted in yellow.

Band	PC 1	PC 1	PC 2	PC 4	PC 5	PC 4	PC 5
B02	0,09	0,04	-0,31	-0,54	-0,28	-0,44	-0,51
B03	0,18	0,16	-0,17	0,27	-0,45	0,08	-0,05
B04	0,17	0,14	-0,21	-0,40	0,01	-0,36	-0,30
B05	0,40	0,39	0,18	0,02	0,24	0,20	0,10
B06	0,44	0,44	0,30	0,11	0,10	0,22	0,08
B07	0,46	0,47	0,36	0,13	-0,06	0,21	0,02
B08	0,43	0,45	0,33	0,61	0,76	0,60	0,78
B8A	0,41	0,42	0,28	0,07	-0,20	0,09	-0,08
B11	0,10	0,05	-0,45	-0,19	0,01	-0,21	0,07
B12	0,07	0,04	-0,43	-0,19	-0,17	-0,34	-0,06
Subset	2018-03-04 A	2018-03-04 B	2018-03-04 C	2019-04-28 A	2019-04-28 B	2019-03-04	2019-03-09
Sea state	Calm water	Calm water	Calm water	Rough water	Rough water	Rough water	Rough water
Cloud	Some clouds	Some clouds	Cloudy	Cloudy	Cloudy	Cloud free	Cloud free

Principal component thresholding results
The Triangle algorithm was carried out to automatically calculate the threshold value from the histogram of each PC image. Appendix 7 shows the distribution of each PC image along with the position of the threshold. Values greater than this threshold are associated with floating Sargassum. It is noteworthy that these values are positive as indicated by the bright floating Sargassum pixels in figure 28.

3.2.3 Robustness of different classification methods in classifying Sargassum in open sea

Cross-comparison of floating Sargassum classified areas

The classification performances between the $\text{GNDVI}_{\text{Slice}}$ and $\text{PCA}_{\text{Triangle}}$ were compared with those from the supervised classifiers (DTC and MLC). The MLC_{Base} model was found to be applicable on open sea for both rough and dark calm waters. The total area of each classification was calculated for each subset. The results are presented in figure 29. Figures 30 and 31 show two example results for scenes taken on 4 March 2018 (calm waters) and 4 March 2019 (rough waters).

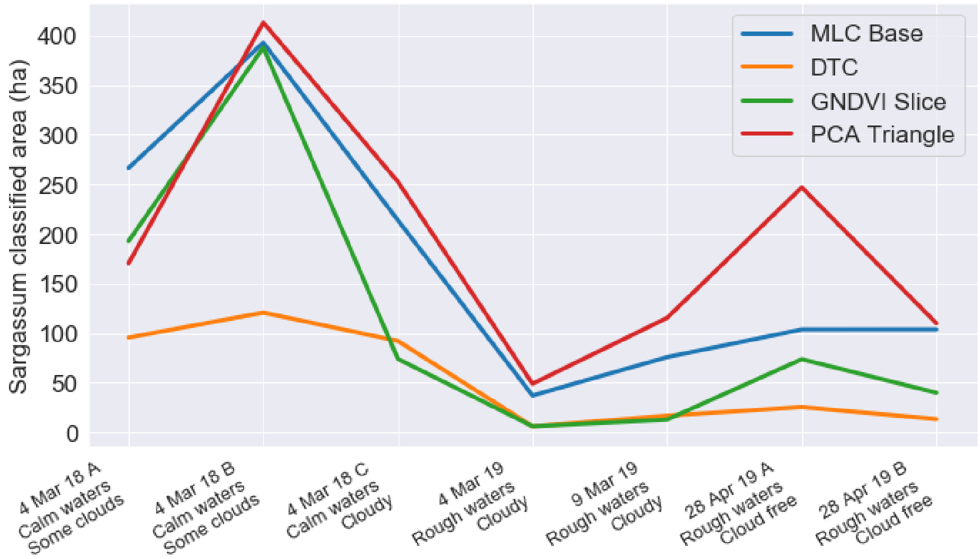

Figure 29. Floating Sargassum classified area (ha) for various scenes taken on east sea of Bonaire. X-axis labels are annotated with the observed sea state and cloud condition in each subset.

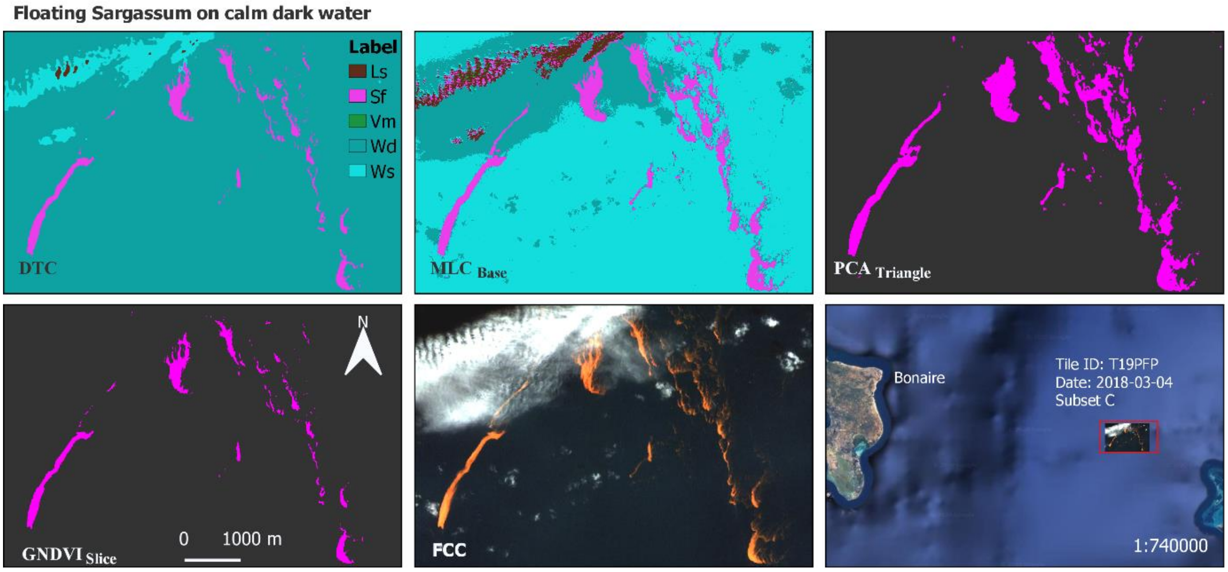

Figure 30. Floating Sargassum (Sf) classification results on calm sea for a scene taken on 4 March 2018 (subset C). Four classification methods were tested: DTC, MLC_{Base}, $\text{PCA}_{\text{Triangle}}$ and $\text{GNDVI}_{\text{Slice}}$. An image enhanced false colour composite (FCC) is shown as reference. The $\text{PCA}_{\text{Triangle}}$ and $\text{GNDVI}_{\text{Slice}}$ results are overlaid on top of a black background for clarity. Base map by Google Maps ®.

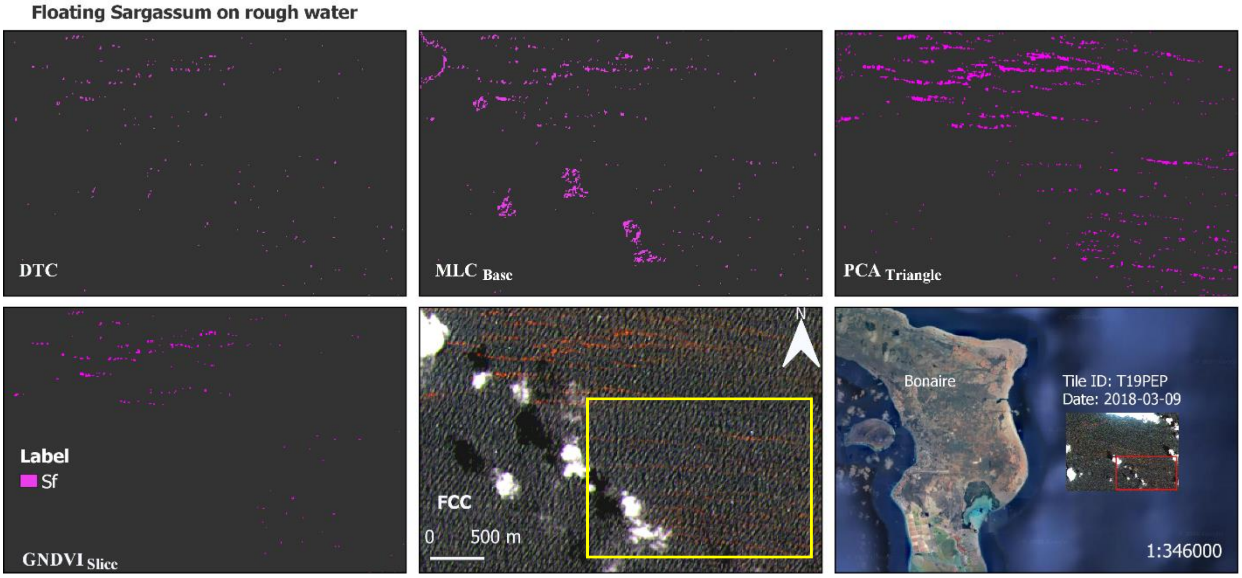

Figure 31. Floating Sargassum (Sf) classification results on rough sea for a scene taken on 9 March 2019. Four classification methods were tested: DTC, MLC_{Base}, $\text{PCA}_{\text{Triangle}}$ and $\text{GNDVI}_{\text{Slice}}$. An image enhanced false colour composite (FCC) is shown as reference. All classification results are overlaid on top of a black background for clarity. The yellow rectangle indicates sparsely distributed Sargassum slicks. Base map by Google Maps ®.

Performance in classifying floating Sargassum on calm waters

Based on figure 30, it was evident that most methods can detect large dense Sargassum rafts on calm waters effectively. The DTC was the least effective out of the four methods. For example, the DTC detected about 102 hectares of floating Sargassum on average for subsets taken on 4 March 2018 (subsets A, B and C). The MLC_{Base}, $\text{GNDVI}_{\text{Slice}}$ and $\text{PCA}_{\text{Triangle}}$ methods show comparable results for these subsets and detected about 210 hectares on average. However, it should be noted that the MLC_{Base} model grossly overestimate cloud and cloud edge pixels as floating Sargassum (Sf) and few other classes (Vm and Ls). Other classification method were also found susceptible to clouds to a certain degree. Besides, sparsely distributed patches are often misclassified as deep water (Wd) pixels by the DTC and MLC_{Base} models. It is also noteworthy that the DTC and MLC_{Base} models do not misclassify floating Sargassum (Sf) as Sargassum on land (Sl) on open sea, which was more apparent on coastal waters (see section 3.1.4).

Performance in classifying floating Sargassum on rough waters

Floating Sargassum on rough waters has the tendency to stretch into long and sparsely distributed slicks. Consequently, Sargassum patches may appear like speckles on the classified image. For example, the slicks at the bottom right corner of figure 31 (yellow rectangle) are almost undetectable. The $\text{PCA}_{\text{Triangle}}$ method was found more effective in revealing such Sargassum slicks compared to other methods. Moreover, persisting misclassification of clouds (edges) by MLC_{Base} model were also noticeable in figure 31.

Robustness of different methods in handling image artefact

Inter-band parallax (see figure 32) was observed on a scene taken on 4 March 2018. It is a type of systematic error caused by overlapping odd and even detectors inside the Multispectral Instrument onboard Sentinel-2. Consequently, each spectral band may observe moving objects (i.e. clouds or airplanes) at a different time which shows as relative displacement of image pixels (Frantz, 2018). The $\text{PCA}_{\text{Triangle}}$ method was found to be the most susceptible to such image artefact.

The odd and even detectors also have slightly different viewing angles which cause spectral response non-uniformity near the detector boundaries (Markuse, 2017). This is mostly apparent as a near vertical striping in the image. As a result, each half of the image records a different intensity of radiance. An example of image striping is shown in figure 33 for a scene taken on 28 April 2019 (rough waters). This image artefact was also noticeable in other PC images in figure 28. Both PCA$_{\text{Triangle}}$ and GNDVI$_{\text{Slice}}$ were prone to misclassify this detector boundary as floating Sargassum (Sf). This explains the peak (247 hectares) detected by the PCA$_{\text{Triangle}}$ method for a scene taken on 28 April 2019 (subset A). Other methods detected less than 100 hectares for the same scene.

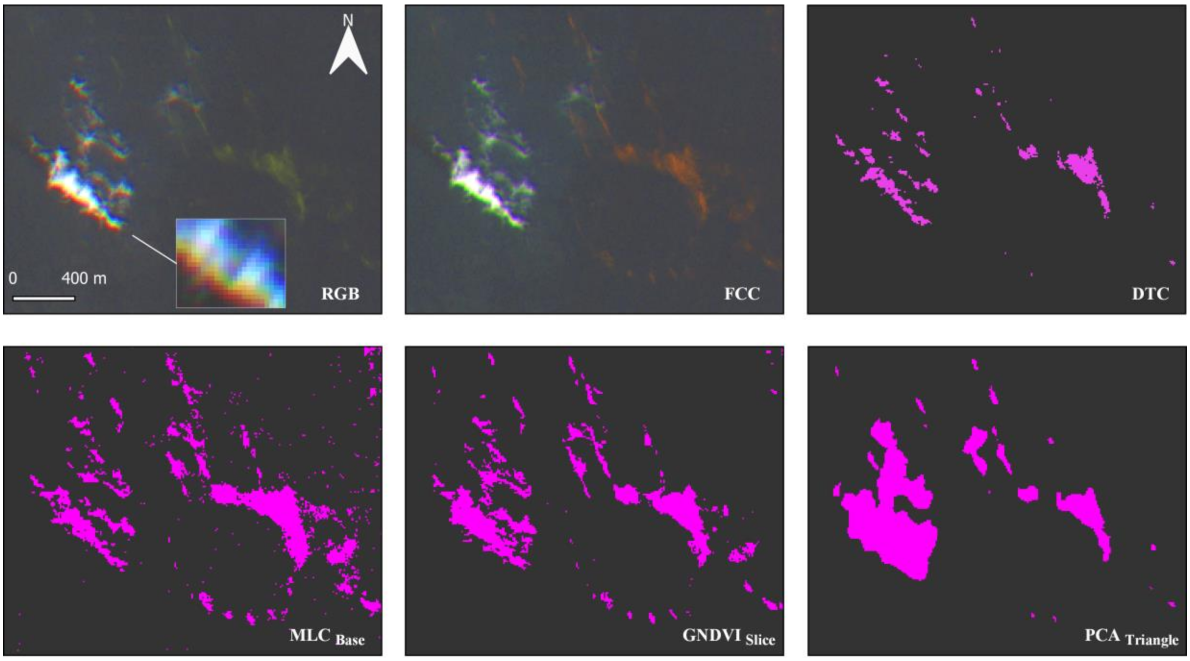

Figure 32. Inter-band parallax artefact found on a subset taken on 4 March 2018 with tile ID T19PEP. The classification results of the four methods: MLC$_{\text{Base}}$, DTC, GNDVI$_{\text{Slice}}$ and PCA$_{\text{Triangle}}$ are depicted in this figure along with the true colour (RGB) and false colour composites (FCC). The typical rainbow colour in the RGB composite reveals the displacement in each band.

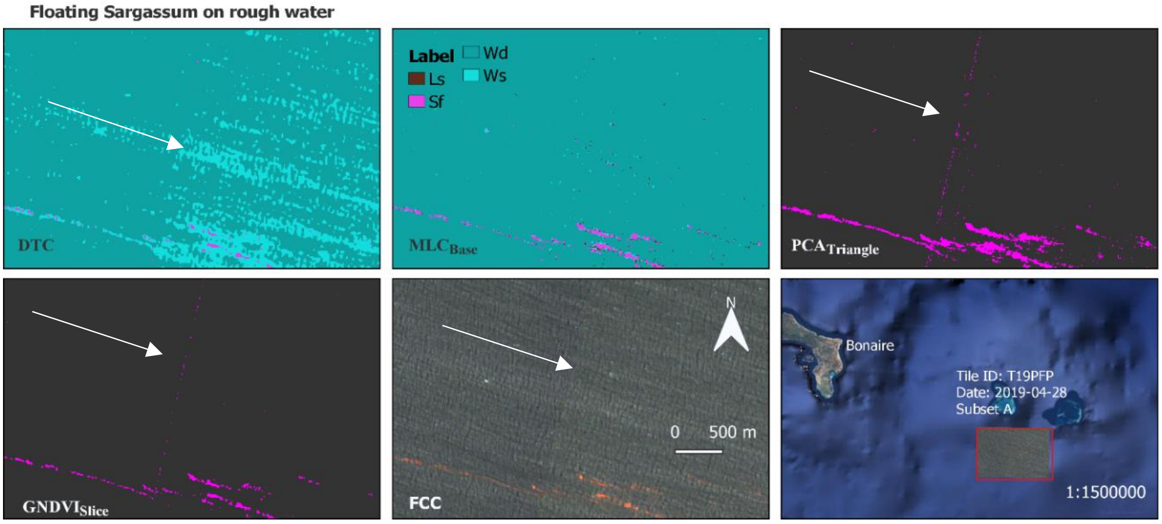

Figure 33. Image striping found on a subset taken on 28 April 2019. Four classification methods were tested: DTC, MLC$_{\text{Base}}$, PCA$_{\text{Triangle}}$ and GNDVI$_{\text{Slice}}$. An image enhanced false colour composite (FCC) is shown as reference. The PCATriangle and GNDVISlice results are overlaid on top of a black background for clarity. The white arrows indicate, though very faintly, where image striping occurs. Base map by Google Maps ®.

3.2.4 Scalability performances

Scene selection for large scale floating Sargassum classification

The scalability of the four previously mentioned classification methods was tested for a larger sea region east of Bonaire. Two previously investigated scenes (calm dark waters) taken on 4 March 2018, which include Sentinel-2 tile IDs T19PEP (tile covers entire Bonaire) and T19PFP (tile covers eastern seas), were classified using $\text{GNDVI}_{\text{Slice}}$, $\text{PCA}_{\text{Triangle}}$, DTC and MLC_{Base} methods.

Threshold selection for Green Normalized Difference Index

The increased spatial extent leads to greater scene disturbances such as clouds and specular reflection. Therefore, a GNDVI threshold of 0.0 was used for both scenes instead of a value between -0.25 and -0.30 that was proposed in section 3.2.2. for dark calm waters.

Selected principal component images for larger subsets

The increased spatial extent also affects the Principal Component Analysis of the ten input Sentinel-2 bands. Initially, PC images 1 (subsets A and B 4 March 2018) and 2 (subset C 4 March 2018) were selected in paragraph 3.2.2 for smaller subsets. However, during visual inspection it was found that PC 3 (tile ID=T19PEP) and 2 (tile ID=T19PFP) show better contrast between floating Sargassum and open water for larger subsets. The principal component scores of the subsets are shown in table 10. Large positive scores (0.29 to 0.39) are found in the Red-Edge bands B06 to B8A (740nm to 865nm), which indicate strong reflection of floating Sargassum and land vegetation.

Cloud mask creation

The classification results of both scenes were merged (first layer priority). Based on the outcome of paragraph 3.2.3, it was found that most methods were susceptible to clouds. Masking these clouds is crucial for effectively calculating the areal coverage of floating Sargassum on open sea. This was not performed in previous paragraphs since the standard Level-2 Sentinel-2 cloud mask data were not satisfactory. The blue band (B02 at 492nm) has a high reflectance for dense cloud pixels and can therefore be used to mask clouds (Coluzzi et al., 2018) by defining a threshold. However, such procedure is a laborious task for multiple scenes since the threshold value may vary per scene. In this part of the study, a cloud mask was created just for the investigated scenes. A surface reflectance greater than 0.09 was found suitable for masking clouds in both scenes taken on 4 March 2018 with tile IDs T19PEP and T19PFP. It should be noted that the created cloud masks do not take cloud edges well into account. Additionally, a sieve filter was applied to reduce leftover isolated pixels in the final merged classifications.

Table 10. Principal component score (Eigenvector loading) of each input band for scenes taken on 4 March 2018 with tile IDs T19PEP and T19PFP. Positive scores are highlighted in green, whereas negative scores are in red. Scores close to zero are highlighted in orange.

Band	PC 3	PC 2
B02	-0.24	-0.35
B03	-0.31	0.17
B04	-0.24	-0.21
B05	-0.07	0.21
B06	0.31	0.32
B07	0.36	0.38
B08	0.29	0.32
B8A	0.39	0.29
B11	-0.38	-0.40
B12	-0.42	-0.42

Table 10 (continued).

Subset	T19PEP 2018-03-04	T19PFP 2018-03-04
Sea state	Calm water	Calm water
Cloud	Cloudy	Cloudy

Total classified floating Sargassum area on greater east sea of Bonaire

The calculated floating Sargassum (Sf) classified area is summarized in table 11 for each method. A pixel-to-pixel similarity map (see figure 35) was also created to assess the degree of overlap across different classification results. The pixel-to-pixel similarity map suggests that most methods can detect large blobs of Sargassum, but not sparsely distributed slicks as previously investigated in section 3.2.3. Based on table 11, the MLC_{Base} and $PCA_{Triangle}$ methods were found effective in classifying Sargassum on calm dark waters, although not all Sargassum slicks on the image could be detected (see blue arrow figure 35). The $PCA_{Triangle}$ model detected the most Sargassum on the open sea with 3911.25 hectares, whereas the $GNDVI_{Slice}$ method detected the least with 805.33 hectares. However, the $PCA_{Triangle}$ method was more susceptible to clouds edges as suggested by the mini map in figure 35. Surprisingly, the MLC_{Base} did not misclassify these cloud pixels as floating Sargassum (Sf) in these scenes, which was the case in previous section 3.2.3 (see figures 30 and 31). The MLC_{Base} model classified about 3078.22 hectares of floating Sargassum. Therefore, for larger subsets, the MLC_{Base} was found to be more robust and effective in detecting Sargassum on calm open sea. An effective overlap of 797.09 hectares was found across all classification results.

Table 11. Combined total classified area as floating Sargassum for two scenes taken on 4 March 2018 with tile IDs T19PEP and T19PFP. Four different classification methods were compared: MLC, DTC, GNDVI density slicing and PCA with triangle algorithm. The sea region of interest is 59 km by 32 km large.

	DTC	**MLC_{Base}**	**$GNDVI_{Slice}$**	**$PCA_{Triangle}$**	**Effective overlap**
Area (ha)	1041.26	3078.22	805.33	3911.25	797.09

Classification comparison with Sargassum Watch System

Floating Sargassum (Sf) was detected by Sargassum Watch System (SaWS) on the same date (4 March 2018) as the scenes used in this part of study. The Sargassum Watch System used the Alternative Floating Algae Index (AFAI) from the MODIS Terra and Aqua sensors to detect floating Sargassum. An AFAI value greater than zero indicates the presence of floating Sargassum. The original FAI was previously investigated in this study (see paragraph 3.1) for coastal waters. However, the results were found not satisfactory, hence it was not investigated in the rest of the study.

Figure 36 shows a comparison between MODIS Terra AFAI[1] and MLC_{Base} floating Sargassum (Sf) map products. The original scenes were taken at 15:05 (MODIS Terra) and 15:07 (Sentinel-2A) Greenwich Mean Time (GMT). An abundance of floating Sargassum (Sf) was observed about 5-10 kilometers away from the east coast of Bonaire in the MODIS Terra AFAI map. The same chunk of floating Sargassum was observed to drift about 1-2 kilometers towards east based on the MLC_{Base} map. A light west wind, which presumably caused this drift, was confirmed based on Bonaire's weather data (see figure 34).

---

[1] Note that both FAI and AFAI are in the same scale. The Sargassum Watch System bulletin page displays AFAI products but the colorbar is labelled as FAI.

Time		Temp	Weather	Wind		Humidity	Barometer	Visibility
14:55	⛅	29 °C	Scattered clouds.	11 km/h	→	62%	1009 mbar	N/A
15:55	⛅	29 °C	Scattered clouds.	9 km/h	→	66%	1009 mbar	N/A

Figure 34. Weather data of Bonaire for 4 March 2018. Image adapted from Time and Date webpage (https://www.timeanddate.com/weather/@7609816/historic?month=3&year=2018).

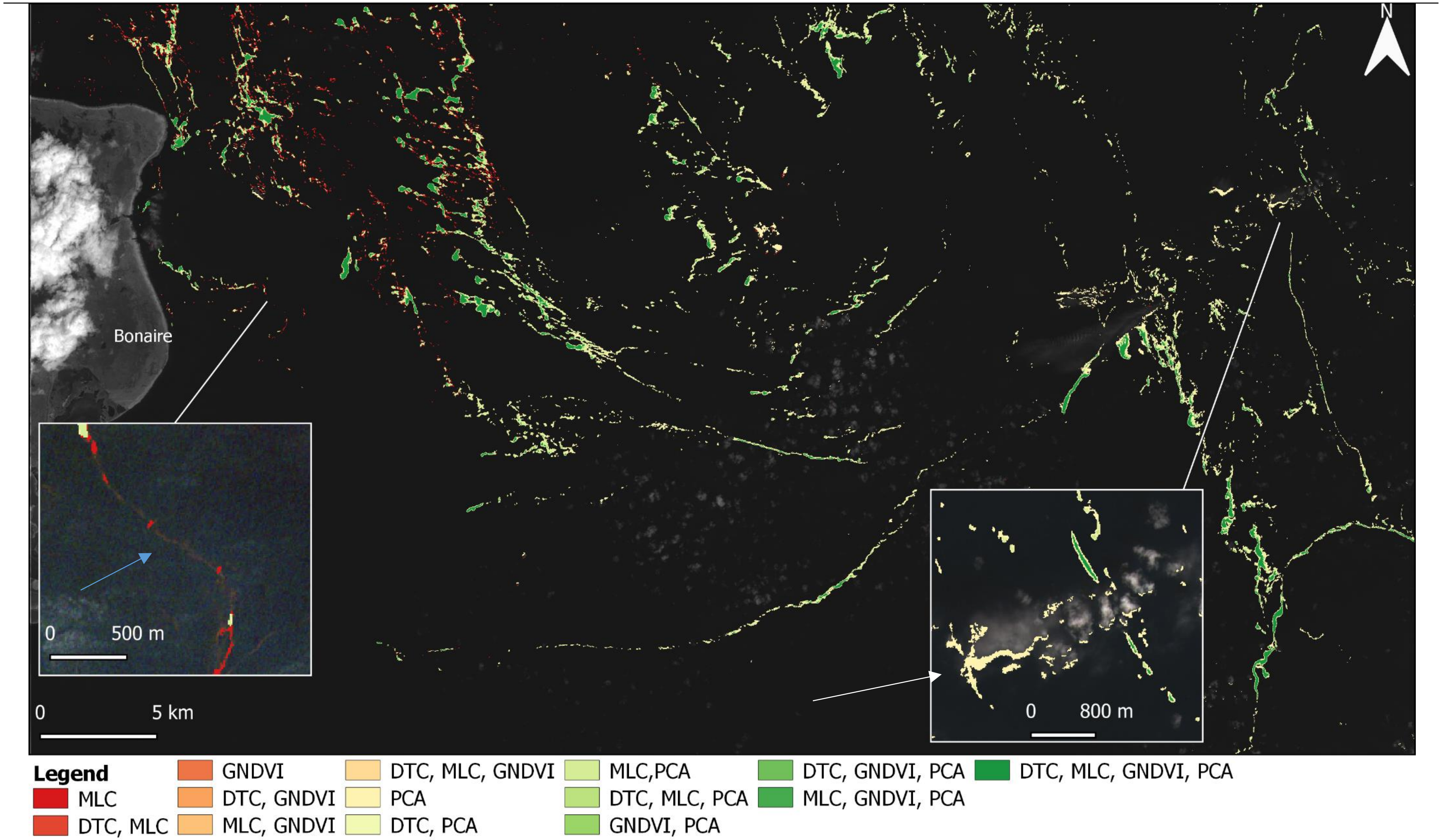

Figure 35. Pixel-to-pixel similarity map showing the overlap between the $\text{GNDVI}_{\text{Slice}}$*,* $\text{PCA}_{\text{Triangle}}$*, DTC and MLC floating Sargassum (Sf) classifications. The pixel-to-pixel similarity layer is overlaid on top of a merged grayscale image of the two classified scenes taken on 4 March 2018 with tile IDs T19PEP and T19PFP. The white dashed lines indicate up to where the two tiles overlap. Two mini maps are shown in false colour for reference. The white arrow indicates where misclassification of floating Sargassum (Sf) occur. The blue arrow indicates where a Sargassum slick is not classified.*

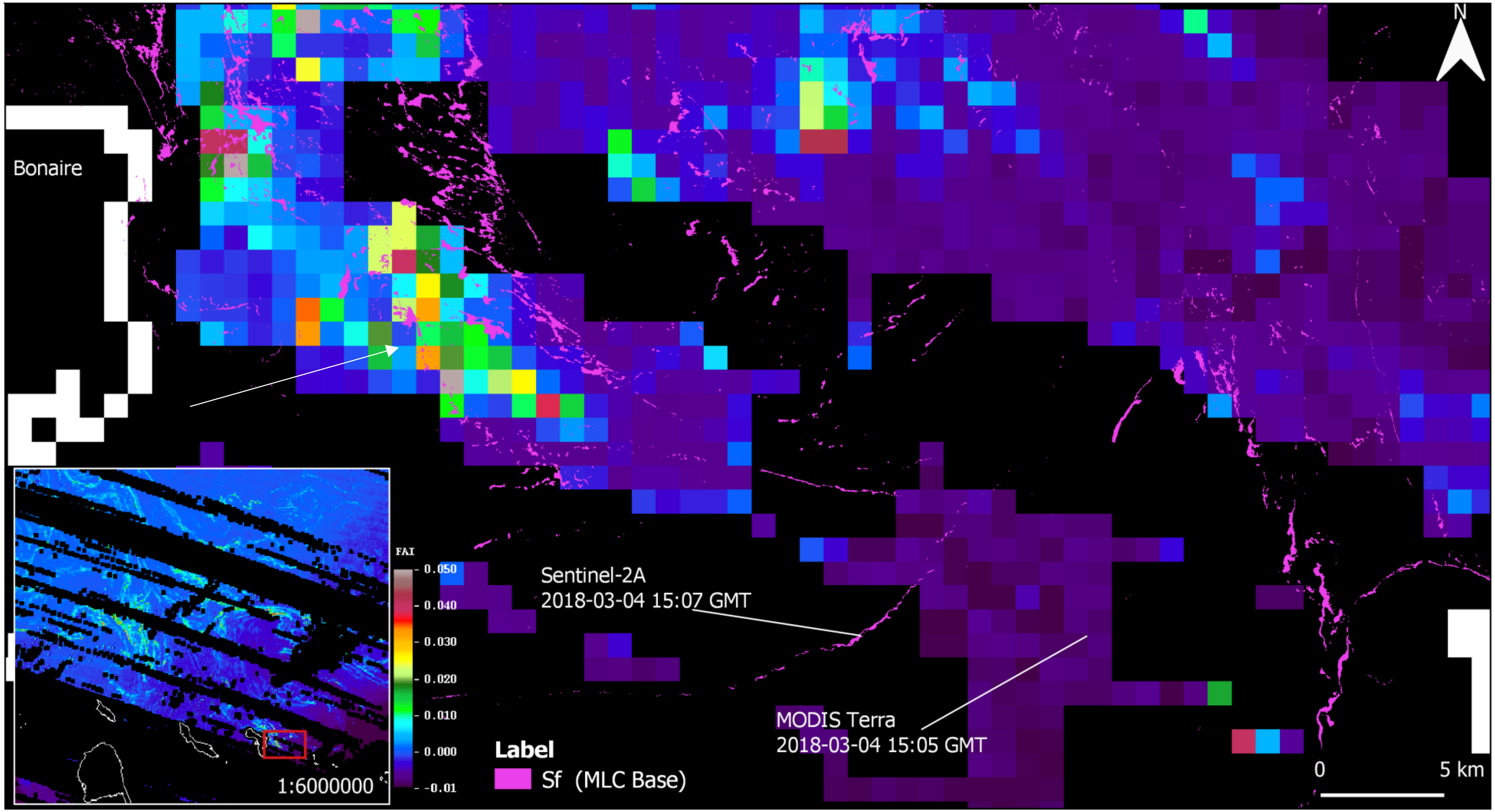

Figure 36. Comparison between MODIS Terra Alternative Floating Algae Index (AFAI) and MLC$_{Base}$ floating Sargassum (Sf) map products. Both scenes were taken on 4 March 2018 at 15:05 (Sentinel-2A) and 15:07 (MODIS Terra) GMT. The mini map shows the Sargassum influx in greater east Caribbean Sea. The black pixels refer to no data areas in which presumably clouds, and land were masked from the MODIS Terra AFAI product. The white arrow indicates an observed abundance of floating Sargassum. MODIS Terra AFAI image courtesy of the Sargassum Watch System of University of South Florida Optical Oceanography Lab (https://optics.marine.usf.edu/projects/saws.html).

3.3 Classification of seagrass in Lac Bay

3.3.1 Sampled dataset for seagrass classification

Purposive sampling was carried out to build a training dataset for the supervised Decision Tree and Maximum Likelihood classifiers. Pixel values from multiple training sites covering seagrass and non-seagrass bottom types were obtained in Lac Bay. The pixel values of bands 2,3 and 4 were sampled from three Sentinel-2 scenes taken on 8 and 28 January and 12 February 2019. Appendix 8 shows an overview of the sampled dataset. The band covariance matrix of each bottom type is also given in this appendix. The total number of samples in the dataset is 819 in which seagrass and non-seagrass have about equal sample sizes.

The distribution of each class and input feature is shown in figure 37. Severe overlap exists between seagrass and non-seagrass classes across the visible spectrum. A bimodal distribution was observed in B02 (490nm) and B03 (560nm) for non-seagrass bottom type. This was presumably caused by dark coral reefs (low value) and shallow water pixels (high value). This phenomenon is most pronounced in B04 (665nm). The Jeffries-Matusita separability score suggests that B02 (score =0.559) is the most effective for separating both classes compared to B03 (score = 0.398) and B04 (score = 0.161). All bands were used as input features for the classifiers.

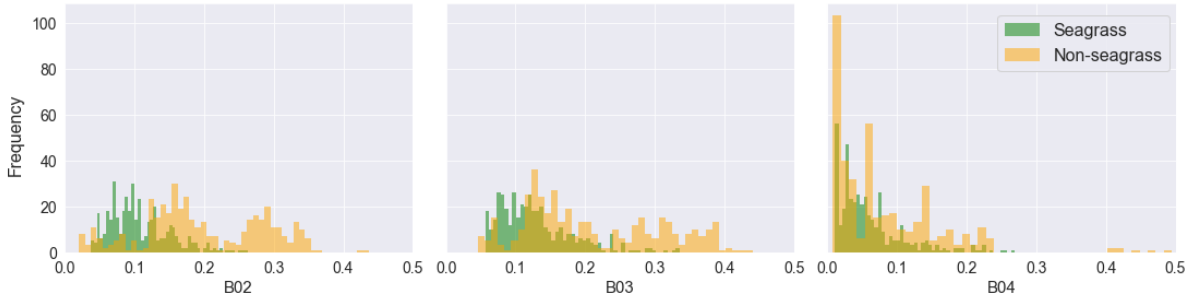

Figure 37. Distributions of seagrass and non-seagrass classes for each input feature. The x-axis is limited to 0.5 for better comparison.

3.3.2 Seagrass classification accuracy

Tuning Decision Tree Classifier for classifying seagrass
The DTC and MLC model performances were evaluated prior image classification. The training samples were stratified randomly split into 80% training (=963 samples) and 20% test (=241 samples) sets. A cross-validation was performed to tune the DTC hyperparameters. The cross-validation results and DTC model are shown in appendix 9. The most important splitting feature in the Decision Tree model was B02 based on the Entropy criterion.

Uncertainty of Maximum Likelihood Classification results
Class posterior probability and Entropy maps were created to assess the degree of uncertainty of the MLC model. These maps are shown in appendix 10 for scenes taken on 8 January, 4 March, 8 August and 29 November 2019. Note that scenes from August and November were not used to train the classifier. The probability maps suggest that the likelihood of a pixel belonging to a certain bottom type varies per scene. High seagrass probabilities were observed in between shallow and deep waters in Lac Bay. Such patterns were found for non- seagrass as well. This indicated that many pixels were assigned equal probabilities for both bottom types. Equal probabilities imply high uncertainty as suggested by the Entropy maps. Contrarily, the MLC was able to predict bare-sand sites (i.e. shallowest waters) with high certainty (Entropy = 0).

Model and predictive performances in classifying seagrass

The model and predictive performances of the DTC and MLC classifiers were evaluated. MLC models with probabilities of 10%, 20% and 50% were tested next to the base model. A degree of freedom equal to 3 (= number of input features) was used to select the critical chi-square value of each probability. The model performances were evaluated based on the training and test sets. The 2019 seagrass observation dataset was used as external validation to test the classifiers predictive performances. The classification results for a scene taken on 4 March 2019 was validated. Appendix 11 summarizes the model and validation accuracy results for classifying seagrass. Figure 38 shows a comparison between their overall accuracies along with the F1-scores of the seagrass class. Figure 39 displays the classification validation results.

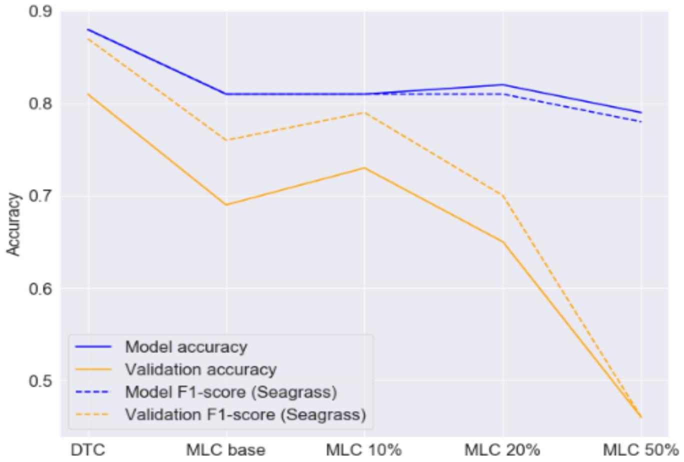

Figure 38. Comparison between model and validation accuracies of the DTC and MLC models in classifying Seagrass and non-Seagrass. The F1-scores of seagrasses are also plotted in this figure.

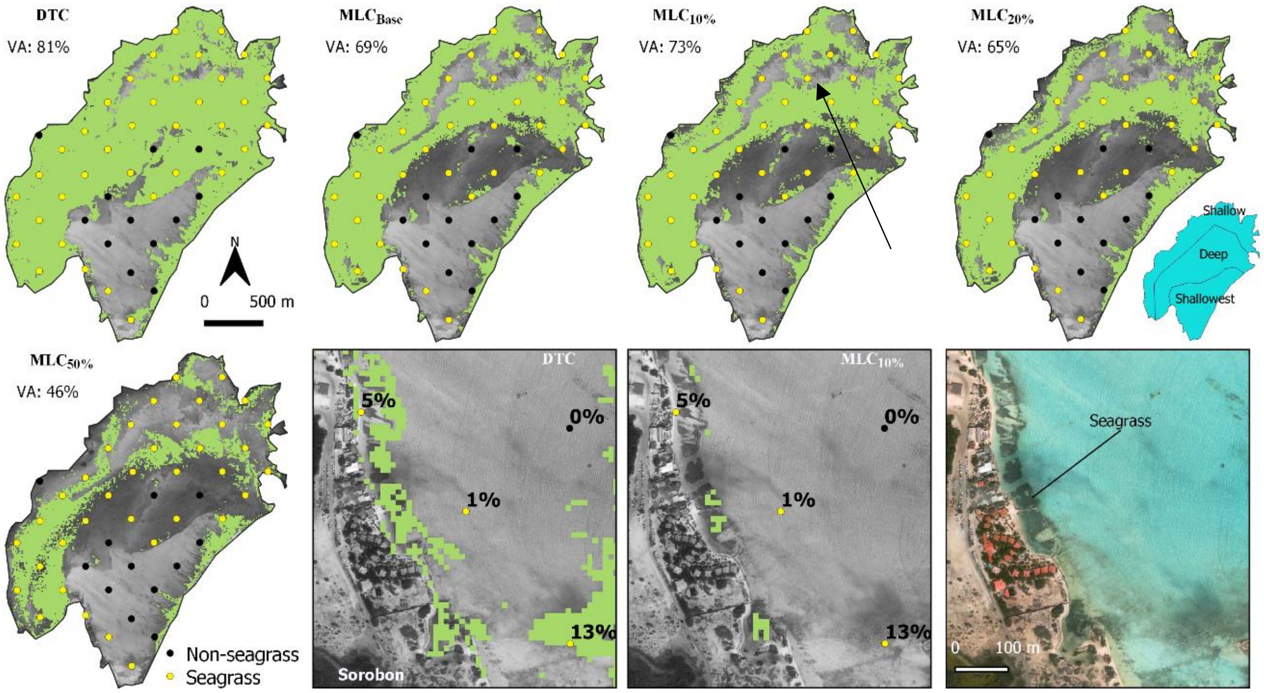

Figure 39. Seagrass classification validation results for a scene taken on 4 March 2019. A subset of Sorobon is shown in the second row. The seagrass observations of 2019 are annotated with the mean cover (%) of the four species found at each site. The black arrows indicate a site with mixed bottom types. Grayscale and true colour base maps by Bing Maps ® 2019.VA = validation accuracy

Based on the training and test sets, the DTC achieved an overall model accuracy of 88%, whereas the MLC achieved accuracies between 79 and 81% for increasing probabilities between 0% (base model) and 50%, respectively. The DTC yields an overall validation accuracy of 81%, whereas the MLC achieved significantly lower accuracies between 46% and 73% for the same confidence interval. The $\text{MLC}_{10\%}$ model was found to performs best, with the lowest variance, compared to other MLC models. Also, the F1-score of seagrass in the validation step was found to be the highest (F1-score = 79%) for the $\text{MLC}_{10\%}$ model.

The classification results in figure 39 suggest that both classifiers can predict seagrass situated in-between shallow and deep waters. Dissimilarities between classifiers were found more severe on sites with mixed bottom types and on shallowest waters (e.g. Sorobon). These mixed bottom types were better discriminated by the MLC models.

3.3.3 Robustness of classifiers in classifying seagrass

Cross-comparison of seagrass classified area in Lac Bay

Four different Sentinel-2 scenes taken on 8 January, 4 March, 21 August and 11 November 2019 were classified for seagrass and non-seagrass bottom types. Note that scenes from January and March were used to train and validate the classifiers. The DTC and restricted MLC models were used to predict the scenes. Figure 40 summarizes the total seagrass classified area for three different depths in Lac Bay. The classification results are shown in figure 41. In this figure, the MLC classifications were aggregated into a pixel-to-pixel similarity map. The same was done for DTC and $\text{MLC}_{10\%}$ classifications. This MLC model was selected for its low variance (see paragraph 3.3.2).

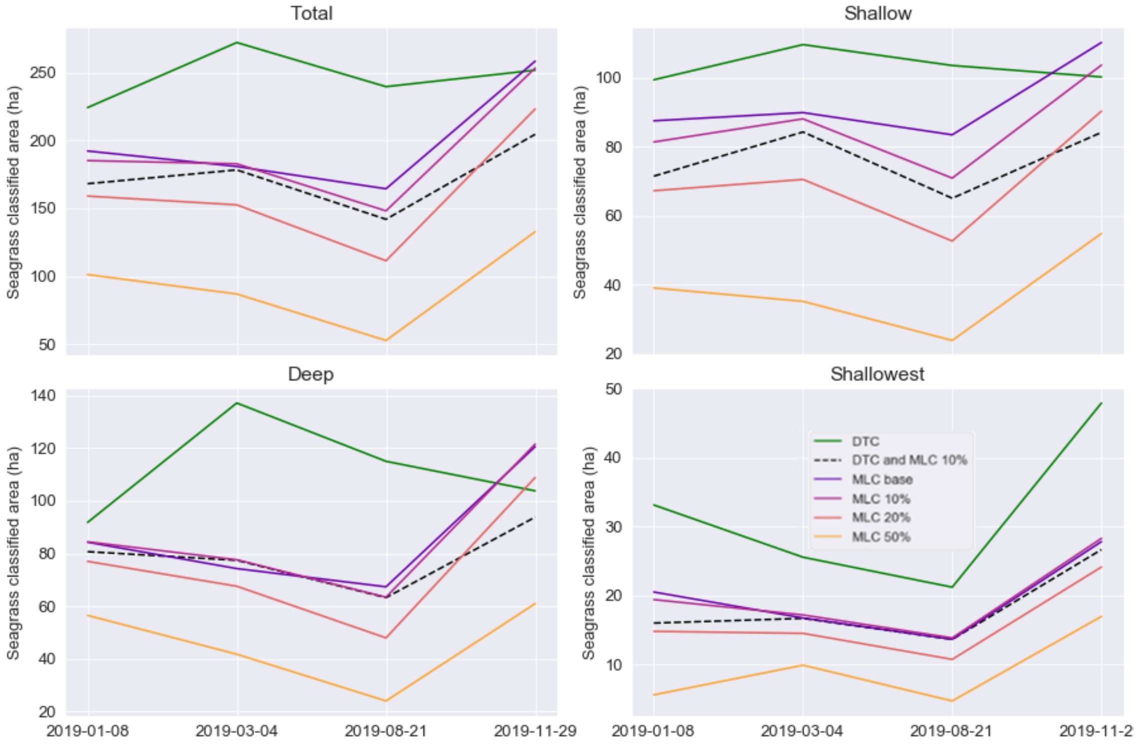

Figure 40. Cross-comparison between DTC and restricted MLC models classified seagrass area (ha) for three different depths in Lac Bay.

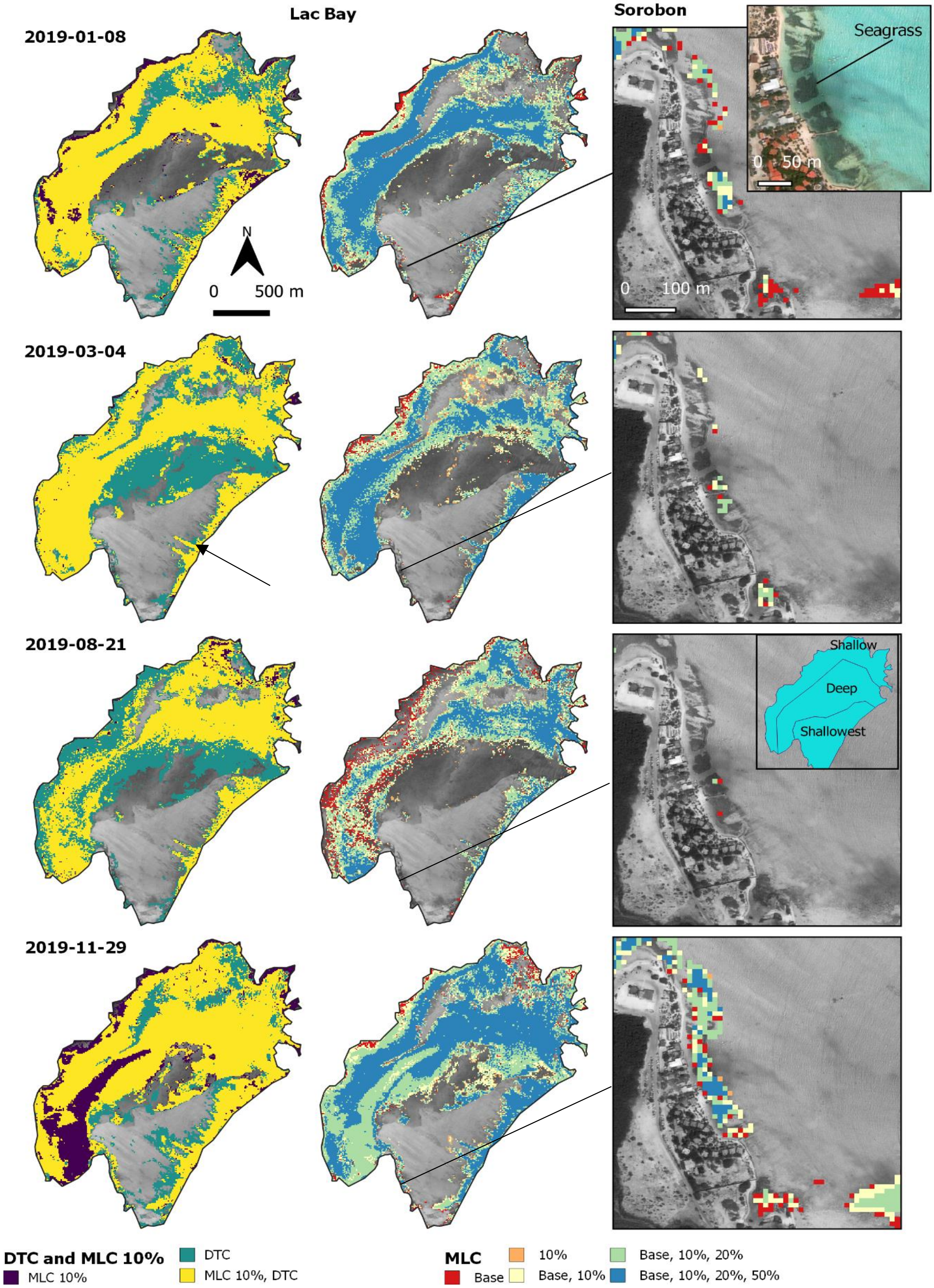

Figure 41. Cross-comparison between DTC and restricted MLC models classified seagrass distributions across multiple scenes. The first column shows the similarities between DTC and MLC10% models, whereas the second and third columns depict the similarities between various MLC models. The black arrow indicates the location of fringing coral reefs. Grayscale and true colour base maps by Bing Maps ® 2019.

Based on figures 40 and 41, it was evident that the DTC model predicted the most seagrass bottom type compared to the MLC models. The predicted seagrass distribution varies severely across scenes. The greatest difference between DTC (total area = 272 hectares) and MLC models (total area between 87 and 183 hectares) was observed on 4 March 2019. This is mostly caused by the large predicted seagrass area (=137 hectares) in deep waters by the DTC model. The MLC_{Base} and $MLC_{10\%}$ models show comparable results across different scenes. The MLC models predicted the least seagrass classified area on 21 August which is illustrated as sparsely distributed pixels in figure 43. Sudden increase of seagrass classified area was observed on 29 November for all MLC models across different water depths. This was less pronounced in the DTC classifications, except at the shallowest waters.

Cross-comparison of seagrass distribution at Sorobon beach

It should be noted that both the DTC and MLC models misclassify fringing reef as seagrass, which causes a gross overestimation of the total area in the shallowest waters. Large seagrass beds in these waters are mostly situated at Sorobon. Figure 42 shows true colour composites of Sorobon across various scenes. The total classified seagrass area is given in figure 43. The restricted MLC models classified the least seagrass beds at Sorobon, whereas the DTC model classified the most. Almost no seagrass was detected by the MLC models on 21 August as previously indicated in figure 41. Overall, both the DTC and MLC models show a comparable trend in estimating seagrass area at Sorobon.

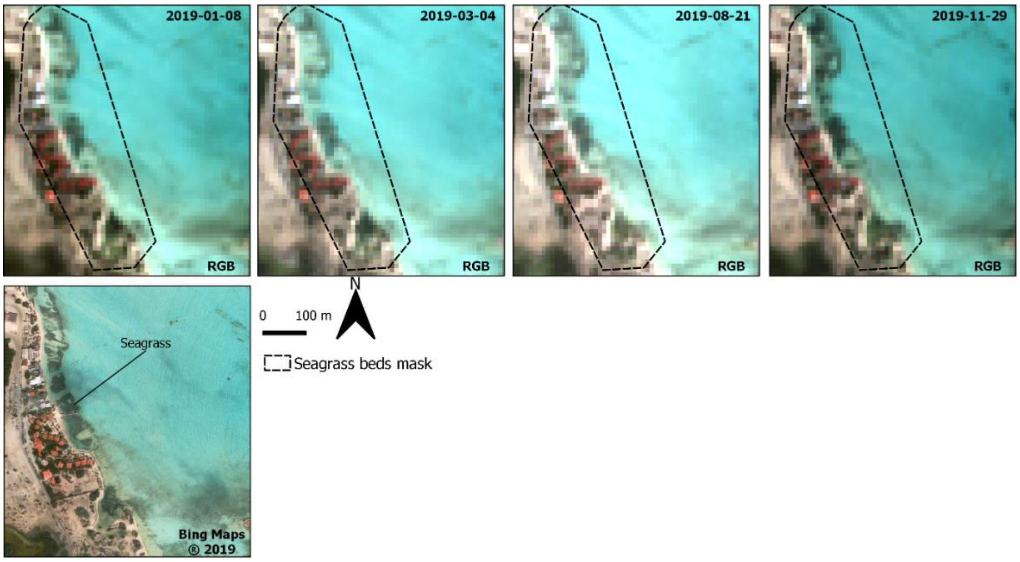

Figure 42. Cross-comparison between true colour composites (Sentinel-2 bands 4,3 and 2) of Sorobon across different scenes. The seagrass beds mask is used to calculate the total area within the mask. A higher resolution true colour base map by Bing Maps ® 2019 is also given as reference.

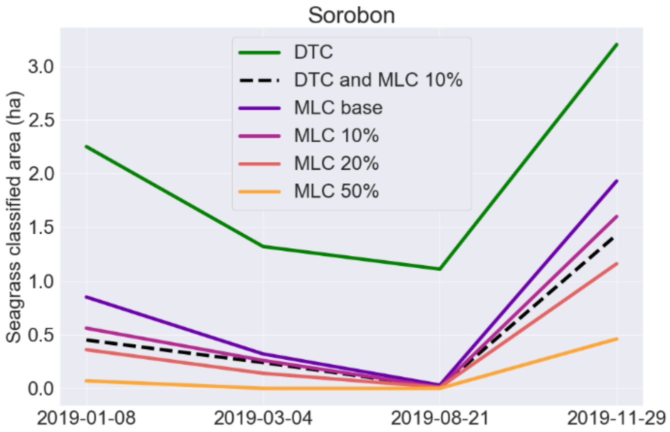

Figure 43. Cross-comparison between DTC and restricted MLC models classified seagrass area (ha) at Sorobon

Misclassification of isolated mangrove stands in Lac Bay

It is also noteworthy that the DTC and MLC$_{20\%}$ models were more robust in avoiding misclassification of isolated mangrove stands (see example in figure 44) located west of Lac Bay. Lesser restricted MLC models than MLC$_{20\%}$ cannot discriminate mangrove and seagrass effectively, whereas the MLC$_{50\%}$ model rejected many seagrass pixels in general.

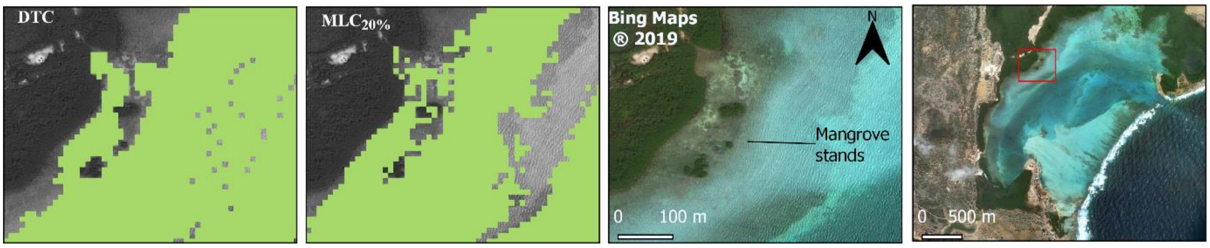

Figure 44. DTC and MLC$_{20\%}$ models predicted seagrass distributions for a scene taken on 29 November 2019 for a subset of Lac Bay. Small isolated mangrove stands can be found in this figure. Grayscale and true colour base maps by Bing Maps ® 2019.

Chapter 4 Discussion

The use of Sentinel-2 remotely sensed images for mapping Sargassum and seagrass are influenced by many factors including image classification techniques, environmental conditions and complexity of the objects of interest. This chapter will review these factors.

4.1 Spectral discrimination of Sargassum

Other floating materials on open sea
In this study, Sargassum was effectively classified based on a combination of bands (B05 and B11 at 705nm and 1610nm) and spectral indices (NDVI and REP) in the visible and near-infrared spectral regions. NDVI uses bands B08 (842nm) and B04 (665nm), whereas the REP uses B05, B06 (740nm) and B07 (783nm). However, Sargassum is not the only floating object found on the Atlantic Ocean with an enhanced near-infrared reflectance. A study by Hu et al., (2015) showed that *Syringodium* (manatee seagrass) wrack, *Trichodesmium* cyanobacteria (sea sawdust), *Ulva prolifera*, garbage and oil spill are regularly found on the Gulf of Mexico and part of the Atlantic Ocean east of Florida. Seagrass wrack, *Ulva prolifera* and *Trichodesmium* cyanobacteria have been observed in the Caribbean Sea as well (Brocke et al., 2018; Debrot et al., 2018; Littler & Littler, 2006). *Ulva prolifera* is a type of green macroalgae which is commonly found on shorelines but also free floating on the water surface. On the other hands, *Trichodesmium* is a cyanobacteria that is found in nutrient-poor waters (Capone et al., 1997) and can form surface slicks similar to Sargassum.

Green algae and floating Sargassum
A comparison between the spectral signatures of Sargassum, *Trichodesmium* cyanobacteria and *Ulva* from the study of Hu et al., (2015) is given in figure 45. The spectral curve of Sargassum has a unique local minimum at around 630 nm. This is due to the absorption of chlorophyll-c pigment in Sargassum (Margulis & Chapman, 2009). Unfortunately, the MSI onboard of Sentinel-2 does not support such spectral feature, hence this local minimum is not visible in figure 16 in section 3.1.2. The spectral shape of Sargassum is comparable with *Ulva prolifera* based on the reflectance intensity around 550 nm (green band) and the near-infrared region. Contrarily, *Trichodesmium* cyanobacteria has a greater intensity at 550 nm compared to Sargassum.

Nevertheless, misclassification of Sargassum might occur if other floating materials with enhanced near-infrared reflectance are present on the satellite image. In this study, objects on the image with enhanced reflectance in the near-infrared region were presumed to be associated with floating Sargassum exclusively. Therefore, the possibility of other macroalgae on the coast, coastal waters and open sea was not investigated.

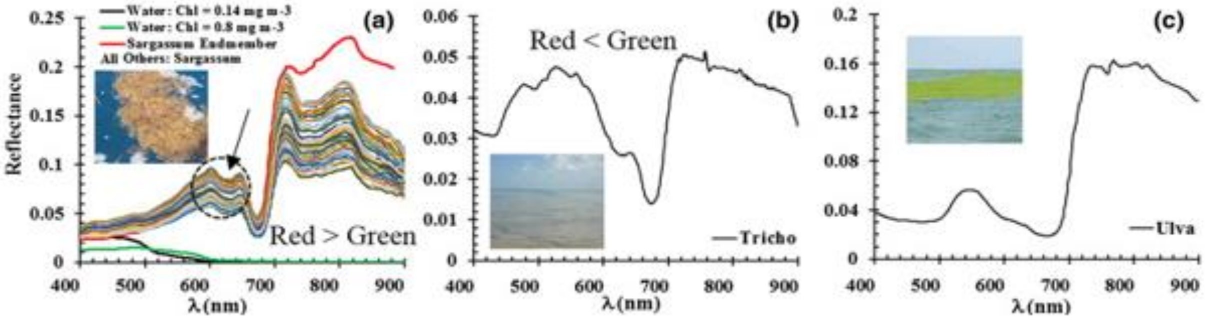

Figure 45. Surface reflectances of Sargassum (a) from the Gulf of Mexico and Atlantic Ocean, Trichodesmium *cyanobacteria (b) from Florida Keys and Ulva prolifera (c) from the Yellow Sea of Qingdao (China). The surface reflectances are measured using a field spectrometer. Figure is adapted from* (Hu et al., 2015)

4.2 Spatial limitation to detect floating Sargassum

Partial coverage required for detecting floating materials

Hu et al. (2015) also investigated the spatial requirement of remote measurements of Sargassum in the Gulf of Mexico and Atlantic Ocean using a WorldView-2 (2m) satellite image. The high-resolution image was resampled (spatial averaging) to a 60m resolution image to assess the proportion of water and Sargassum in a pixel using a linear unmixing model. His results showed that a Sargassum mat with a width greater than 0.6-1.2m (1-2% partial coverage) and length of 180m can be detected on water. The 180 m limit implies three times the pixel length to exclude single-pixel anomaly. The 1-2% partial coverage range depends on the chlorophyll-a concentration (0.14-0.8 mg m^{-3}) in the water, which was used as a metric for turbidity in the study of Hu et al., (2015). High chlorophyll concentration is associated with high water turbidity which limits the detectability of Sargassum.

Partial coverage required for detecting floating Sargassum

In this study, 20m spatial resolution images were resampled to 10m resolution images. Therefore, theoretically, any floating materials on clear water with a width greater than 0.1-0.2m (1-2% of 10m) and length of 30m (3 times 10m pixel) can be detected by Sentinel-2. Hu et al., (2015) also indicated that a partial coverage greater than 20-30% or 2-3m for a 10m image is required to spectrally distinguish Sargassum from other floating materials.

Theoretical minimum Sargassum mat size in this study

An example comparison between false colour composites with different down sampled (spatial averaging) resolutions is shown in figure 46. Based on this comparison, a 30m resolution sensor is still viable for detecting Sargassum slicks. At 60m resolution, the slicks become patchy because most of the reflectance of Sargassum is attenuated by water. At 100m resolution and greater, the Sargassum mat is barely distinguishable from water pixels. The smallest detectable Sargassum mat shown in figure 46 is conservatively estimated between 0.1m (1% of 10m) and 0.6m (1% of 60m) large.

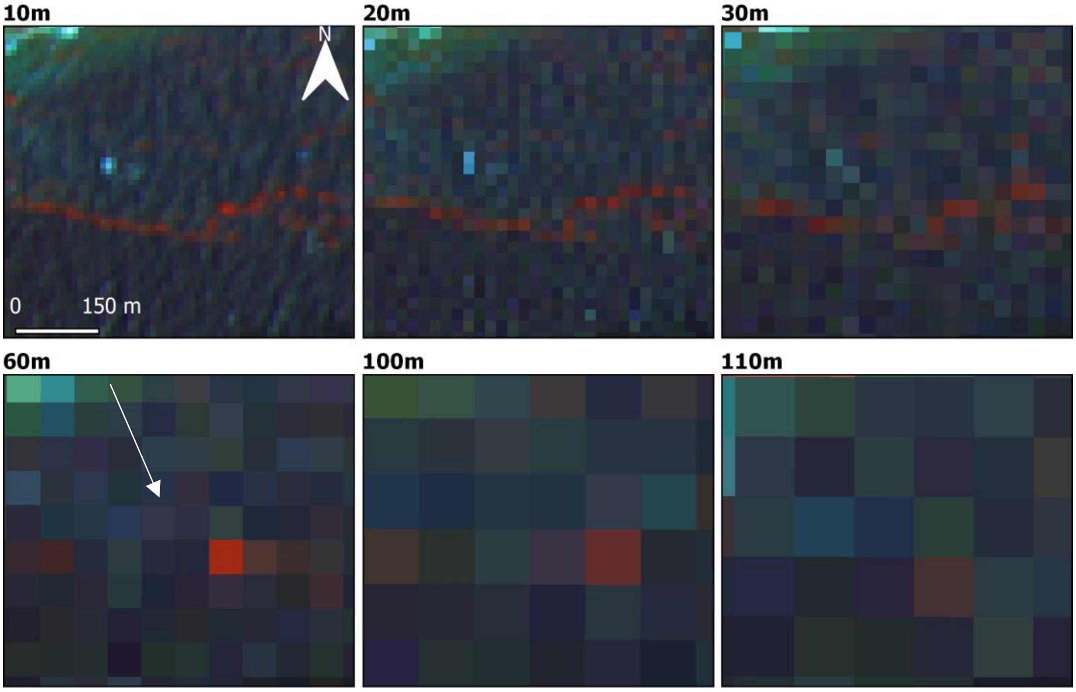

Figure 46. Example false colour composites (Sentinel-2 bands 8, 3 and 2) with different spatial resolutions for a subset taken on 9 March 2019. A Sargassum slick near the east coast of Bonaire is illustrated here. The white arrows indicate where the Sargassum line is not detectable anymore.

4.3 Remote sensing of seagrass in shallow waters

Factors influencing downwelling light

Non-seagrass bottom types were often misclassified as seagrass, because the class distributions are not spectrally separable (see figure 38 section 3.3.1). Deep water pixels tend to be classified as seagrass in Lac Bay. This could be explained due to light attenuation which is inversely related to water depth (Traganos & Reinartz, 2018). Besides, optical properties of water can also influence the scattering, transmission and absorption of downwelling light (Mobley, 2010). Water optical properties depend on the composition and concentration of particles in water and how the light propagates through or out the water. Optically active water constituents (OACs) like phytoplankton, colored dissolved organic matter (CDOM) and non-algal particles can affect remote sensing measurements and classifications (Werdell et al., 2018). In this study, these water elements were not addressed.

Variable light condition and cloudy waters in Lac Bay

It was observed that some water areas in Lac Bay are more turbid which might affect bottom reflectance. This phenomenon can be observed in the water as a faint white substance flowing along the west mangrove fringes of Lac Bay (see figure 47). Moreover, specular reflections, clouds and cloud shadows were also present in the Sentinel-2 images and can affect surface reflectances. The white substance in the water seems to be variable across different scenes and is mostly situated east of Lac Bay. Variable light and cloud conditions depend on the wind and time of the day. It is noteworthy that the Sentinel-2 images used in this study are always taken at 15:07 local time due to its sun-synchronous orbit. However, Sentinel-2 near nadir-viewing sensor (± 10.3° from nadir) is also prone to sun-glint (Roy et al., 2017). According to Mobley (2000), a sensor with a 40° viewing angle from nadir is required to avoid sun-glint. Nevertheless, specular reflection and cloudy water parts could lead to misclassifications.

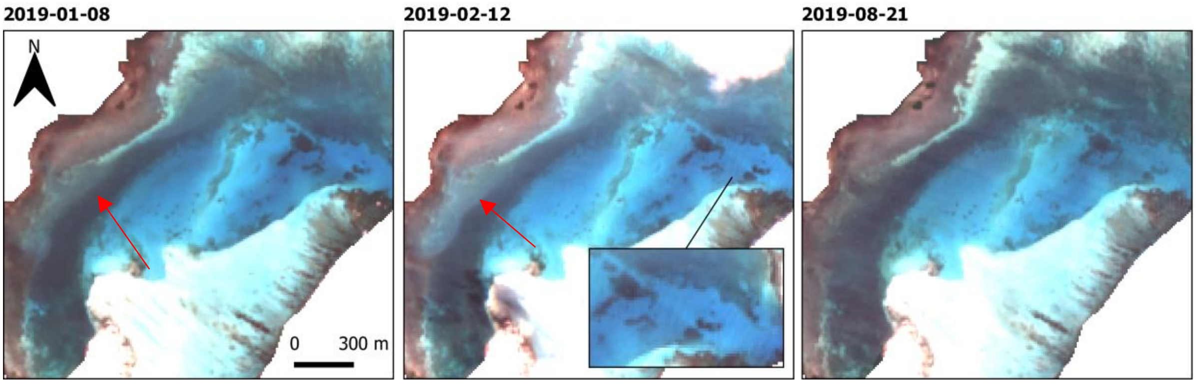

Figure 47. Image enhanced true colour composites (Sentinel-2 bands 4,3,2) of Lac Bay taken in 2019. The red arrows indicate where the water is often turbid (faint white substance). Sun-glint due to water ripples is observed on the middle panel.

4.4 Remote sensing of Sargassum

The adjacency effects

Based on the Jeffries-Matusita distance (Sf-Sl score = 1.6) (appendix 2) both Sargassum classes should be well separated by band B11 (1610nm). However, floating Sargassum (Sf) is often misclassified as Sargassum on land (Sl). It should be noted that misclassification only occurs on Sargassum mats floating close to the coastline and against the mangroves (see figures 19 and 21 in sections 3.1.3 and 3.1.4). This phenomenon might be caused by the adjacency effect which contaminates surface reflectance due to aerosol scattering from neighborhood pixels (Tanre et al., 1981). Adjacency effect can reduce the reflectance over bright pixels because aerosol diffuses outgoing light. It can also reflect incoming light causing increased reflectance over dark pixels

(Lyapustin & Kaufman, 2001). The latter case might have caused a higher reflectance intensity of floating Sargassum, which the DTC and MLC confuse as Sargassum on land.

Mixed pixel of Sargassum on the coast and beach
Pure pixels in the training samples dictate class membership. In reality, multiple classes might occur in a single pixel (Shivakumar & Nagaraja, 2019). Such mixed pixels in the training samples could lead to spectrally mixed reflectances and misclassifications. Figure 48 shows the spectral curve of an example sample point from the coastline. The spectral curve at this site highly resembles Sargassum on land (Sl) which explains why coastline pixels were misclassified as Sargassum. To acquire pure pixels, large homogenous training areas are required (Clevers & Zurita-Milla, 2008). In this study, it was difficult to create such training sites for Sargassum on land (Sl). Most of the eastern coastlines of Bonaire are cliffed, hence Sargassum is less likely to accumulate on the coast but sinks to the bottom of the sea.

Sargassum is more likely to accumulate on flatter shorelines near Lac Bay and on Sorobon beach. It should be noted that the width of Sorobon beach is smaller than 10m, hence Sargassum is partially on land and on water. Moreover, the trees and buildings are very close to the beach which also contributes to mixed pixels and limits the detection of Sargassum with Sentinel-2 images. Consequently, the study put more emphasis on detecting floating Sargassum (Sf) which is in abundance on coastal waters.

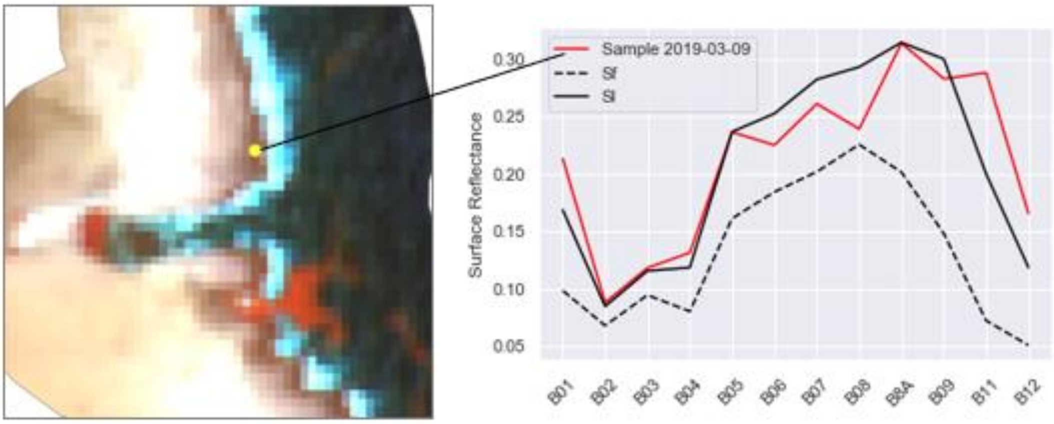

Figure 48. Spectral signature of an example sample point (yellow) from the coastline for a scene taken on 9 March 2019. The surface reflectances (mean values) of the two Sargassum classes (Sf and Sl) from the training samples are also plotted for comparison.

4.5 Performance of image classification techniques

Decision Tree Classification
In this study, multiple DTC parameters were individually assessed using a validation curve. In practice, each parameter could influence one and another. For example, Entropy was mostly used in this study as splitting criterion because it yielded the highest cross-validation accuracy (see Appendices 3 and 8) despite the small difference with Gini (≈1%). However, other studies reported higher classification accuracies when using Gini (Faramarzi et al., 2014; Zambon et al., 2006). Nevertheless, in this study, the influence of the parameter values with respect to the classification results and accuracies were not addressed extensively.

Maximum Likelihood Classification
Maximum Likelihood Classifier is considered as a hard classifier because it assigns a pixel to a class without considering sub-pixel information (mixed pixel) (Das & Singh, 2009). Consequently, it is prone to misclassification due to spectrally similar classes and subclasses

(Kavzoglu & Reis, 2008). Such cases were observed in this study for Sargassum (Sf and Sl) and seagrass classes.

Principal Component Analysis

For operational purposes, a Principal Component Analysis might be less suitable since image interpretation is required to select the best PC image. The scalability performance results in this study also suggest that the recognition of floating Sargassum in the PC images can shift according to the scale of the scene. Moreover, Gupta et al., (2013) stress that temporal variability of other pixels in the image might affect the detection of a target (e.g. Sargassum) in PC images apart from its intrinsic properties. In this study, land pixels (covering east Bonaire) were masked after performing PCA. Mangroves and other terrestrial vegetations are subject to seasonality which influence the feature-space of the near-infrared bands. Consequently, this could shift the contrast of Sargassum to other PC images. This study did not address to what extent seasonality of land pixels could affect the PCA and classifications. Also, the effect of masking land pixels before and after performing PCA was not investigated.

Triangle thresholding

Triangle thresholding is considered a global threshold because it uses the entire image histogram for segmentation. The caveat of such algorithm is that it apts to fail if there is a low contrast between the subject and the background or if the intensity varies across the image (Rogowska, 2009). Low contrast in remote sensing images is mostly caused by atmospheric scattering. The Triangle algorithm implementation in Scikit-Image Python module allows variable bin size that may affect the position of the threshold. Larger bin size implies that very slight differences in pixel intensities could be distinguished in the histogram. In this study, the default value (=256 bins) was used. The effect of variable bin size on the classification results was not explored.

Density slicing

Density slicing is a simple method to segment a grayscale image. This study only explored the effectiveness of the GNDVI which uses a combination of green and near-infrared bands (B03 and B08 at 560mn and 842nm). The water penetrating green band was presumed to be effective in detecting partially submerged Sargassum. It should be noted that this study did not investigate the submerged depth of Sargassum, hence the actual effectiveness of the green band could not be assessed. Therefore, the near-infrared band could be more contributing for the detection of floating Sargassum (Sf) with GNDVI. However, this could be a limiting factor since NIR reflectance is strongly attenuated by water. Hu et al., (2015) estimated a decrease of 47% of the reflectance at 752nm when Sargassum is submerged in water for 0.15m. The absorption of water is weaker in the Red-Edge region, therefore a spectral index using band B05 (at 705nm) might be more effective for detecting submerged Sargassum.

Chapter 5 Conclusions and recommendations

This research explored the limitation and capability of Sentinel-2 imageries for mapping Sargassum and seagrass in Bonaire. The data and Sargassum map in this research can be used as a reference for selecting suitable methods for monitoring Sargassum on coastal waters and open sea in other regions. Besides, the seagrass results may support further studies in improving mapping seagrass in shallow waters. Research questions that were addressed in this study are answered in this chapter. Additionally, a few recommendations are given for further studies.

5.1 Conclusion

RQ 1. To what extent can Sargassum patches be classified on the coast and coastal waters of Bonaire using Sentinel-2 imagery?

Supervised DTC and MLC were employed to map Sargassum on land and water (Sf and Sl) among other coastal features in Bonaire. Based on the training samples, the NDVI, REP, B05 and B11 were found to be useful for classifying both Sargassum classes. The $MLC_{20\%}$ model achieved a validation accuracy of 87% and was found to be the most robust model in classifying floating Sargassum across different scenes while minimizing false positives due to cloud edges and dark mangrove fringes.

Persisting overlap exists between Sargassum on land (Sl) and floating Sargassum (Sf) in the training samples. Consequently, Sargassum on land cannot be classified effectively in this study. The DTC results were comparable with $MLC_{10\%}$, but grossly misclassify floating Sargassum (Sf) as Sargassum on land (Sl) across different scenes. Nevertheless, the $MLC_{50\%}$ model was found applicable for classifying Sargassum on land while minimizing overestimation due to coastline pixels.

RQ 2. To what extent can floating Sargassum patches be classified on open sea with Sentinel-2 imagery?

In this part of the study, unsupervised density slicing of GNDVI image data ($GNDVI_{Slice}$) and PCA combined with Triangle thresholding ($PCA_{Triangle}$) were explored for classifying floating Sargassum (Sf) on east sea of Bonaire. Additionally, the performances of supervised DTC and MLC models on open sea were tested as well. Small subsets located on the east sea of Bonaire were classified to assess the performance of the four classification methods. The result showed that most methods were able to detect large dense Sargassum patches but apt to misclassify cloud edges as floating Sargassum to a certain degree. The $PCA_{Triangle}$ method was found the most effective in classifying floating Sargassum (Sf) on calm and rough waters. This method is excellent in revealing sparsely distributed slicks on the image. However, it should be noted that the $PCA_{Triangle}$ method is more susceptible to image artefacts such as image striping and inter-band parallax.

A larger sea region east of Bonaire was also classified to assess the scalability of the four classification methods in calm open sea. Based on the results, the $PCA_{Triangle}$ method classified the most floating Sargassum of 3911 hectares on 4 March 2018. The MLC_{Base} model classified the second most Sargassum with about 3078 hectares, whereas the $GNDVI_{Slice}$ and DTC methods classified less than 1100 hectares. The pixel-to-pixel similarity map suggested that the $PCA_{Triangle}$ method grossly overestimated cloud edges as floating Sargassum (Sf). This effect was less pronounced in the MLC_{Base} classification results. Therefore, the MLC_{Base} was considered the most robust and effective method in detecting floating Sargassum for a larger sea region under calm sea condition.

RQ 3. Can the impact of Sargassum on seagrass distribution in Lac Bay be mapped with Sentinel-2?

Supervised Decision Trees and Maximum Likelihood classifications were employed to map seagrass distribution in Lac Bay. The intention was to assess the seagrass distributions from before and after the Sargassum invasion in 2019 to reveal most impacted sites. However, the training samples showed severe overlap between seagrass and non-seagrass bottom types which causes gross overestimation of the seagrass classified area. Therefore, in this study, seagrass cannot be classified effectively nor can the impact of Sargassum on its distribution be assessed properly. The comparative study did indicate that fringing coral reefs, deep water pixels and mangrove stands in Lac Bay are most likely misclassified as seagrass.

5.2 Recommendation

Data collection and validation

1. The annual seagrass monitoring dataset is acquired in the field with small (1m^2) quadrants with mixed species. For remote sensing and mapping purposes, homogeneous plots with respect to the minimal mapping unit (MMU) of Sentinel-2 (10m x 10m) are desirable. Roelfsema, Kovacs, et al. (2015) and Roelfsema, Lyons, et al. (2015) presented a georeferenced photo transect sampling method to rapidly collect seagrass coverage data over shallow water (<5m). The method is specially designed to be integrated with remote sensing images for mapping benthic habitats. Such method could be used to collect homogenous samples over a large area like Lac Bay.

2. This study suggested that floating Sargassum (Sf) is often misclassified as deep water (Wd). Therefore, collecting more reference pixels of floating Sargassum and deep-water features on coastal waters and open sea could help improving the separability between these classes. Besides, more reference pixels also mean a larger training dataset that could increase the classification accuracy of the classifier.

3. This study did not assess the validity of Sargassum on land (Sl) because the feature is difficult to interpret on the image. Proper ground truth data is required to accurately validate this class. The coverage maps in the study suggest that flatter shorelines around Lac Bay could be investigated for accumulation of Sargassum during future influxes. Sargassum samples on this site could be collected for training or validating the classification results.

4. Image differencing is a change detection method that could be used to map the effective area of Sargassum between two dates. This is done by subtracting two images (e.g. NDVI) with and without Sargassum. The result is useful for validating classification results or mapping the extent of Sargassum on the coast. The caveat for Sentinel-2 images is that it suffers from multi-temporal registration errors of 10m and 12m (Sentinel-2A and Sentinel-2B) (European Space Agency, 2019) which is roughly the size of a single pixel. Aligning the images before analysis is recommended to avoid errors in the subtracted image.

Classification technique

5. Sub-pixel (or soft) classifiers could be useful for classifying Sargassum and seagrass over heterogeneous areas. Sub-pixel classifiers can better address mixed pixels and ambiguous classes by producing fraction maps. These maps depict the partial class membership within a pixel (Congalton, 2015). Dierssen (2015) and Hu et al. (2015) used Linear Spectral Mixture Analysis (LSMA) to unmix seagrass and Sargassum pixels, respectively. Another study by Frazier and Wang (2011) used Soft Maximum Likelihood

Classification (SMLC) to characterize the distribution of invasive plant species. SMLC uses the posterior probabilities from MLC, also used in this study (see figure 19 and appendix 9), as the sub-pixel fractional covers. Therefore, the MLC implementation in this study could be further developed into a SMLC algorithm.

6. Object-based image analysis (OBIA) is a classification technique that includes contextual information such as texture, shape and size apart from spectral information. Contextual information could be useful for improving the separability between spectrally similar classes such as seagrass and corals. OBIA has been effectively used for mapping benthic habitats (Anggoro et al., 2018; Su and Huang, 2019).

Remote sensing sensor

7. Hu et al., (2015) suggested in their study that that the local reflectance minimum around 630 nm combined with the reflectance ratio between 555 (green) and 650 (red) nm can be used to improve the spectral discrimination of Sargassum from other floating materials on open sea. Current spaceborne remote sensing sensors that closely support this unique spectral fingerprint include: Landsat-8 Operational Land Imager (3rd band with bandwidth: 630-680 nm) and Sentinel-3 Ocean and Land Colour Instrument (7th band with bandwidth: 615-625 nm) (Blix et al., 2018; Knight & Kvaran, 2014). These sensors have higher signal-to-noise ratio (SNR) than Sentinel-2, which could be more effective is detecting Sargassum on rough waters. Note that Landsat-8 and Sentinel-3 operate at 30m and 300m spatial resolutions with revisit times of 16 and 27 days, respectively.

General

8. For an early warning system, the transport and distribution of floating Sargassum on open sea should be further studied. Modelling the transportation of Sargassum requires ancillary information such as sea surface currents and wind data. Recent studies that integrated satellite monitoring and ocean data have shown promising results in predicting the trajectories of Sargassum on open sea (Kwon et al., 2019; Prakash et al., 2018; Putman et al., 2018). These studies used coarse resolution images, therefore the use of Sentinel-2 high-resolution classification data should have the advantage of supporting a more accurate Sargassum forecast.

9. The study revealed that clouds, especially cloud edges, often led to misclassification of Sargassum and other coastal features. The original Sentinel-2 cloud flag was not implemented due to its poor performance. Therefore, a better cloud detection algorithm should be included for future studies. Current state-of-the-art cloud detection frameworks implement a deep learning model that is capable in detecting multitemporal clouds at pixel-level (Tuia et al., 2018). Such cloud detection algorithm is essential for operational monitoring purposes and accurate mapping of Sargassum or seagrass. Moreover, a more effective comparative analysis across different scenes could be performed, which is beneficial for image interpretation and assessing the best classification method.

List of references

Akurathi, R. (2016). *Principal Component Analysis based Assessment of Trees Outside Forests in Satellite Images*. https://doi.org/10.17485/ijst/2016/v9is1/107824

Alawadi, F. (2010). Detection of surface algal blooms using the newly developed algorithm surface algal bloom index (SABI). In *Proceedings of SPIE - The International Society for Optical Engineering* (Vol. 7825). https://doi.org/10.1117/12.862096

Anggoro, A., Sumartono, E., Siregar, V., Agus, S., Purnama, D., Supriyono, S., Puspitosari, D., Listyorini, T., Sulistyo, B., & Parwito, P. (2018). Comparing Object-based and Pixel-based Classifications for Benthic Habitats Mapping in Pari Islands. *Journal of Physics: Conference Series*, *1114*, 12049. https://doi.org/10.1088/1742-6596/1114/1/012049

Atkin, E. (2018). Humans Have Created a New Natural Disaster | The New Republic. Retrieved September 5, 2019, from The New Republic website: https://newrepublic.com/article/150775/humans-created-new-natural-disaster

Ballantyne, A. (2018). Remote Sensing: An Overview of Common Pixel Classification Techniques. Retrieved February 8, 2020, from https://alan.do/remote-sensing-an-overview-of-common-pixel-classification-techniques-4827c4c3a9ff

Bettencourt, J. de, & Imminga-Berends, H. (2015). *Overseas Countries and Territories: Environmental Profiles SECTION A-CARIBBEAN REGION*. Retrieved from https://ec.europa.eu/europeaid/sites/devco/files/octs-environmental-profiles-caribbean-012015_en.pdf

Blanco, A., & Tamondong, A. (2019). Mapping of Sargassum distribution in the Eastern Coast of Southern Leyte Using Sentinel 2 Satellite Imagery. *ISPRS - International Archives of the Photogrammetry, Remote Sensing and Spatial Information Sciences*, *XLII-4/W19*, 289–295. https://doi.org/10.5194/isprs-archives-XLII-4-W19-289-2019

Blix, K., Pálffy, K., Tóth, V., & Eltoft, T. (2018). Remote Sensing of Water Quality Parameters over Lake Balaton by Using Sentinel-3 OLCI. *Water*, *10*, 1428. https://doi.org/10.3390/w10101428

Bonaire Nu. (2018, March 6). Sorobon en Lagoen overspoeld door sargassum Bonaire . Retrieved February 12, 2020, from https://bonaire.nu/2018/03/06/sorobon-en-lagoen-overspoeld-sargassum/

Bonaire Nu. (2019, March 6). Overheid en Stinapa zetten oliebooms in om sargassum tegen te houden Nieuws . Retrieved February 12, 2020, from https://bonaire.nu/2019/03/06/oliebooms-moeten-sargassum-tegenhouden-bij-mangroven/

Brocke, H. J., Piltz, B., Herz, N., Abed, R. M. M., Palinska, K. A., John, U., Haan, J. den, de Beer, D., & Nugues, M. M. (2018). Nitrogen fixation and diversity of benthic cyanobacterial mats on coral reefs in Curaçao. *Coral Reefs*, *37*(3), 861–874. https://doi.org/10.1007/s00338-018-1713-y

Bustamante, J., Pacios, F., Díaz-Delgado, R., & Aragonés, D. (2009). Predictive models of turbidity and water depth in the Doñana marshes using Landsat TM and ETM+ images. *Journal of Environmental Management*, *90*(7), 2219–2225. https://doi.org/https://doi.org/10.1016/j.jenvman.2007.08.021

Butler, J., & Stoner, A. (1984). Pelagic Sargassum: has its biomass changed in the last 50 years? *Deep Sea Research Part A. Oceanographic Research Papers*, *31*, 1259–1264. https://doi.org/10.1016/0198-0149(84)90061-X

Capone, D., Zehr, J., Paerl, H., Bergman, B., & Carpenter, E. (1997). Trichodesmium, a Globally Significant Marine Cyanobacterium. *Science*, *276*, 1221–1229. https://doi.org/10.1126/science.276.5316.1221

Caribbean Regional Fisheries Mechanism. (2014). *Communication Brief of the Caribbean Regional Fisheries Mechanism Secretariat-SARGASSUM SEAWEED INVASION-WHAT, WHY AND WHAT WE CAN DO?* Retrieved from http://www.crfm.int/~uwohxjxf/images/Sargassum_Communication_Brief-_Final.pdf

Christianen, M. (2015, July 30). Experiment on (invasive) seagrass & turtle grazing, Bonaire. Retrieved February 12, 2020, from http://penyu.nl/2015/07/30/experiment-on-seagrass-invasive-species-turtle-grazing-in-bonaire/

Clevers, J. G. P. W., & Zurita-Milla, R. (2008). *3 - Multisensor and multiresolution image fusion using the linear mixing model* (T. B. T.-I. F. Stathaki, Ed.). https://doi.org/https://doi.org/10.1016/B978-0-12-372529-5.00004-4

Coluzzi, R., Imbrenda, V., Maria, L., & Tiziana, S. (2018). A first assessment of the Sentinel-2 Level 1-C cloud mask product to support informed surface analyses. *Remote Sensing of Environment*, *217*, 426–443. https://doi.org/10.1016/j.rse.2018.08.009

Congalton, R. (2015). Remote Sensing and Image Interpretation. 7th Edition. *Photogrammetric Engineering & Remote Sensing*, *81*, 615–616. https://doi.org/10.14358/PERS.81.8.615

Croft-Cusworth, C. (2018). What is blue carbon? A look at ongoing research into the world's water-based carbon sinks. Retrieved September 6, 2019, from CIFOR Forest News website: https://forestsnews.cifor.org/55358/what-is-blue-carbon?fnl=en

Dalezios, N. (2013). REMOTE SENSING POTENTIAL IN HYDROLOGICAL SIMULATION. *Special Collections*.

Das, S., & Singh, R. (2009). Performance of Kriging-Based Soft Classification on WiFS/IRS-1D Image Using Ground Hyperspectral Signatures. *Geoscience and Remote Sensing Letters, IEEE*, *6*, 453–457. https://doi.org/10.1109/LGRS.2009.2016988

Deacon, G. E. R. (1942). The Sargasso Sea. *The Geographical Journal*, *99*(1), 16–28. https://doi.org/10.2307/1788092

Debrot, A. O., Henkens, R. J. H. G., & Verweij, P. J. F. M. (2018). *Staat van de natuur van Caribisch Nederland 2017 : een eerste beoordeling van de staat (van instandhouding), bedreigingen en managementimplicaties van habitats en soorten in Caribisch Nederland*. Retrieved from Wageningen Marine Research website: https://edepot.wur.nl/426340

Dierssen, H. M., Chlus, A., & Russell, B. (2015). Hyperspectral discrimination of floating mats of seagrass wrack and the macroalgae Sargassum in coastal waters of Greater Florida Bay using airborne remote sensing. *Remote Sensing of Environment*, *167*, 247–258. https://doi.org/https://doi.org/10.1016/j.rse.2015.01.027

Dogliotti, A. I., Ruddick, K. G., Nechad, B., Doxaran, D., & Knaeps, E. (2015). A single algorithm to retrieve turbidity from remotely-sensed data in all coastal and estuarine waters. *Remote Sensing of Environment*, *156*, 157–168. https://doi.org/https://doi.org/10.1016/j.rse.2014.09.020

Dutch Caribbean Nature Alliance. (2019). *Prevention and clean-up of Sargassum in the Dutch Caribbean*. Retrieved from https://www.dcnanature.org/wp-content/uploads/2019/02/DCNA-Sargassum-Brief.pdf

El Isleño. (2014). Coralina: "Algas no deben generar preocupación." Retrieved September 5, 2019, from El Isleño website: http://www.elisleño.com/index.php?option=com_content&view=article&id=8320:coralina-algas-no-deben-generar-preocupacion&catid=41:ambiental&Itemid=83

Engel, S. (2013). Invasive Seagrass in Lac Bay, Bonaire. Retrieved September 25, 2019, from https://www.dcnanature.org/invasive-seagrass-in-lac-bonaire/

ESRI. (n.d.). How Principal Components works. Retrieved February 16, 2020, from https://pro.arcgis.com/en/pro-app/tool-reference/spatial-analyst/how-principal-components-works.htm

Estornell, J., Marti Gavilá, J., Sebastiá, M. T., & Mengual, J. (2013). Principal component analysis applied to remote sensing. *Modelling in Science Education and Learning*, *6 (2)*, 83–89. https://doi.org/10.4995/msel.2013.1905

European Space Agency. (2015). *SENTINEL-2 User Handbook* . Retrieved from https://sentinel.esa.int/documents/247904/685211/Sentinel-2_User_Handbook

European Space Agency. (2017). *S2 MPC Level 2A Product Format Specification*. Retrieved from https://sentinel.esa.int/documents/247904/685211/S2+L2A+Product+Definition+Document/2c0f6d5f-60b5-48de-bc0d-e0f45ca06304

European Space Agency. (2019). *L1C Data Quality Report Ref. S2-PDGS-MPC-DQR S2 MPC*. Retrieved from https://sentinel.esa.int/documents/247904/685211/Sentinel-2_L1C_Data_Quality_Report

Fang, H., & Liang, S. B. T.-R. M. in E. S. and E. S. (2014). *Leaf Area Index Models*. https://doi.org/https://doi.org/10.1016/B978-0-12-409548-9.09076-X

Faramarzi, M., Fathizad, H., Pakbaz, N., & Golmohamadi, B. (2014). Application Of Different Methods Of Decision Tree Algorithm For Mapping Rangeland Using Satellite Imagery (Case Study: Doviraj Catchment In Ilam Province). *Journal of Rangeland Science*, *3*, 10.

Frantz, D., Haß, E., Uhl, A., Stoffels, J., & Hill, J. (2018). Improvement of the Fmask algorithm for Sentinel-2 images: Separating clouds from bright surfaces based on parallax effects. *Remote Sensing of Environment*, *215*, 471–481. https://doi.org/10.1016/j.rse.2018.04.046

Frazier, A., & Wang, L. (2011). Characterizing spatial patterns of invasive species using sub-pixel classifications. *Remote Sensing of Environment - REMOTE SENS ENVIRON*, *115*, 1997–2007. https://doi.org/10.1016/j.rse.2011.04.002

Gillies, S., & others. (2013). *Rasterio: geospatial raster I/O for Python programmers*. Retrieved from https://github.com/mapbox/rasterio

Gitelson, A. A., Kaufman, Y. J., & Merzlyak, M. N. (1996). Use of a green channel in remote sensing of global vegetation from EOS-MODIS. *Remote Sensing of Environment*, *58*(3), 289–298. https://doi.org/https://doi.org/10.1016/S0034-4257(96)00072-7

Global Environment Facility. (2018). Communities innovate to address Sargassum seaweed on coasts of Saint Lucia | Global Environment Facility. Retrieved November 15, 2019, from https://www.thegef.org/news/communities-innovate-address-sargassum-seaweed-coasts-saint-lucia

Gower, J., Hu, C., Borstad, G., & King, S. (2007). Ocean Color Satellites Show Extensive Lines of Floating Sargassum in the Gulf of Mexico. *Geoscience and Remote Sensing, IEEE Transactions On*, *44*, 3619–3625. https://doi.org/10.1109/TGRS.2006.882258

Gower, J., & King, S. (2008). Satellite Images Show the Movement of Floating Sargassum in the Gulf of Mexico and Atlantic Ocean. *Nature Precedings*, *3*. https://doi.org/10.1038/npre.2008.1894.1

Gower, J., Young, E., & King, S. (2013). Satellite images suggest a new Sargassum source region in 2011. *Remote Sensing Letters*, *4*. https://doi.org/10.1080/2150704X.2013.796433

Gumma, M. K., Thenkabail, P. S., Teluguntla, P., & Whitbread, A. M. (2019). *Chapter 9 - Indo-Ganges River Basin Land Use/Land Cover (LULC) and Irrigated Area Mapping* (S. I. Khan & T. E. B. T.-I. R. B. Adams, Eds.). https://doi.org/https://doi.org/10.1016/B978-0-12-812782-7.00010-2

Gupta, R. P., Tiwari, R. K., Saini, V., & Srivastava, N. (2013). A Simplified Approach for Interpreting Principal Component Images. *Advances in Remote Sensing*, *02*(02), 111–119. https://doi.org/10.4236/ars.2013.22015

Guyot, G., & Frederic, B. (1988). Utilisation de la Haute Resolution Spectrale pour Suivre L'etat des Couverts Vegetaux. *Proceedings of the 4th International Colloquium on Spectral Signatures of Objects in Remote Sensing Aussios, France, 18-22 January 1988*, *287*, 279.

Haiti Libre. (2015). Haiti - ALERT : Algae invade the coast of the Great South - HaitiLibre.com : Haiti news 7/7. Retrieved September 5, 2019, from Haiti Libre website: https://www.haitilibre.com/en/news-16193-haiti-alert-algae-invade-the-coast-of-the-great-south.html

Hearn, G. E., & Metcalfe, A. V. (1995). *2 - Relationships between variables* (G. E. Hearn & A. V. B. T.-S. A. in E. Metcalfe, Eds.). https://doi.org/https://doi.org/10.1016/B978-034063171-3/50004-X

Higgins, M. (2011). Caribbean Beaches Dig Out From Massive Seaweed Invasion - The New York Times. Retrieved September 5, 2019, from The New York Times website: https://www.nytimes.com/2011/10/16/travel/caribbean-beaches-dig-out-from-massive-seaweed-invasion.html

Hinds, C., Oxenford, H., Cumberbatch, J., Fardin, F., Doyle, E., & Cashman, A. (2016). *Sargassum Management Brief Golden Tides: Management Best Practices for Influxes of Sargassum in the*

Caribbean with a focus on clean-up. Retrieved from https://www.cavehill.uwi.edu/cermes/getdoc/123bf91c-1565-414d-8e21-e59fb6f7ca2d/cermes_sargassum_management_brief_2016_08_24.aspx

Homan, C. (2017). Klimaatverandering op de Caribische Eilanden. Retrieved February 5, 2020, from https://www.knmi.nl/over-het-knmi/nieuws/klimaatverandering-op-de-caribische-eilanden

Hu, C. (2009). A novel ocean color index to detect floating algae in the global oceans. *Remote Sensing of Environment*, *113*(10), 2118–2129. https://doi.org/https://doi.org/10.1016/j.rse.2009.05.012

Hu, C., Feng, L., Hardy, R. F., & Hochberg, E. J. (2015). Spectral and spatial requirements of remote measurements of pelagic Sargassum macroalgae. *Remote Sensing of Environment*, *167*, 229–246. https://doi.org/https://doi.org/10.1016/j.rse.2015.05.022

Ismail, M. H., Pakhriazad, H. Z., & Shahrin, M. F. (2009). Evaluating supervised and unsupervised techniques for land cover mapping using remote sensing data. *Geografia : Malaysian Journal of Society and Space*.

Kavzoglu, T., & Reis, S. (2008). Performance Analysis of Maximum Likelihood and Artificial Neural Network Classifiers for Training Sets with Mixed Pixels. *Giscience & Remote Sensing - GISCI REMOTE SENS*, *45*, 330–342. https://doi.org/10.2747/1548-1603.45.3.330

Kingsford, C., & Salzberg, S. L. (2008). What are decision trees? *Nature Biotechnology*, *26*(9), 1011–1013. https://doi.org/10.1038/nbt0908-1011

Knight, E., & Kvaran, G. (2014). Landsat-8 Operational Land Imager Design, Characterization and Performance. *Remote Sensing*, *6*, 10286–10305. https://doi.org/10.3390/rs61110286

Krümmel, O. (1891). Die nordatlantische Sargassosee. *Petermann's Geographische Mitteilungen*, *37*, 129–141.

Kwon, K., Choi, B.-J., Kim, K. Y., & Kim, K. (2019). Tracing the trajectory of pelagic Sargassum using satellite monitoring and Lagrangian transport simulations in the East China Sea and Yellow Sea. *ALGAE*, *34*(4), 315–326. https://doi.org/10.4490/algae.2019.34.12.11

Laffoley, D., Roe, H., Angel, M. V, Ardron, J., Bates, N., Boyd, L. L., Brooke, S., Buck, K., Carlson, C., Causey, B., Conte, M. H., Christiansen, S., Cleary, J., Donnelly, J., Earle, S. A., Edwards, R., Gjerde, K., Giovannoni, S. J., Gulick, S., & Vats, V. (2011). *The protection and management of the Sargasso Sea: The golden floating rainforest of the Atlantic Ocean: Summary Science and Supporting Evidence Case*. Retrieved from https://www.researchgate.net/publication/299450775_The_protection_and_management_of_the_Sargasso_Sea_The_golden_floating_rainforest_of_the_Atlantic_Ocean_Summary_Science_and_Supporting_Evidence_Case

Lai, J.-S., & Tsai, F. (2019). Improving GIS-based Landslide Susceptibility Assessments with Multi-temporal Remote Sensing and Machine Learning. *Sensors (Basel, Switzerland)*, *19*(17), 3717. https://doi.org/10.3390/s19173717

Lapointe, B. E. (1995). A comparison of nutrient-limited productivity in Sargassum natans from neritic vs. oceanic waters of the western North Atlantic Ocean. *Limnology and Oceanography*. https://doi.org/10.4319/lo.1995.40.3.0625

Li, M., Zang, S., Zhang, B., Li, S., & Wu, C. (2014). A Review of Remote Sensing Image Classification Techniques: the Role of Spatio-contextual Information. *European Journal of Remote Sensing*, *47*(1), 389–411. https://doi.org/10.5721/EuJRS20144723

Littler, D. S., & Littler, M. M. (2006). *REPORT: Bonaire National Marine Park-Algal Survey and Inventory Assess the Current Status of Bonaire's Marine Reefs*.

Lyapustin, A., & Kaufman, Y. J. (2001). Role of adjacency effect in the remote sensing of aerosol. *Journal of Geophysical Research*, *106*, 11909–11916. https://doi.org/10.1029/2000JD900647

Main-Knorn, M., Pflug, B., Louis, J., Debaecker, V., Müller-Wilm, U., & Gascon, F. (2017). Sen2Cor for Sentinel-2. *Image and Signal Processing for Remote Sensing*, 3. https://doi.org/10.1117/12.2278218

Margulis, L., & Chapman, M. J. (2009). *Chapter Two - KINGDOM PROTOCTISTA* (L. Margulis & M. J. B. T.-K. and D. (Fourth E. Chapman, Eds.). https://doi.org/https://doi.org/10.1016/B978-

0-12-373621-5.00002-7

Markuse, P. (2017). Europe Mosaic - Sentinel Hub Temporal Processing. Retrieved January 31, 2020, from https://pierre-markuse.net/2017/11/06/europe-mosaic-sentinel-hub-temporal-processing/

Maselli, F., Conese, C., & Petkov, L. (1994). Use of probability entropy for the estimation and graphical representation of the accuracy of maximum likelihood classifications. *ISPRS Journal of Photogrammetry and Remote Sensing*, *49*(2), 13–20. https://doi.org/https://doi.org/10.1016/0924-2716(94)90062-0

Masson-Delmotte, V., Zhai, P., Pörtner, H. O., D/, R., Skea, J., Shukla, P. R., Pirani, A., Moufouma-Okia, W., Péan, C., Pidcock, R., Connors, S., Matthews, J. B. R., Chen, Y., Zhou, X., Gomis, M. I., Lonnoy, E., Maycock, T., Tignor, M., & Waterfield, T. (2018). *Summary for Policymakers. In: Global warming of 1.5°C. An IPCC Special Report on the impacts of global warming of 1.5°C above pre-industrial levels and related global greenhouse gas emission pathways, in the context of strengthening the global response to*. Geneva.

McFeeters, S. K. (1996). The use of the Normalized Difference Water Index (NDWI) in the delineation of open water features. *International Journal of Remote Sensing*, *17*(7), 1425–1432. https://doi.org/10.1080/01431169608948714

Midwood, J., & Chow-Fraser, P. (2010). Mapping Floating and Emergent Aquatic Vegetation in Coastal Wetlands of Eastern Georgian Bay, Lake Huron, Canada. *Wetlands*, *30*, 1141–1152. https://doi.org/10.1007/s13157-010-0105-z

Miranda, E., Mutiara, A., Emastuti, & Wibowo, W. (2018). *Classification of Land Cover from Sentinel-2 Imagery Using Supervised Classification Technique (Preliminary Study)*. https://doi.org/10.1109/ICIMTech.2018.8528122

Mobley, C. (2000). Estimation of the Remote-Sensing Reflectance from Above-Surface Measurements. *Applied Optics*, *38*, 7442–7455. https://doi.org/10.1364/AO.38.007442

Mobley, C. (2010, February 16). Inherent Optical Properties . Retrieved February 27, 2020, from http://www.oceanopticsbook.info/view/overview_of_optical_oceanography/inherent_optical_properties

Moons, K. (2018). Verstikkend zeewier bedreigt Bonaire. Retrieved September 9, 2019, from Trouw website: https://www.trouw.nl/duurzaamheid-natuur/verstikkend-zeewier-bedreigt-bonaire~bfd4f082/

National Oceanic and Atmospheric Administration. (2017). What are the trade winds? Retrieved February 5, 2020, from https://oceanservice.noaa.gov/facts/tradewinds.html

National Research Council. (2011). *Assessing the Requirements for Sustained Ocean Color Research and Operations*. https://doi.org/10.17226/13127

Nussbaum, S., & Menz, G. (2008). SEaTH Method. In *Object-Based Image Analysis and Treaty Verification: New Approaches in Remote Sensing - Applied to Nuclear Facilities in Iran* (p. 53). Retrieved from https://books.google.nl/books?id=RxHbb3enITYC

Ody, A., Thibaut, T., Berline, L., Changeux, T., André, J.-M., Chevalier, C., Blanfuné, A., Blanchot, J., Ruitton, S., Stiger-Pouvreau, V., Connan, S., Grelet, J., Aurelle, D., Guéné, M., Bataille, H., Bachelier, C., Guillemain, D., Schmidt, N., Fauvelle, V., Guasco, S., & Ménard, F. (2019). From In Situ to satellite observations of pelagic Sargassum distribution and aggregation in the Tropical North Atlantic Ocean. *PLOS ONE*, *14*(9), e0222584. Retrieved from https://doi.org/10.1371/journal.pone.0222584

Parr, A. E. (1939). Quantitative Observations on the Pelagic Sargassum Vegetation of the Western North Atlantic: With Premilinary Discussions of Morphology and Relationships. In *Bulletin of the Bingham Oceanographic Collection*. Retrieved from https://books.google.nl/books?id=Rt-2nQEACAAJ

Pe'eri, S., Morrison, J. R., Short, F., Mathieson, A., & Lippmann, T. (2016). Eelgrass and Macroalgal Mapping to Develop Nutrient Criteria in New Hampshire's Estuaries using Hyperspectral Imagery. *Journal of Coastal Research*, *76*(SI), 209–218. https://doi.org/10.2112/SI76-018

Pedregosa, F., Varoquaux, G., Gramfort, A., Michel, V., Thirion, B., Grisel, O., Blondel, M., Prettenhofer, P., Weiss, R., Dubourg, V., Vanderplas, J., Passos, A., Cournapeau, D., Brucher, M., Perrot, M., Duchesnay, E., & Louppe, G. (2012). Scikit-learn: Machine Learning in Python.

Journal of Machine Learning Research, *12*.

Pink, J. (2018). 5 ways that climate change affects the ocean. Retrieved September 5, 2019, from Conservation International website: https://www.conservation.org/blog/5-ways-that-climate-change-affects-the-ocean

Piragnolo, M., Masiero, A., & Pirotti, F. (2017). Open source R for applying machine learning to RPAS remote sensing images. *Open Geospatial Data, Software and Standards*, *2*(1), 16. https://doi.org/10.1186/s40965-017-0033-4

Platt, T., Hoepffner, N., Stuart, V., & Brown, C. (2008). *Why ocean colour? the societal benefits of ocean-colour technology*. https://doi.org/10.25607/OBP-97

Platt, T., & Sathyendranath, S. (2008). Ecological indicators for the pelagic zone of the ocean from remote sensing. *Remote Sensing of Environment*, *112*, 3426–3436. https://doi.org/10.1016/j.rse.2007.10.016

Pooja, A. P., Jayanth, J., & Koliwad, S. (2011). Classification of RS data using decision tree approach. *International Journal of Computer Applications*, *23*(3), 7–11.

Prakash, D., Dicopolous, J., Roarty, H., Morell, J., Canals, M., & Evans, C. (2018). *Development of Sargassum Seaweed Tracking Tools*. https://doi.org/10.1109/OCEANS.2018.8604742

Putman, N. F., Goni, G. J., Gramer, L. J., Hu, C., Johns, E. M., Trinanes, J., & Wang, M. (2018). Simulating transport pathways of pelagic Sargassum from the Equatorial Atlantic into the Caribbean Sea. *Progress in Oceanography*, *165*, 205–214. https://doi.org/https://doi.org/10.1016/j.pocean.2018.06.009

Radboud Universiteit. (2019, September 13). Zon, zee, strand en... bruinwier: een ecologische ramp. Retrieved February 12, 2020, from https://www.ru.nl/nieuws-agenda/vm/2019/september/zon-zee-strand-bruinwier-ecologische-ramp/

Richards, J. A. (2013). *Remote Sensing Digital Image Analysis, An Introduction* (5th ed.). https://doi.org/10.1007/978-3-642-30062-2

Roelfsema, C., Kovacs, E., & Phinn, S. (2015). Field data sets for seagrass biophysical properties for the Eastern Banks, Moreton Bay, Australia, 2004-2014. *Scientific Data*, *2*, 150040. https://doi.org/10.1038/sdata.2015.40

Roelfsema, C., Lyons, Dunbabin, Kovacs, E., & Phinn, S. (2015). Integrating field survey data with satellite image data to improve shallow water seagrass maps: The role of AUV and snorkeller surveys? *Remote Sensing Letters*, *6*. https://doi.org/10.1080/2150704X.2015.1013643

Rogowska, J. (2009). *Chapter 5 - Overview and Fundamentals of Medical Image Segmentation* (I. N. B. T.-H. of M. I. P. and A. (Second E. BANKMAN, Ed.). https://doi.org/https://doi.org/10.1016/B978-012373904-9.50013-1

Rouse, J. W., Haas, R. H., Schell, J. A., & Deering, D. W. (1973). Monitoring vegetation systems in the Great Plains with ERTS. *Third Earth Resources Technology Satellite-1 Symposium-Volume I: Technical Presentations, NASA*, *1*, 309–317.

Roy, D. P., Li, J., Zhang, H. K., Yan, L., Huang, H., & Li, Z. (2017). Examination of Sentinel-2A multi-spectral instrument (MSI) reflectance anisotropy and the suitability of a general method to normalize MSI reflectance to nadir BRDF adjusted reflectance. *Remote Sensing of Environment*, *199*, 25–38. https://doi.org/https://doi.org/10.1016/j.rse.2017.06.019

Scheunders, P., Tuia, D., & Moser, G. (2018). *2.10 - Contributions of Machine Learning to Remote Sensing Data Analysis* (S. B. T.-C. R. S. Liang, Ed.). https://doi.org/https://doi.org/10.1016/B978-0-12-409548-9.10343-4

Shivakumar, B. R., & Nagaraja, G. (2019). Sensitivity Analysis of Support Vector Machines on Landsat 8 Image Classification in Original Multidimensional Feature Space: A Kernel Approach -Part 1. *The International Journal of Analytical and Experimental Modal Analysis*, *XI*, 3983–3991.

Siddiqui, M., & Zaidi, A. (2015). Worldview-2 and Landsat 8 Satellite Data for Seaweed Mapping along Karachi Coast. *Pakistan Journal of Engineering, Technology & Science*, *5*(2), 134–151. https://doi.org/10.22555/pjets.v5i2.920

Siddiqui, M., Zaidi, A., & Abdullah, M. (2019). Performance Evaluation of Newly Proposed Seaweed Enhancing Index (SEI). *Remote Sensing*, *11*, 1434.

https://doi.org/10.3390/rs11121434

STINAPA Bonaire. (n.d.). Lac Zonation. Retrieved September 27, 2019, from https://stinapabonaire.org/bonaire-national/lac-zonation/

Su, L., & Huang, Y. (2019). Seagrass Resource Assessment Using WorldView-2 Imagery in the Redfish Bay, Texas. *Journal of Marine Science and Engineering*, *7*, 98. https://doi.org/10.3390/jmse7040098

Swain, P. H., & Davis, S. M. (1978). *Remote sensing: The quantitative approach*. Retrieved from https://books.google.nl/books?id=Jf9OAAAAMAAJ

Tamis, J. E., & Foekema, E. M. (2016). *Blue carbon in the Dutch Caribbean*. Retrieved from https://edepot.wur.nl/368993

Tanre, D., Herman, M., & Deschamps, P. Y. (1981). Influence of the background contribution upon space measurements of ground reflectance. *Applied Optics*, *20*(20), 3676–3684. https://doi.org/10.1364/AO.20.003676

Teoh, K. K., Ibrahim, H., & Bejo, S. K. (2008). Investigation on several basic interpolation methods for the use in remote sensing application. *2008 IEEE Conference on Innovative Technologies in Intelligent Systems and Industrial Applications*, 60–65. https://doi.org/10.1109/CITISIA.2008.4607336

Terletzky, P., & Ramsey, R. (2016). Comparison of Three Techniques to Identify and Count Individual Animals in Aerial Imagery. *Journal of Signal and Information Processing*, *07*, 123–135. https://doi.org/10.4236/jsip.2016.73013

Thang, H., Manley-Harris, M., Pham, T. D., & Hawes, I. (2020). A Comparative Assessment of Ensemble-Based Machine Learning and Maximum Likelihood Methods for Mapping Seagrass Using Sentinel-2 Imagery in Tauranga Harbor, New Zealand. *Remote Sensing*, *12*, 355. https://doi.org/10.3390/rs12030355

Torbick, N., & Becker, B. (2009). Evaluating principal components analysis for identifying Optimal bands using wetland hyperspectral measurements from the Great Lakes, USA. *Remote Sensing*. https://doi.org/10.3390/rs1030408

Traganos, D., & Reinartz, P. (2018). Mapping Mediterranean seagrasses with Sentinel-2 imagery. *Marine Pollution Bulletin*, *134*, 197–209. https://doi.org/https://doi.org/10.1016/j.marpolbul.2017.06.075

Tuia, D., Kellenberger, B., Perez-Suey, A., & Camps-Valls, G. (2018). A Deep Network Approach to Multitemporal Cloud Detection. *IGARSS 2018 - 2018 IEEE International Geoscience and Remote Sensing Symposium*, 4351–4354. https://doi.org/10.1109/IGARSS.2018.8517312

University of South Florida. (n.d.). Sargassum blooms in the Caribbean Sea. Retrieved December 27, 2019, from https://optics.marine.usf.edu/projects/saws.html

University of South Florida Optical Oceanography Lab. (n.d.). Satellite-based Sargassum Watch System (SaWS). Retrieved February 14, 2020, from https://optics.marine.usf.edu/projects/saws.html

Van Dam, A. (2019). World Wetlands Day 2019: the Ramsar Convention on Wetlands remains important | IHE Delft Institute for Water Education. Retrieved September 6, 2019, from IHE Delft website: https://www.un-ihe.org/stories/world-wetlands-day-2019-ramsar-convention-wetlands-remains-important

van der Walt, S., Schönberger, J., Nunez-Iglesias, J., Boulogne, F., Warner, J., Yager, N., Gouillart, E., Yu, T., & contributors, the. (2014). scikit-image: Image processing in Python. *PeerJ*, *2*. https://doi.org/10.7717/peerj.453

Van Moorsel, G., & Meijer, M. (1994). *Base-line ecological study van het Lac op Bonaire*. Culemborg.

Van Tussenbroek, B. I., Hernández Arana, H. A., Rodríguez-Martínez, R. E., Espinoza-Avalos, J., Canizales-Flores, H. M., González-Godoy, C. E., Barba-Santos, M. G., Vega-Zepeda, A., & Collado-Vides, L. (2017). Severe impacts of brown tides caused by Sargassum spp. on near-shore Caribbean seagrass communities. *Marine Pollution Bulletin*, *122*(1), 272–281. https://doi.org/https://doi.org/10.1016/j.marpolbul.2017.06.057

VanderPlas, J. (2016). *Python Data Science Handbook: Essential Tools for Working with Data* (1st ed.). O'Reilly Media, Inc.

Verweij, P. (2018). Raw data of seagrass observations. Retrieved September 25, 2019, from https://www.dcbd.nl/author/engel-s

Vos, B., Foursoff, W., de Bruijn, L., & Bruijn, W. (2016). *Coastal Seaweed Solutions* (Technische Universiteit Delft). Retrieved from https://repository.tudelft.nl/islandora/object/uuid:4de9aa1b-a9a9-4dcb-bfef-82fe4ae0584c?collection=education

Wang, M., & Hu, C. (2016). Mapping and quantifying Sargassum distribution and coverage in the Central West Atlantic using MODIS observations. *Remote Sensing of Environment*, *183*, 350–367. https://doi.org/https://doi.org/10.1016/j.rse.2016.04.019

Wang, M., Hu, C., Barnes, B. B., Mitchum, G., Lapointe, B., & Montoya, J. P. (2019). The great Atlantic Sargassum belt. *Science*, *365*(6448), 83–87. https://doi.org/10.1126/science.aaw7912

Weijerman, M., Lindeboom, H., & Zuur, A. (2005). Regime shifts in marine ecosystems of the North Sea and Wadden Sea. *Marine Ecology-Progress Series*, *298*, 21–39. https://doi.org/10.3354/meps298021

Werdell, P. J., McKinna, L. I. W., Boss, E., Ackleson, S. G., Craig, S. E., Gregg, W. W., Lee, Z., Maritorena, S., Roesler, C. S., Rousseaux, C. S., Stramski, D., Sullivan, J. M., Twardowski, M. S., Tzortziou, M., & Zhang, X. (2018). An overview of approaches and challenges for retrieving marine inherent optical properties from ocean color remote sensing. *Progress in Oceanography*, *160*, 186–212. https://doi.org/https://doi.org/10.1016/j.pocean.2018.01.001

Winge, O. (1923). The Sargasso Sea, its boundaries and vegetation. *Report on the Danish Oceanographical Expeditions 1908-1910 to the Mediterranean and Adjacent Seas*, *Vol. III.*, 34.

Xing, Q., & Hu, C. (2016). Mapping macroalgal blooms in the Yellow Sea and East China Sea using HJ-1 and Landsat data: Application of a virtual baseline reflectance height technique. *Remote Sensing of Environment*, *178*, 113–126. https://doi.org/https://doi.org/10.1016/j.rse.2016.02.065

Zack, G. W., Rogers, W. E., & Latt, S. A. (1977). Automatic measurement of sister chromatid exchange frequency. *Journal of Histochemistry and Cytochemistry*. https://doi.org/10.1177/25.7.70454

Zambon, M., Lawrence, R., Bunn, A., & Powell, S. (2006). Effect of Alternative Splitting Rules on Image Processing Using Classification Tree Analysis. *Photogrammetric Engineering & Remote Sensing*, *72*, 25–30. https://doi.org/10.14358/PERS.72.1.25

Zhou, V. (2019, June 7). A Simple Explanation of Information Gain and Entropy. Retrieved February 9, 2020, from https://victorzhou.com/blog/information-gain/

Appendix 1 Sampled dataset covering eight classes obtained from the coast and coastal waters

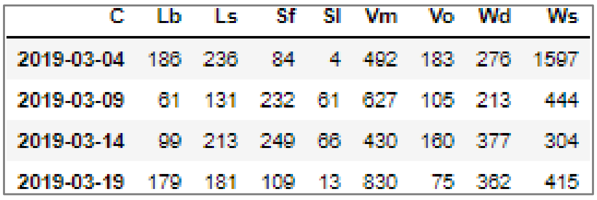

C	Lb	Ls	Sf	Sl	Vm	Vo	Wd	Ws
2019-03-04	186	236	84	4	492	183	276	1597
2019-03-09	61	131	232	61	627	105	213	444
2019-03-14	99	213	249	66	430	160	377	304
2019-03-19	179	181	109	13	830	75	362	415

Number of sampled pixels from each Sentinel-2 scene before undersampling

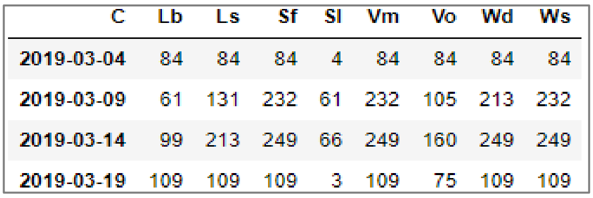

C	Lb	Ls	Sf	Sl	Vm	Vo	Wd	Ws
2019-03-04	84	84	84	4	84	84	84	84
2019-03-09	61	131	232	61	232	105	213	232
2019-03-14	99	213	249	66	249	160	249	249
2019-03-19	109	109	109	3	109	75	109	109

Number of sampled pixels from each Sentinel-2 scene after undersampling

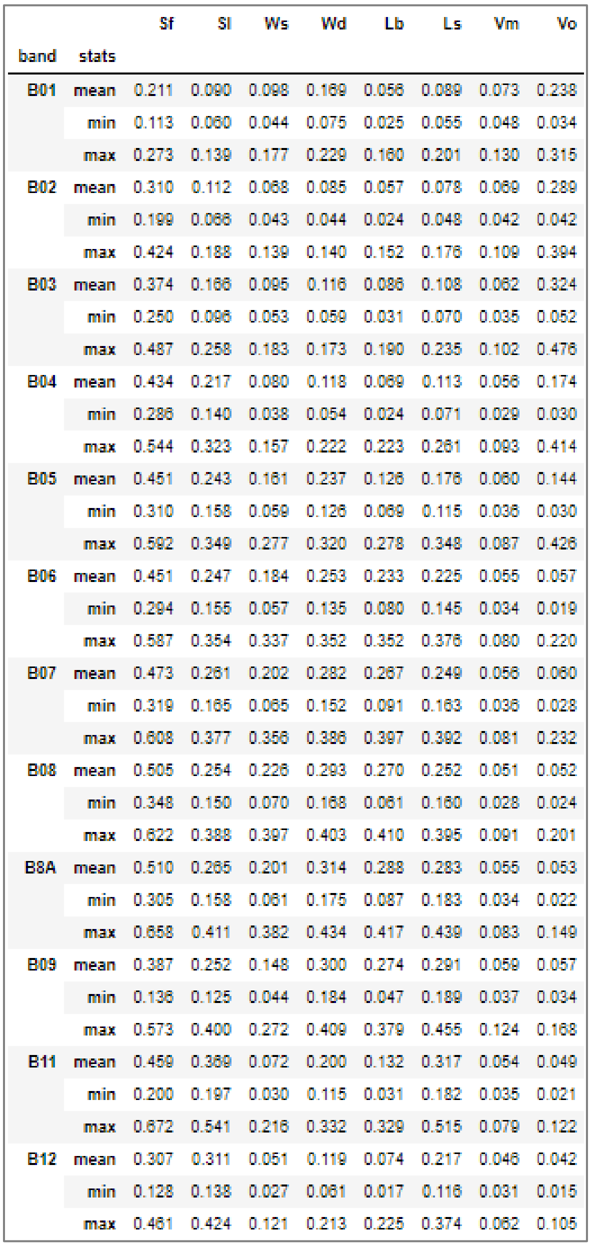

		Sf	Sl	Ws	Wd	Lb	Ls	Vm	Vo
band	**stats**								
B01	**mean**	0.211	0.090	0.098	0.169	0.056	0.089	0.073	0.238
	min	0.113	0.060	0.044	0.075	0.025	0.055	0.048	0.034
	max	0.273	0.139	0.177	0.229	0.160	0.201	0.130	0.315
B02	**mean**	0.310	0.112	0.068	0.085	0.057	0.078	0.069	0.289
	min	0.199	0.066	0.043	0.044	0.024	0.048	0.042	0.042
	max	0.424	0.188	0.139	0.140	0.152	0.176	0.109	0.394
B03	**mean**	0.374	0.166	0.095	0.116	0.086	0.108	0.062	0.324
	min	0.250	0.096	0.053	0.059	0.031	0.070	0.035	0.052
	max	0.487	0.258	0.183	0.173	0.190	0.235	0.102	0.476
B04	**mean**	0.434	0.217	0.080	0.118	0.069	0.113	0.056	0.174
	min	0.286	0.140	0.038	0.054	0.024	0.071	0.029	0.030
	max	0.544	0.323	0.157	0.222	0.223	0.261	0.093	0.414
B05	**mean**	0.451	0.243	0.161	0.237	0.126	0.176	0.060	0.144
	min	0.310	0.158	0.059	0.126	0.069	0.115	0.036	0.030
	max	0.592	0.349	0.277	0.320	0.278	0.348	0.087	0.426
B06	**mean**	0.451	0.247	0.184	0.253	0.233	0.225	0.055	0.057
	min	0.294	0.155	0.057	0.135	0.080	0.145	0.034	0.019
	max	0.587	0.354	0.337	0.352	0.352	0.376	0.080	0.220
B07	**mean**	0.473	0.261	0.202	0.282	0.267	0.249	0.056	0.060
	min	0.319	0.165	0.065	0.152	0.091	0.163	0.036	0.028
	max	0.608	0.377	0.356	0.386	0.397	0.392	0.081	0.232
B08	**mean**	0.505	0.254	0.226	0.293	0.270	0.252	0.051	0.052
	min	0.348	0.150	0.070	0.168	0.061	0.160	0.028	0.024
	max	0.622	0.388	0.397	0.403	0.410	0.395	0.091	0.201
B8A	**mean**	0.510	0.265	0.201	0.314	0.288	0.283	0.055	0.053
	min	0.305	0.158	0.061	0.175	0.087	0.183	0.034	0.022
	max	0.658	0.411	0.382	0.434	0.417	0.439	0.083	0.149
B09	**mean**	0.387	0.252	0.148	0.300	0.274	0.291	0.059	0.057
	min	0.136	0.125	0.044	0.184	0.047	0.189	0.037	0.034
	max	0.573	0.400	0.272	0.409	0.379	0.455	0.124	0.168
B11	**mean**	0.459	0.369	0.072	0.200	0.132	0.317	0.054	0.049
	min	0.200	0.197	0.030	0.115	0.031	0.182	0.035	0.021
	max	0.672	0.541	0.216	0.332	0.329	0.515	0.079	0.122
B12	**mean**	0.307	0.311	0.051	0.119	0.074	0.217	0.046	0.042
	min	0.128	0.138	0.027	0.061	0.017	0.116	0.031	0.015
	max	0.461	0.424	0.121	0.213	0.225	0.374	0.062	0.105

Statistical summary of total dataset before undersampling

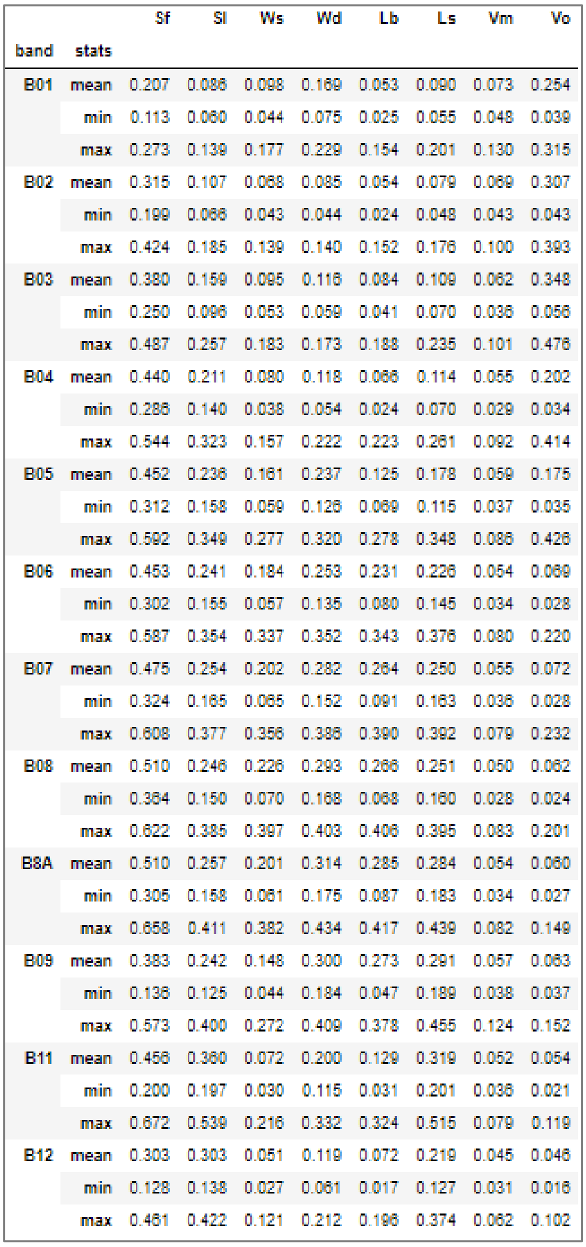

		Sf	Sl	Ws	Wd	Lb	Ls	Vm	Vo
band	**stats**								
B01	**mean**	0.207	0.086	0.098	0.169	0.053	0.090	0.073	0.254
	min	0.113	0.060	0.044	0.075	0.025	0.055	0.048	0.039
	max	0.273	0.139	0.177	0.229	0.154	0.201	0.130	0.315
B02	**mean**	0.315	0.107	0.068	0.085	0.054	0.079	0.069	0.307
	min	0.199	0.066	0.043	0.044	0.024	0.048	0.043	0.043
	max	0.424	0.185	0.139	0.140	0.152	0.176	0.100	0.393
B03	**mean**	0.380	0.159	0.095	0.116	0.084	0.109	0.062	0.348
	min	0.250	0.096	0.053	0.059	0.041	0.070	0.036	0.056
	max	0.487	0.257	0.183	0.173	0.188	0.235	0.101	0.476
B04	**mean**	0.440	0.211	0.080	0.118	0.066	0.114	0.055	0.202
	min	0.286	0.140	0.038	0.054	0.024	0.070	0.029	0.034
	max	0.544	0.323	0.157	0.222	0.223	0.261	0.092	0.414
B05	**mean**	0.452	0.236	0.161	0.237	0.125	0.178	0.059	0.175
	min	0.312	0.158	0.059	0.126	0.069	0.115	0.037	0.035
	max	0.592	0.349	0.277	0.320	0.278	0.348	0.086	0.426
B06	**mean**	0.453	0.241	0.184	0.253	0.231	0.226	0.054	0.069
	min	0.302	0.155	0.057	0.135	0.080	0.145	0.034	0.028
	max	0.587	0.354	0.337	0.352	0.343	0.376	0.080	0.220
B07	**mean**	0.475	0.254	0.202	0.282	0.264	0.250	0.055	0.072
	min	0.324	0.165	0.065	0.152	0.091	0.163	0.036	0.028
	max	0.608	0.377	0.356	0.386	0.390	0.392	0.079	0.232
B08	**mean**	0.510	0.246	0.226	0.293	0.266	0.251	0.050	0.062
	min	0.364	0.150	0.070	0.168	0.068	0.160	0.028	0.024
	max	0.622	0.385	0.397	0.403	0.406	0.395	0.083	0.201
B8A	**mean**	0.510	0.257	0.201	0.314	0.285	0.284	0.054	0.060
	min	0.305	0.158	0.061	0.175	0.087	0.183	0.034	0.027
	max	0.658	0.411	0.382	0.434	0.417	0.439	0.082	0.149
B09	**mean**	0.383	0.242	0.148	0.300	0.273	0.291	0.057	0.063
	min	0.136	0.125	0.044	0.184	0.047	0.189	0.038	0.037
	max	0.573	0.400	0.272	0.409	0.378	0.455	0.124	0.152
B11	**mean**	0.456	0.360	0.072	0.200	0.129	0.319	0.052	0.054
	min	0.200	0.197	0.030	0.115	0.031	0.201	0.036	0.021
	max	0.672	0.539	0.216	0.332	0.324	0.515	0.079	0.119
B12	**mean**	0.303	0.303	0.051	0.119	0.072	0.219	0.045	0.046
	min	0.128	0.138	0.027	0.061	0.017	0.127	0.031	0.016
	max	0.461	0.422	0.121	0.212	0.196	0.374	0.062	0.102

Statistical summary of total dataset after undersampling

	B01	B02	B03	B04	B05	B06	B07	B08	B8A	B09	B11	B12
B01	0.000831264	0.000140821	0.000202186	0.000129128	0.00028215	0.000197397	0.000107228	0.000248597	4.36635e-05	2.29903e-05	1.68761e-05	2.96159e-05
B02	0.000140821	0.00020713	0.000196663	0.000196525	4.10864e-05	-6.10467e-05	-8.46822e-05	-8.5309e-05	-6.68179e-05	0.000105841	0.000194677	0.000121137
B03	0.000202186	0.000196663	0.00029751	0.000279466	0.000342179	0.000344628	0.00035271	0.000458831	0.000392347	0.000368533	0.000217551	0.000115346
B04	0.000129128	0.000196525	0.000279466	0.000382902	0.00040302	0.000456276	0.000504832	0.000616572	0.000646808	0.000628209	0.00042319	0.000221475
B05	0.00028215	4.10864e-05	0.000342179	0.00040302	0.00167168	0.00228785	0.00251188	0.00266824	0.00271407	0.00162865	0.000310052	7.40635e-05
B06	0.000197397	-6.10467e-05	0.000344628	0.000456276	0.00228785	0.00341333	0.00378122	0.0040174	0.00414712	0.00245889	0.000398735	6.12376e-05
B07	0.000107228	-8.46822e-05	0.00035271	0.000504832	0.00251188	0.00378122	0.00424721	0.00450204	0.00469442	0.00283348	0.000480438	7.80699e-05
B08	0.000248597	-8.5309e-05	0.000458831	0.000616572	0.00266824	0.0040174	0.00450204	0.00547967	0.00509972	0.00320707	0.000637637	0.000136847
B8A	4.36635e-05	-6.68179e-05	0.000392347	0.000646808	0.00271407	0.00414712	0.00469442	0.00509972	0.00545506	0.00352093	0.000795617	0.00021028
B09	2.29903e-05	0.000105841	0.000368533	0.000628209	0.00162865	0.00245889	0.00283348	0.00320707	0.00352093	0.00329156	0.000935782	0.000363296
B11	1.68761e-05	0.000194677	0.000217551	0.00042319	0.000310052	0.000398735	0.000480438	0.000637637	0.000795617	0.000935782	0.00080016	0.000419714
B12	2.96159e-05	0.000121137	0.000115346	0.000221475	7.40635e-05	6.12376e-05	7.80699e-05	0.000136847	0.00021028	0.000363296	0.000419714	0.000240354

Band covariance matrix of floating Sargassum from the resampled dataset. The sampling variance is highlighted in the diagonal.

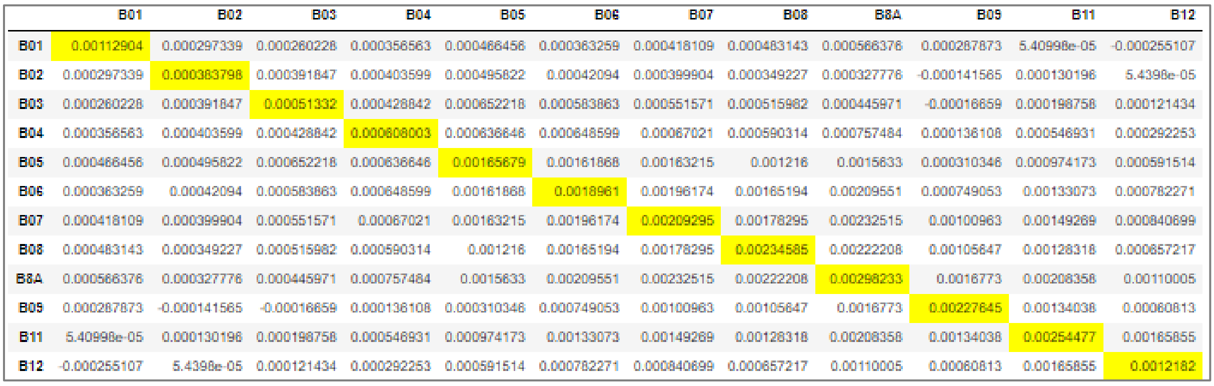

	B01	B02	B03	B04	B05	B06	B07	B08	B8A	B09	B11	B12
B01	0.00112904	0.000297339	0.000260228	0.000356563	0.000466456	0.000363259	0.000418109	0.000483143	0.000566376	0.000287873	5.40998e-05	-0.000255107
B02	0.000297339	0.000383798	0.000391847	0.000403599	0.000495822	0.00042094	0.000399904	0.000349227	0.000327776	-0.000141565	0.000130196	5.4398e-05
B03	0.000260228	0.000391847	0.00051332	0.000428842	0.000652218	0.000583863	0.000551571	0.000515982	0.000445971	-0.00016659	0.000198758	0.000121434
B04	0.000356563	0.000403599	0.000428842	0.000608003	0.000636646	0.000648599	0.00067021	0.000590314	0.000757484	0.000136108	0.000546931	0.000292253
B05	0.000466456	0.000495822	0.000652218	0.000636646	0.00165679	0.00161868	0.00163215	0.001216	0.0015633	0.000310346	0.000974173	0.000591514
B06	0.000363259	0.00042094	0.000583863	0.000648599	0.00161868	0.0018961	0.00196174	0.00165194	0.00209551	0.000749053	0.00133073	0.000782271
B07	0.000418109	0.000399904	0.000551571	0.00067021	0.00163215	0.00196174	0.00209295	0.00178295	0.00232515	0.00100963	0.00149269	0.000840699
B08	0.000483143	0.000349227	0.000515982	0.000590314	0.001216	0.00165194	0.00178295	0.00234585	0.00222208	0.00105647	0.00128318	0.000657217
B8A	0.000566376	0.000327776	0.000445971	0.000757484	0.0015633	0.00209551	0.00232515	0.00222208	0.00298233	0.0016773	0.00208358	0.00110005
B09	0.000287873	-0.000141565	-0.00016659	0.000136108	0.000310346	0.000749053	0.00100963	0.00105647	0.0016773	0.00227645	0.00134038	0.00060813
B11	5.40998e-05	0.000130196	0.000198758	0.000546931	0.000974173	0.00133073	0.00149269	0.00128318	0.00208358	0.00134038	0.00254477	0.00165855
B12	-0.000255107	5.4398e-05	0.000121434	0.000292253	0.000591514	0.000782271	0.000840699	0.000657217	0.00110005	0.00060813	0.00165855	0.0012182

Band covariance matrix of Sargassum on land from the resampled dataset. The sampling variance is highlighted in the diagonal. Note that Sargassum on land was not under sampled hence the variance before-and after resampling is the same.

Appendix 2 Jeffries-Matusita distance heatmap

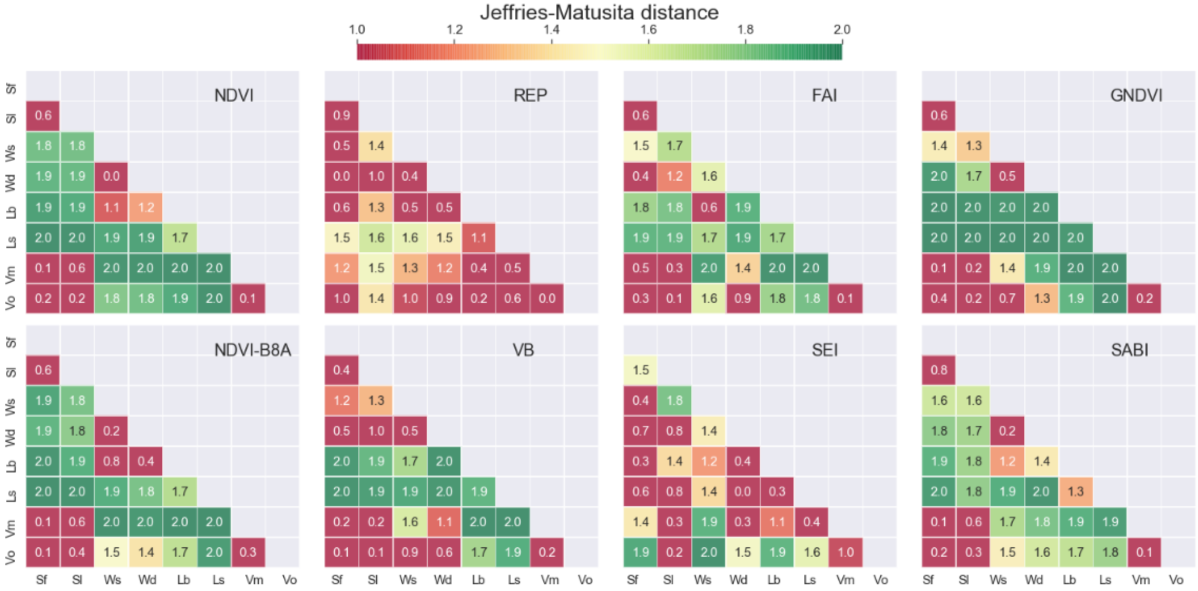

Heatmaps showing the Jeffries- Matusita separability scores between eight classes for each remote sensing index. Values greater than 1.5 indicate high separability.

Heatmaps showing the Jeffries- Matusita separability scores between eight classes for each band. Values greater than 1.5 indicate high separability.

Appendix 3 Hyperparameters tuning and cross-validation of Decision Tree Classifier for Sargassum classification

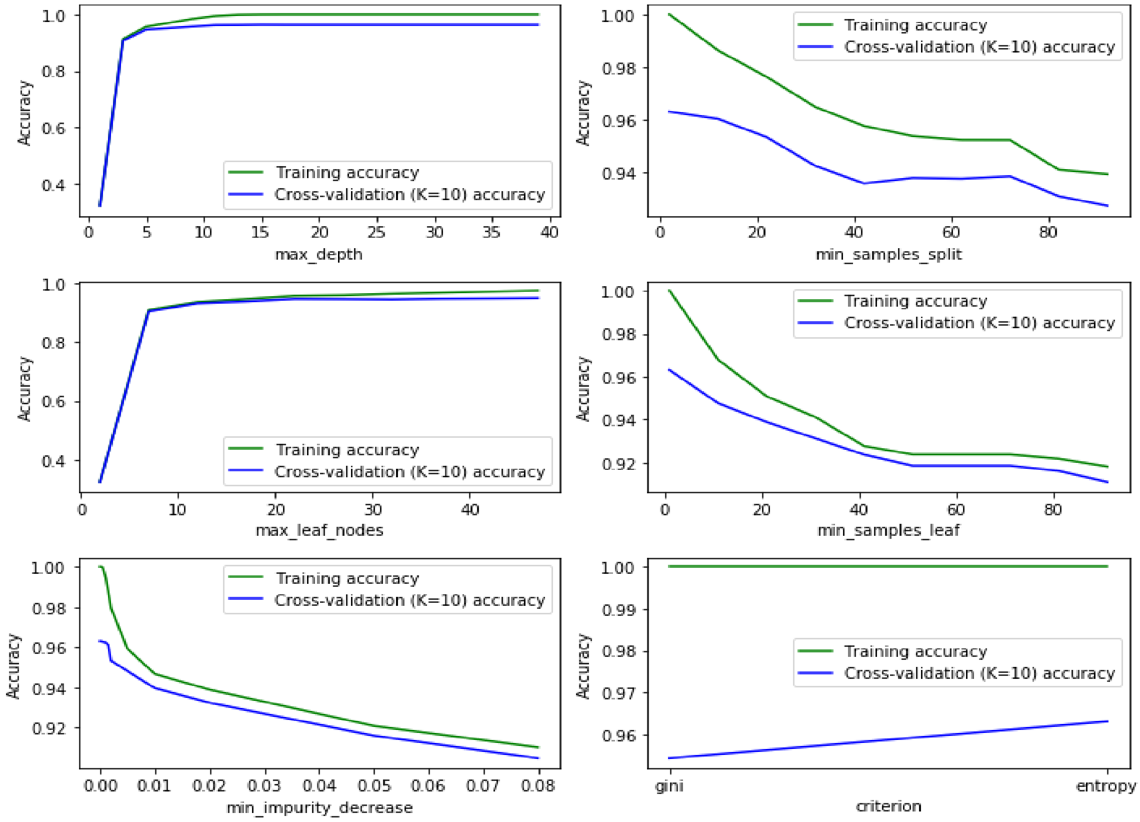

K-fold cross-validation curves (K=10) based of five DTC hyperparameters from Scikit-learn library. Note that the parameters were tuned with the default settings and Entropy as split criterion. Input features are: NDVI, REP, B05 and B11

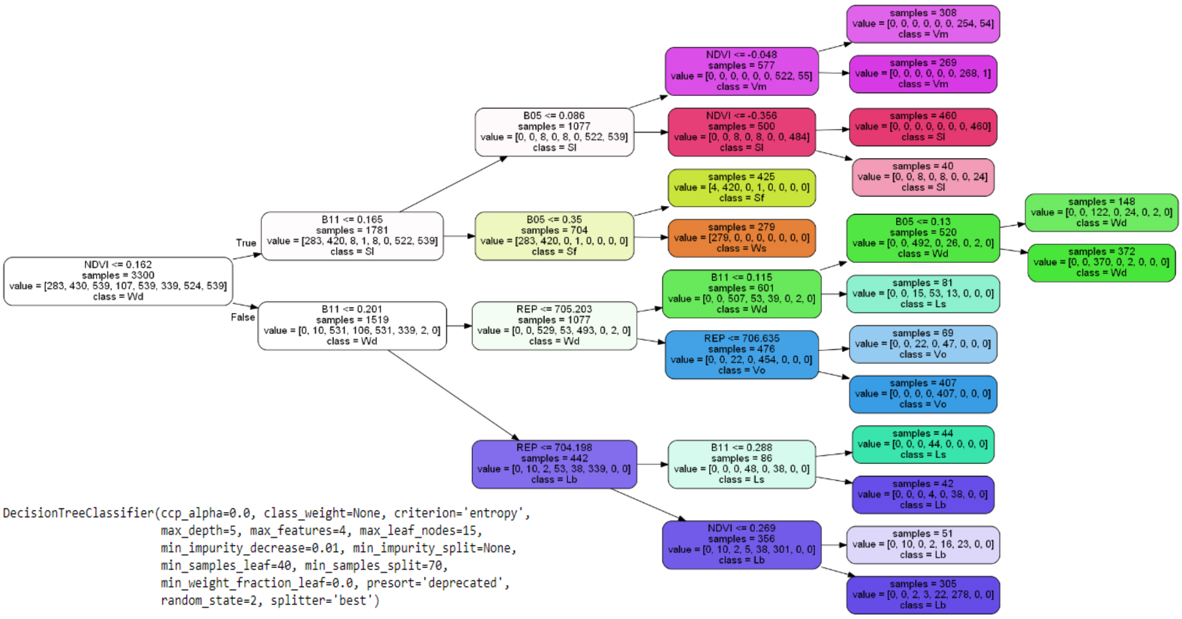

```
DecisionTreeClassifier(ccp_alpha=0.0, class_weight=None, criterion='entropy',
                       max_depth=5, max_features=4, max_leaf_nodes=15,
                       min_impurity_decrease=0.01, min_impurity_split=None,
                       min_samples_leaf=40, min_samples_split=70,
                       min_weight_fraction_leaf=0.0, presort='deprecated',
                       random_state=2, splitter='best')
```

Decision Tree model with four input features: NDVI, REP, B05 and B11. The selected hyperparameters in Scikit-learn are shown at the bottom left corner.

Appendix 4 Accuracy assessment of Sargassum classification in Lac Bay

DTC and MLC models accuracies (MA) in predicting Sargassum and other coastal features. The MLC based rejection class is not included in the accuracy assessment.

Model acc.	Lb	Ls	Sf	Sl	Vm	Vo	Wd	Ws	**Classified**	**UA**	**F1-score**	**Classifier**
Lb	67	3	-	-	-	-	-	-	70	0.96	0.98	DTC
Ls	-	104	-	-	-	3	-	-	107	0.97	0.97	
Sf	-	-	122	7	3	1	-	2	135	0.9	0.91	
Sl	-	-	-	26	-	1	-	-	27	0.96	0.83	
Vm	-	-	10	3	112	8	1	1	135	0.83	0.9	
Vo	-	-	-	-	-	85	-	-	85	1	0.93	
Wd	-	-	-	-	-	-	131	-	131	1	0.93	
Ws	-	-	-	-	-	-	19	116	135	0.86	0.91	
Observed	67	107	132	36	115	98	151	119	**825**	-	-	
PA	1	0.97	0.92	0.72	0.97	0.87	0.87	0.97	-	**0.92 (MA)**		
Lb	70	-	-	-	-	-	-	-	70	1	1	MLC$_{Base}$
Ls	-	105	-	-	-	2	-	-	107	0.98	0.99	
Sf	-	-	127	2	6	-	-	-	135	0.94	0.93	
Sl	-	-	-	25	1	1	-	-	27	0.93	0.93	
Vm	-	-	10	-	120	4	-	1	135	0.89	0.92	
Vo	-	-	-	-	-	85	-	-	85	1	0.96	
Wd	-	-	-	-	-	-	131	-	131	1	0.94	
Ws	-	-	-	-	-	-	16	119	135	0.88	0.93	
Observed	70	105	137	27	127	92	147	120	**825**	-	-	
PA	1	1	0.93	0.93	0.94	0.92	0.89	0.99	-	**0.95 (MA)**		
Lb	54	-	-	-	-	-	-	-	54	1	1	MLC$_{10\%}$
Ls	-	97	-	-	-	1	-	-	98	0.99	0.99	
Sf	-	-	120	-	6	-	-	-	126	0.95	0.95	
Sl	-	-	-	24	-	1	-	-	25	0.96	0.98	
Vm	-	-	7	-	117	3	-	-	127	0.92	0.94	
Vo	-	-	-	-	-	74	-	-	74	1	0.97	
Wd	-	-	-	-	-	-	122	-	122	1	0.95	
Ws	-	-	-	-	-	-	13	105	118	0.89	0.94	
Observed	54	97	127	24	123	79	135	105	**744**	-	-	
PA	1	1	0.94	1	0.95	0.94	0.9	1	-	**0.96 (MA)**		
Lb	50	-	-	-	-	-	-	-	50	1	1	MLC$_{20\%}$
Ls	-	84	-	-	-	1	-	-	85	0.99	0.99	
Sf	-	-	113	-	6	-	-	-	119	0.95	0.95	
Sl	-	-	-	22	-	1	-	-	23	0.96	0.98	
Vm	-	-	6	-	112	1	-	-	119	0.94	0.95	
Vo	-	-	-	-	-	72	-	-	72	1	0.98	
Wd	-	-	-	-	-	-	115	-	115	1	0.95	
Ws	-	-	-	-	-	-	12	98	110	0.89	0.94	

DTC and MLC models accuracies (MA) in predicting Sargassum and other coastal features. The MLC based rejection class is not included in the accuracy assessment (continued).

Observed	50	84	119	22	118	75	127	98	**693**	-	-	
PA	1	1	0.95	1	0.95	0.96	0.91	1	-	**0.96 (MA)**	**0.95 (Kappa)**	
Lb	40	-	-	-	-	-	-	-	40	1	1	MLC$_{50\%}$
Ls	-	65	-	-	-	-	-	-	65	1	1	
Sf	-	-	83	-	-	-	-	-	83	1	0.99	
Sl	-	-	-	12	-	1	-	-	13	0.92	0.96	
Vm	-	-	1	-	102	1	-	-	104	0.98	0.99	
Vo	-	-	-	-	-	51	-	-	51	1	0.98	
Wd	-	-	-	-	-	-	79	-	79	1	0.96	
Ws	-	-	-	-	-	-	7	84	91	0.92	0.96	
	40	65	84	12	102	53	86	84	**526**	-	-	
PA	1	1	0.99	1	1	0.96	0.92	1	-	**0.98 (MA)**		

External validation (VA) accuracies of DTC and MLC models for a scene taken on 18 May 2019. The validation was based on floating Sargassum (Sf) (= 80 samples) and non- floating Sargassum (Non-Sf) (= 80 samples) classes.

Validation acc.	Non-Sf	Sf	**Classified**	**UA**	**F1-score**	**Classifier**
Non-Sf	70	10	80	0.88	0.85	DTC
Sf	14	66	80	0.82	0.85	
Observed	84	76	**160**	-	-	
PA	0.83	0.87	-	**0.85 (VA)**		
Non-Sf	68	12	80	0.85	0.86	MLC$_{Base}$
Sf	11	69	80	0.86	0.86	
Observed	79	81	**160**	-	-	
PA	0.86	0.85	-	**0.86 (VA)**		
Non-Sf	73	7	80	0.91	0.88	MLC$_{10\%}$
Sf	12	68	80	0.85	0.88	
Observed	85	75	**160**	-	-	
PA	0.86	0.91	-	**0.88 (VA)**		
Non-Sf	77	3	80	0.96	0.88	MLC$_{20\%}$
Sf	18	62	80	0.78	0.86	
Observed	95	65	**160**	-	-	
PA	0.81	0.95	-	**0.87 (VA)**		
Non-Sf	80	-	80	1	0.81	MLC$_{50\%}$
Sf	38	42	80	0.52	0.69	
Observed	118	42	**160**	-	-	
PA	0.68	1	-	**0.76 (VA)**		

Appendix 5 Sargassum misclassification masks

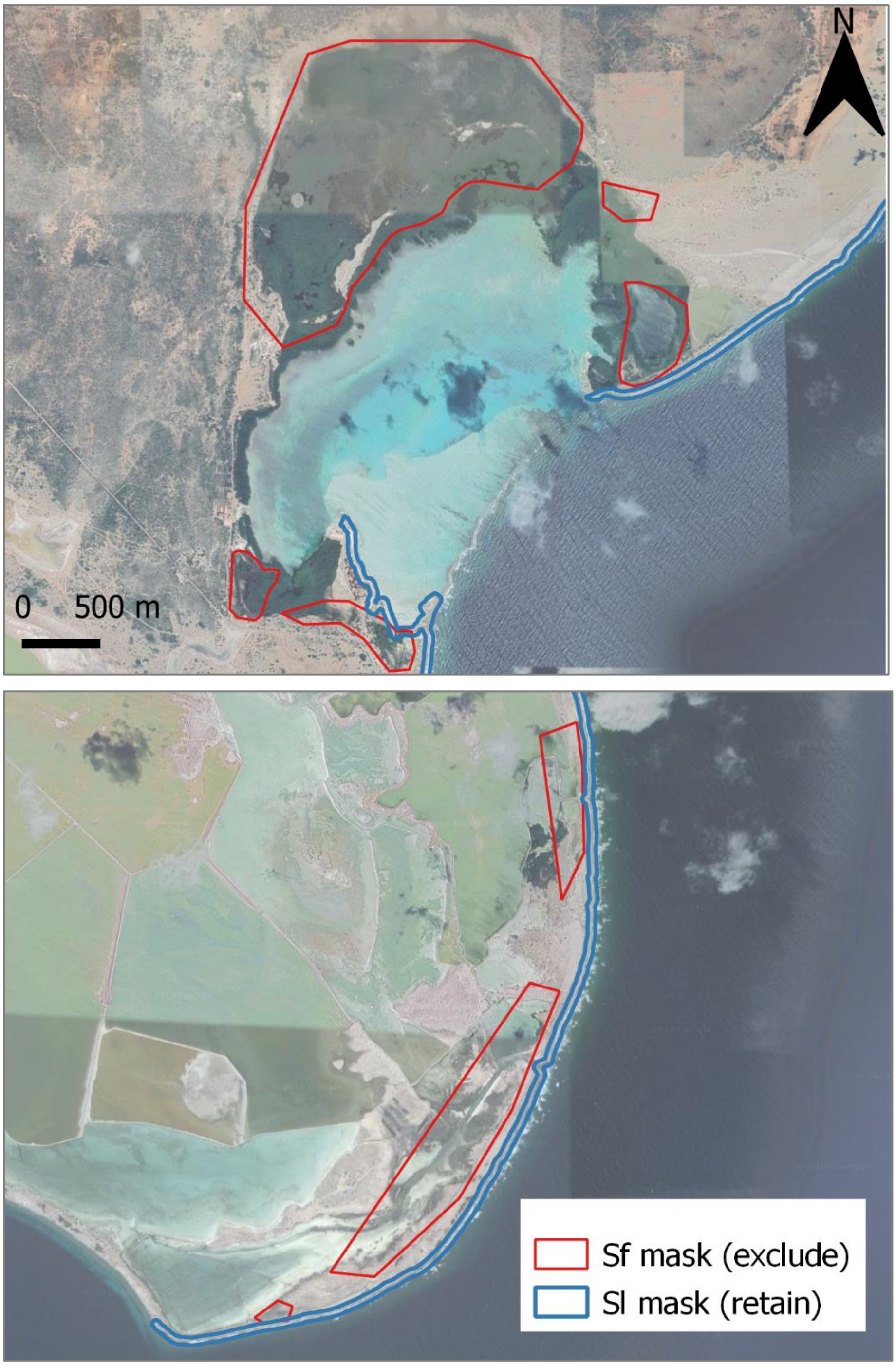

Masks used to exclude false positive pixels from mangrove areas (Sf mask) and retain Sargassum pixels around 25m from the coastline (Sl mask). Satellite image by Google Maps ®.

Appendix 6 False colour composite series of Lac Bay and Lagun

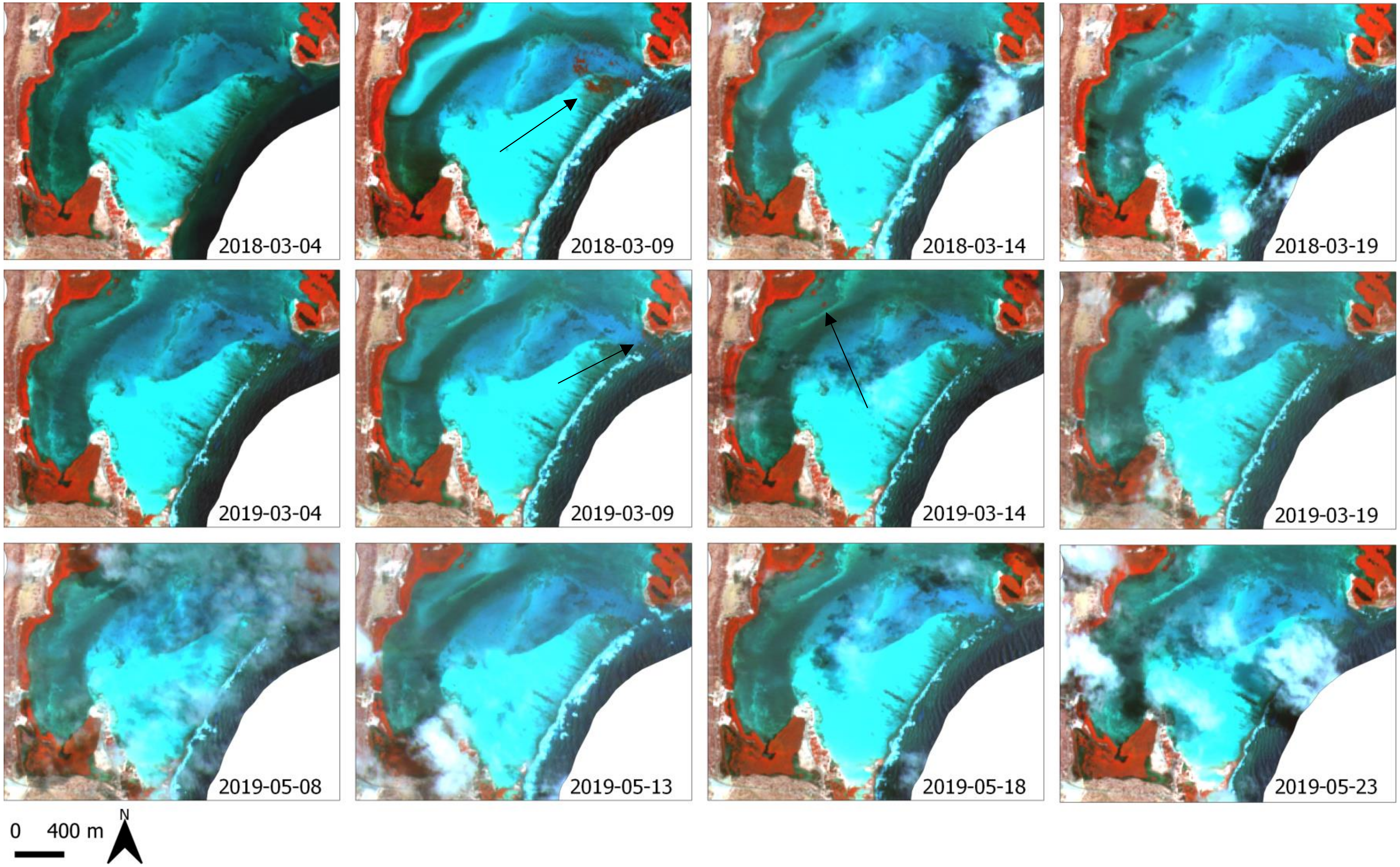

Image enhanced false colour composite series of Lac Bay during the invasion periods in March 2018, March and May 2019. The black arrows indicate location of floating Sargassum. The presence of clouds was noticeable in most of the scenes in the series.

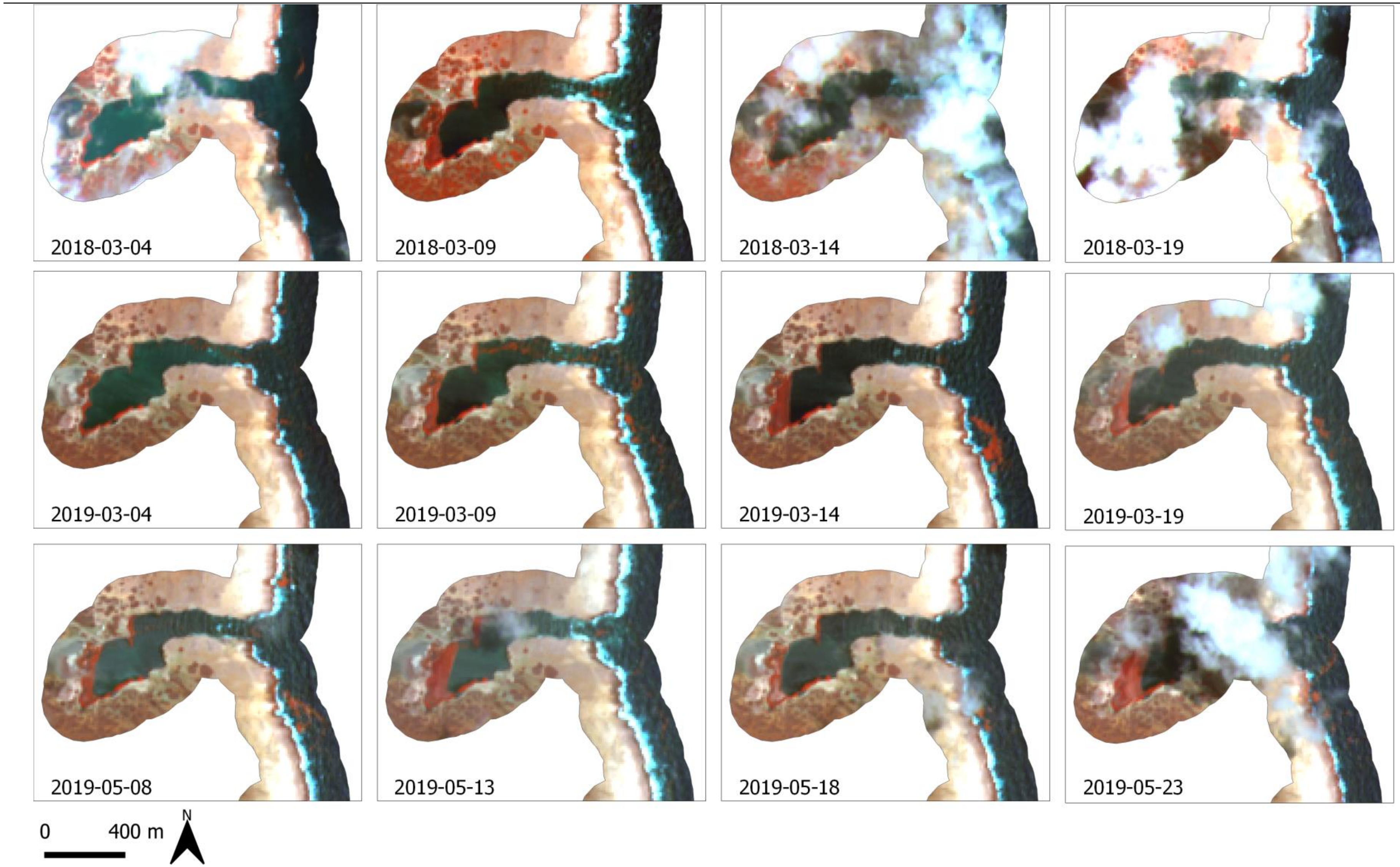

Image enhanced false colour composite series of Lagun during the invasion periods in March 2018, March and May 2019. The presence of clouds was noticeable in most of the scenes in the series.

Appendix 7 Triangle thresholding of Principal Component images

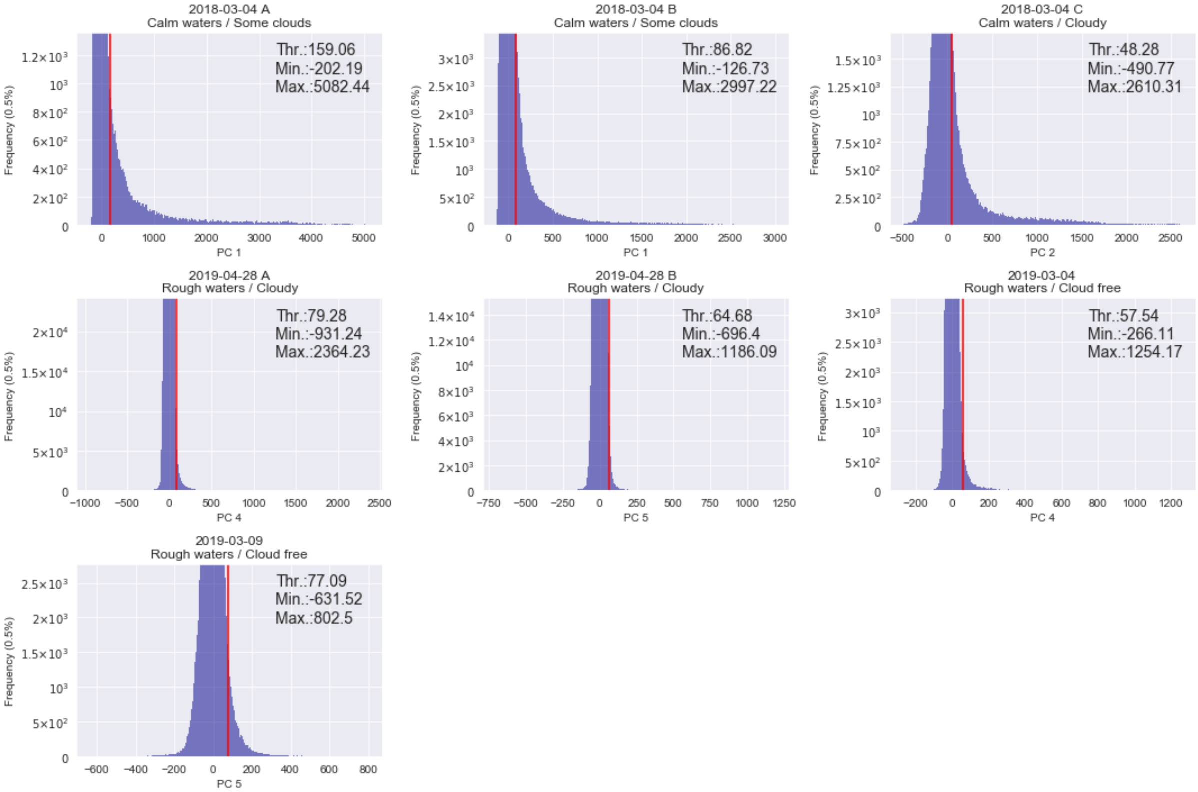

Principle Component image data distribution of each subset including the position of the computed threshold in red. The y-axes are limited to 0.5% of the data.

Appendix 8 Sampled dataset covering seagrass and non-seagrass bottom types obtained from Lac Bay

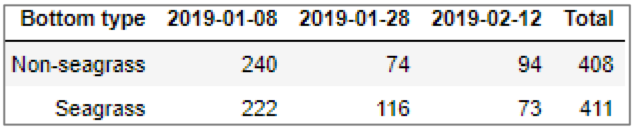

Bottom type	2019-01-08	2019-01-28	2019-02-12	Total
Non-seagrass	240	74	94	408
Seagrass	222	116	73	411

Number of sampled pixels from each Sentinel-2 scene

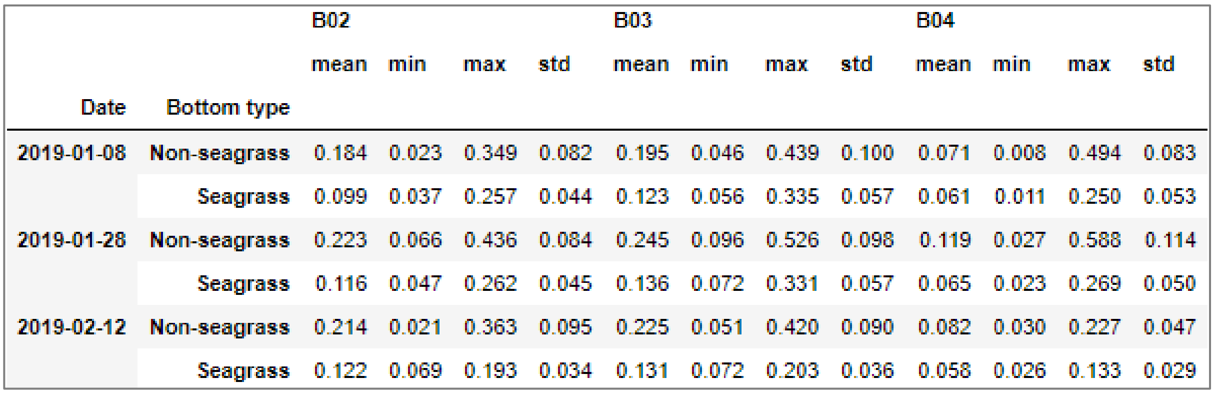

		B02				B03				B04			
		mean	min	max	std	mean	min	max	std	mean	min	max	std
Date	Bottom type												
2019-01-08	Non-seagrass	0.184	0.023	0.349	0.082	0.195	0.046	0.439	0.100	0.071	0.008	0.494	0.083
	Seagrass	0.099	0.037	0.257	0.044	0.123	0.056	0.335	0.057	0.061	0.011	0.250	0.053
2019-01-28	Non-seagrass	0.223	0.066	0.436	0.084	0.245	0.096	0.526	0.098	0.119	0.027	0.588	0.114
	Seagrass	0.116	0.047	0.262	0.045	0.136	0.072	0.331	0.057	0.065	0.023	0.269	0.050
2019-02-12	Non-seagrass	0.214	0.021	0.363	0.095	0.225	0.051	0.420	0.090	0.082	0.030	0.227	0.047
	Seagrass	0.122	0.069	0.193	0.034	0.131	0.072	0.203	0.036	0.058	0.026	0.133	0.029

Statistical summary of sampled dataset

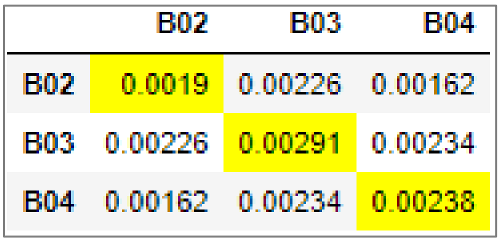

	B02	B03	B04
B02	0.0019	0.00226	0.00162
B03	0.00226	0.00291	0.00234
B04	0.00162	0.00234	0.00238

Band covariance matrix of seagrass class from the sampled dataset. The sampling variance is highlighted in the diagonal.

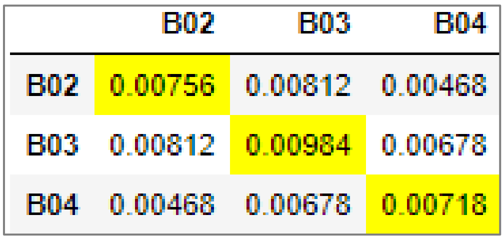

	B02	B03	B04
B02	0.00756	0.00812	0.00468
B03	0.00812	0.00984	0.00678
B04	0.00468	0.00678	0.00718

Band covariance matrix of non-seagrass class from the sampled dataset. The sampling variance is highlighted in the diagonal.

Appendix 9 Hyperparameters tuning and cross-validation of Decision Tree Classifier for bottom type classification

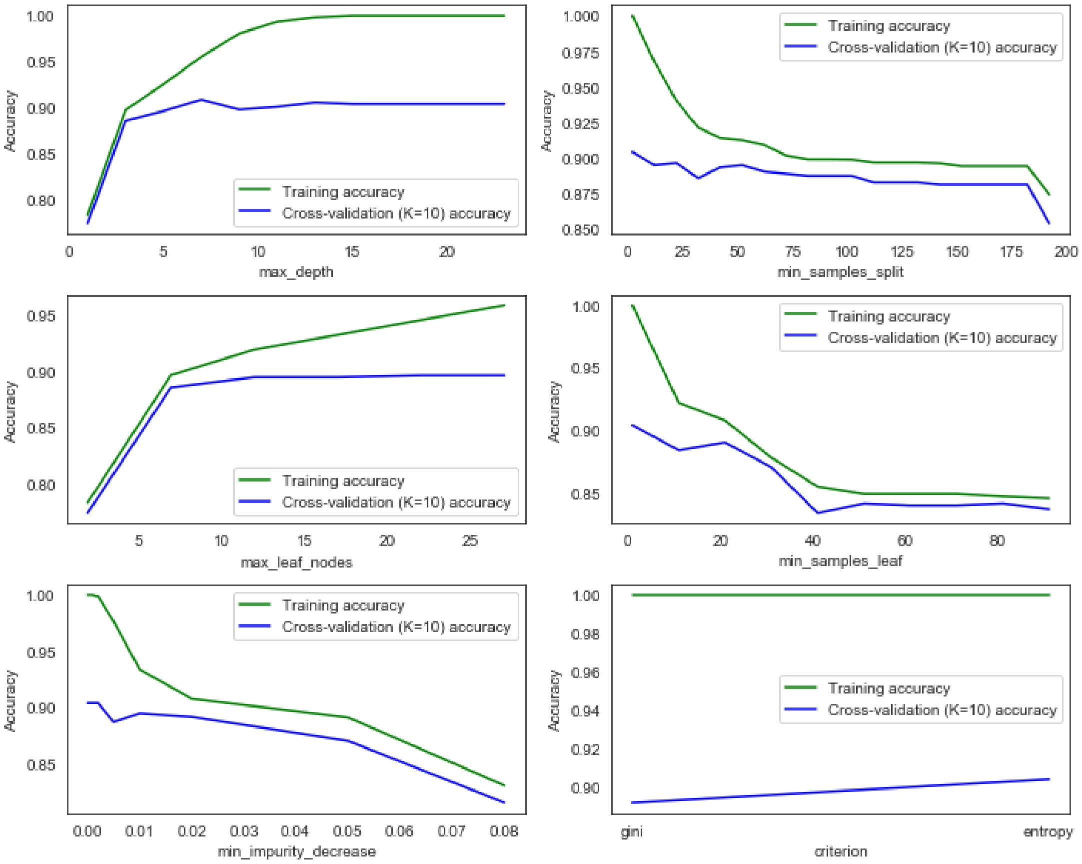

K-fold cross-validation curves (K=10) based of five DTC hyperparameters from Scikit-learn library. Note that the parameters were tuned with the default settings and Entropy as split criterion. Input features are: B02, B03 and B04.

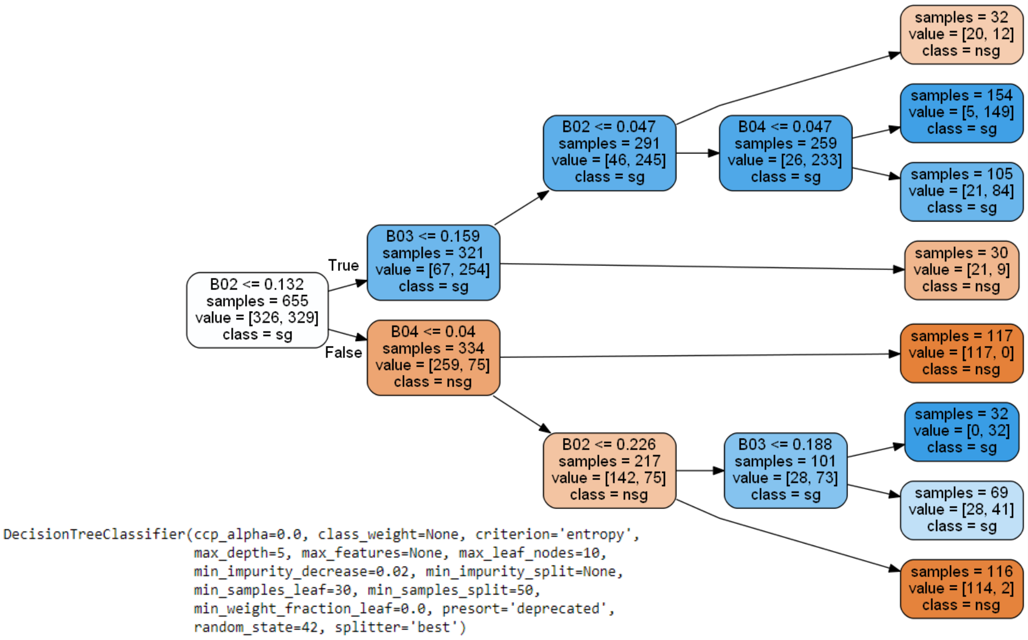

```
DecisionTreeClassifier(ccp_alpha=0.0, class_weight=None, criterion='entropy',
                       max_depth=5, max_features=None, max_leaf_nodes=10,
                       min_impurity_decrease=0.02, min_impurity_split=None,
                       min_samples_leaf=30, min_samples_split=50,
                       min_weight_fraction_leaf=0.0, presort='deprecated',
                       random_state=42, splitter='best')
```

Decision Tree model with three input features: B02, B03 and B04. The selected hyperparameters in Scikit-learn are shown at the bottom.

Appendix 10 Maximum Likelihood Classifier probability and Entropy maps for predicting bottom types in Lac Bay

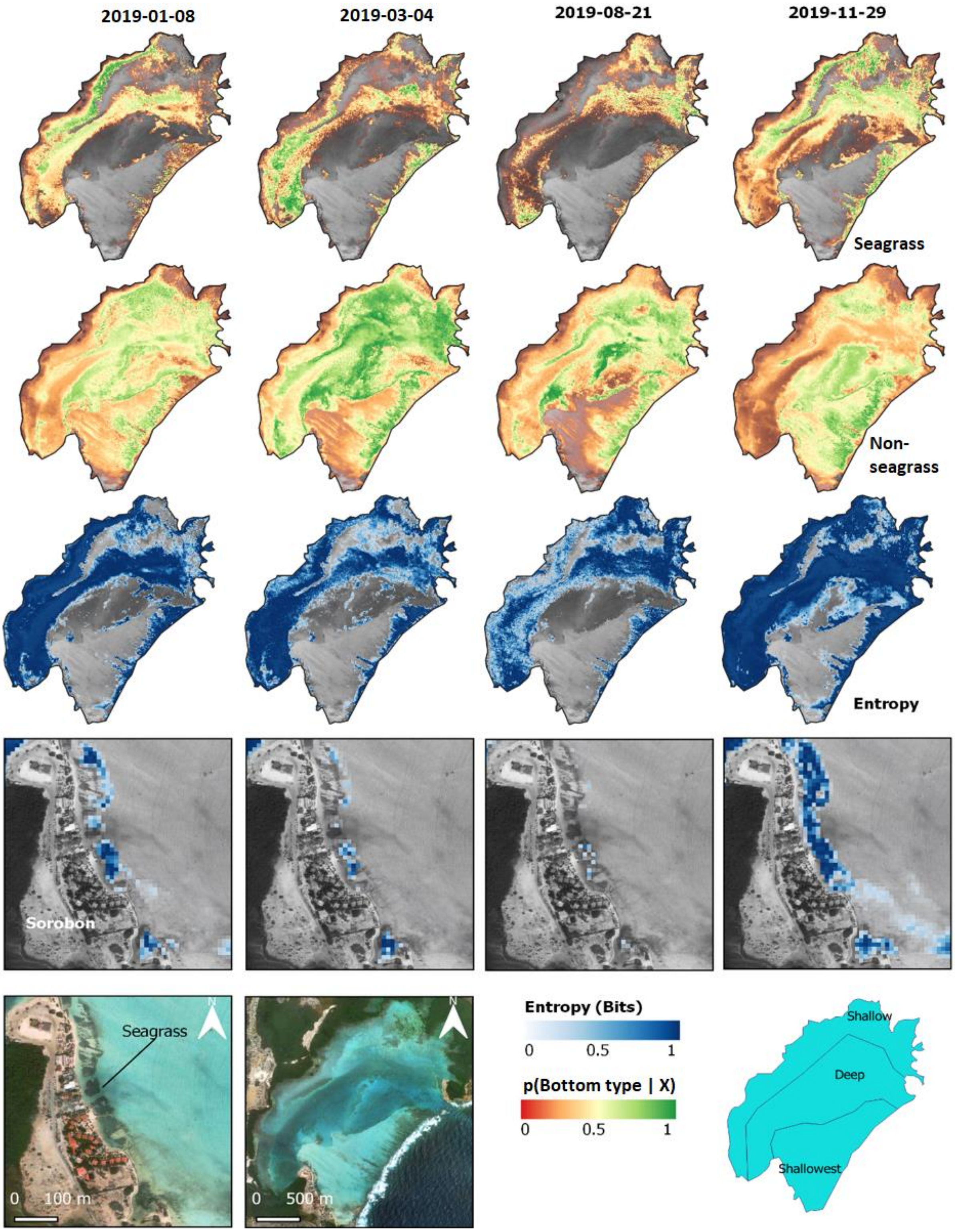

MLC class posterior probability p (Bottom type | X) and Entropy maps across four different scenes. Entropy and probabilities equal to zero are set to transparent for clarity. Entropy value close or equal to 1 refers to complete uncertainty or equal class probabilities. Grayscale and true colour base maps by Bing Maps ® 2019.

Appendix 11 Accuracy assessment of seagrass classification in Lac Bay

DTC and MLC models accuracies (MA) in predicting bottom types

Classified/ observed	Non-seagrass	Seagrass	Total classified	User's acc.	F1-score	Classifier
Non-seagrass	68	6	74	0.92	0.87	DTC
Seagrass	14	76	90	0.84	0.88	
Total observed	82	82	**164**	-	-	
Producer's acc.	0.83	0.93	-	**0.88 (MA)**		
Non-seagrass	65	14	79	0.82	0.81	MLC_{Base}
Seagrass	17	68	85	0.8	0.81	
Total observed	82	82	**164**	-	-	
Producer's acc.	0.79	0.83	-	**0.81 (MA)**		
Non-seagrass	65	14	79	0.82	0.81	$\text{MLC}_{10\%}$
Seagrass	17	68	85	0.8	0.81	
Total observed	82	82	**164**	-	-	
Producer's acc.	0.79	0.83	-	**0.81 (MA)**		
Non-seagrass	68	17	85	0.8	0.82	$\text{MLC}_{20\%}$
Seagrass	13	65	78	0.83	0.81	
Total observed	81	82	**163**	-	-	
Producer's acc.	0.84	0.79	-	**0.82 (MA)**		
Non-seagrass	52	21	73	0.71	0.79	$\text{MLC}_{50\%}$
Seagrass	6	49	55	0.89	0.78	
Total observed	58	70	**128**	-	-	
Producer's acc.	0.9	0.7	-	**0.79 (MA)**		

External validation (VA) accuracies of DTC and MLC models for a scene taken on 4 March 2019. The validation was based on seagrass monitoring dataset 2019.

Classified/ Observed	Non-seagrass	Seagrass	Total classified	User's acc.	F1-score	Classifier
Non-seagrass	8	5	13	0.62	0.64	DTC
Seagrass	4	31	35	0.89	0.87	
Total observed	12	36	**48**	-	-	
Producer's acc.	0.67	0.86	-	**0.81 (VA)**		
Non-seagrass	9	12	21	0.43	0.55	MLC_{Base}
Seagrass	3	24	27	0.89	0.76	
Total observed	12	36	**48**	-	-	
Producer's acc.	0.75	0.67	-	**0.69 (VA)**		
Non-seagrass	10	11	21	0.48	0.61	$\text{MLC}_{10\%}$
Seagrass	2	25	27	0.93	0.79	
Total observed	12	36	**48**	-	-	
Producer's acc.	0.83	0.69	-	**0.73 (VA)**		
Non-seagrass	11	16	27	0.41	0.56	$\text{MLC}_{20\%}$

External validation (VA) accuracies of DTC and MLC models for a scene taken on 4 March 2019. The validation was based on seagrass monitoring dataset 2019 (continued).

Seagrass	1	20	21	0.95	0.7	
Total observed	12	36	**48**	-	-	
Producer's acc.	0.92	0.56	-	**0.65 (VA)**		
Non-seagrass	11	25	36	0.31	0.46	$\text{MLC}_{50\%}$
Seagrass	1	11	12	0.92	0.46	
Total observed	12	36	**48**	-	-	
Producer's acc.	0.92	0.31	-	**0.46 (VA)**		